UNIVERSITY OF CALIFORNIA, SAN DIEGO

The Role of Hematocrit and Nitric Oxide in Regulation in the Microcirculation

A dissertation submitted in partial satisfaction of the
requirements for the degree
Doctor of Philosophy

in

Engineering Science (Mechanical Engineering)

by

Krishna Sriram

Committee in charge:

Professor Daniel M. Tartakovsky, Chair
Professor Marcos Intaglietta, Co-Chair
Professor Pedro Cabrales
Professor Juan Carlos del Alamo
Professor Ratneshwar Lal

2014

The dissertation of Krishna Sriram is approved, and it is
acceptable in quality and form for publication on micro-
film and electronically:

_____

_____

_____
Co-Chair

_____
Chair

University of California, San Diego

2014

DEDICATION

To Anitra, Neelah and Monkey Girl.

There is a theory which states that if ever anyone discovers exactly what the Universe is for and why it is here, it will instantly disappear and be replaced by something even more bizarre and inexplicable.There is another theory which states that this has already happened.

—Douglas Adams

TABLE OF CONTENTS

LIST OF FIGURES

ACKNOWLEDGEMENTS

I would like to thank my faculty advisor Prof. Daniel Tartakovsky for all the help and guidance provided over the last five years.

Also, a sincere thank you to Prof. Marcos Intaglietta, my committe co-chair and collaborator on the research presented in this study.

I would also like to thank my coauthors on the research presented in this stuyd: Dr Pedro Cabrales, Dr Amy Tsai, Dr Paul Johnson, Dr Ozlem Yalcin, Dr Beatriz Salazar-Vazquez, Dr Seetharama Acharya and Dr Fantao Meng.

I am also grateful to my committee members Dr. Ratnesh Lal and Dr. Juan Carlos del Alamo for taking the time to be on my committee and providing their inputs to this work.

Thank you Anitra for the love and support over the years. And thank you Neelah for all the smiles!

And thank you to my family and friends, who have all supported me and encouraged me through this work.

Chapter 5 is currently being prepared for submission for peer review and publication: K. Sriram, D. M. Tartakovsky, and M. Intaglietta. On Optimal Branching of Vascular Networks. 2014. The dissertation author is the primary investigator and author on this paper.

Chapter 6 is currently being prepared for submission for peer review and publication: K. Sriram, D. M. Tartakovsky, and M. Intaglietta. Modeling the Biochemical Reaction Cascade of Endothelial NO Production. 2014. The dissertation author is the primary investigator and author on this paper.

VITA

2014	Doctor of Philosophy in Engineering Science (Mechanical Engineering), University of California, San Diego.
2010	M.Sc. in Mechanical Engineering, University of California, San Diego.
2008	BE in Mechanical Engineering, Rashtriya Vidyalaya College of Engineering, Bangalore, India.

JOURNAL PUBLICATIONS

K. Sriram, B. Y. Salazar Vazquez, O. Yalcin, P. C. Johnson, M. Intaglietta, and D. M. Tartakovsky. The effect of small changes in hematocrit on nitric oxide transport in arterioles. Antioxid. Redox Signal., 14(2):175-185, 2011.

K. Sriram, B. Y. Salazar Vazquez, A. G. Tsai, P. Cabrales, M. Intaglietta, and D. M. Tartakovsky. Autoregulation and mechanotransduction control the arteriolar response to small changes in hematocrit. Am. J. Physiol. Heart Circ. Physiol., 303(9):H1096-1106, 2012.

K. Sriram, M. Intaglietta and D.M. Tartakovsky. Non-Newtonian Flow of Blood in Arterioles: Consequences for Wall Shear Stress Measurements. Under review, Microcir., 02/25/2014.

K. Sriram, A. G. Tsai, P. Cabrales, F. Meng, S. A. Acharya, D. M. Tartakovsky, and M. Intaglietta. PEG albumin supra plasma expansion is due to increased vessel wall shear stress induced by blood viscosity shear thinning. Am. J. Physiol. Heart Circ. Physiol., 302(12):H24892497, 2012.

K. Sriram, D. M. Tartakovsky, and M. Intaglietta. On Optimal Branching of Vascular Networks. 2014. *Under preparation.*

K. Sriram, D. M. Tartakovsky, and M. Intaglietta. Modeling the Biochemical Reaction Cascade of Endothelial NO Production. 2014. *Under preparation.*

ABSTRACT OF THE DISSERTATION

The Role of Hematocrit and Nitric Oxide in Regulation in the Microcirculation

by

Krishna Sriram

Doctor of Philosophy in Engineering Science (Mechanical Engineering)

University of California, San Diego, 2014

Professor Daniel M. Tartakovsky, Chair
Professor Marcos Intaglietta, Co-Chair

Nitric oxide is a critical signaling molecule in the microcirculatory control of vascular resistance. It enables the maintenance of blood pressure and cardiac output at optimal levels, via flow mediated endothelial nitric oxide production which serves to modulate vascular tone. Understanding nitric oxide production and bioavailability in the vasculature facilitates a number of theoretical models and clinical applications. Hematocrit influences the vaso-active role of nitric oxide, since both blood viscosity and shear stress increase with red blood cell concentrations. Moreover, increases in hematocrit cause cell free layer thickness to decrease and hemoglobin scavenging of nitric oxide in red blood cells to increase.

To capture this behavior at the scale of an individual blood vessel, we construct a model of the autoregulatory response of blood vessels. The model incorporates coupled models of blood flow and nitric oxide transport, thereby explaining how changes in hematocrit influence vascular response. We also develop a model that captures the effects of changing hematocrit on blood rheology, velocity profiles and wall shear stress

measurements. This model accounts for the non-Newtonian, shear-thinning properties of blood. A clinical application of these ideas is demonstrated by showing how changes in the blood rheology via plasma expanders can result in the restoration of cardiac performance. These individual-vessel models inform our analysis of the structure of microvascular networks. Specifically, we examine how hematocrit, pressure and shear stress are distributed in optimally configured model networks. Our approach allows for simulation of vascular networks which exhibit the broad characteristics of networks observed in-vivo.

At the cellular level, we examine the biochemistry of nitric oxide production inside endothelial cells. We construct a model which simulates the endothelial nitric oxide production cycle, following application of shear stress. Our model predictions for both steady and transient shear induced nitric oxide production are shown to be in broad agreement with experimental data. Collectively, this dissertation significantly enhances our understanding of the dual and often competing roles of nitric oxide and hematocrit in the microcirculation.

Chapter 1

Introduction

1.1   Motivation for this study

The bulk of the pressure drop encountered in the circulatory system is encountered in the microcirculation, specifically in the arteriolar portion of the vascular network [34]. Hence, the majority of vascular resistance is encountered in these 'resistance' vessels. Understanding how arterioles both individually and as a network act to control vascular resistance is thus central to understand how blood pressure is regulated in a variety of physiological contexts.

Central to the problem of arteriolar control of vascular resistance is the means by which arterioles maintain their radius in response to blood flow through the arterioles. Exposure to intra-luminal fluid pressure causes a mechanical response in arterioles due to the passive, elastic properties of the blood vessel, as well as the active, myogenic response [181, 82]. The combination of these mechanical responses leads to the constriction of arterioles on exposure to elevated levels of blood pressure, resulting in increased vascular resistance [181].

The active, constricting response of arterioles is modulated by Nitric Oxide (NO) [44, 8]; as discussed in chapter 7 of this dissertation, NO is produced in endothelial cells on exposure to shear stress. The NO thus produced diffuses both into the blood stream and the adjacent smooth muscle tissue [103]; the NO in smooth muscles stimulates cGMP production [204, 38], which in turn stimulates vasodilation. Thus, NO serves as a critical

regulator of blood pressure, by modulating vascular resistance [75, 44] via shear-induced endothelial NO production.

The bioavailability of NO is in turn impacted by hematocrit in two regards: 1) RBCs consume NO very rapidly [7, 30, 182, 103, 193] and 2) increased hematocrit leads to higher blood viscosity and shear stress, along with reduced cell free layer thickness [195]. Increases in hematocrit would normally be expected to increase blood pressure and vascular resistance due to this increase in blood viscosity [195, 181, 116, 117], however, increased NO production due to the associated elevation of shear stress is hypothesized to offset this effect [195].

In developing tools for modeling vascular resistance across the microcirculation, we must therefore account for the dual (and competing) roles of hematocrit and NO in regulation of the microvasculature. Specifically, we require a number of individual components (each addressing specific aspects of roles of NO and hematocrit) that can eventually be combined to develop an integrated model of the microcirculation.

In addition to theoretical considerations, our study was also motivated by a range of experimental studies seeking to examine the response of the physiology to acute changes in hematocrit. These studies included a) experiments involving modest levels of hemoconcentration and/or hemodilution [116, 117, 195] and b) experiments involving the use of plasma expanders to modify blood viscosity, thereby facilitating restoration of cardiac performance, following severe hemorrhagic shock [26, 27, 190, 192]. These experimental studies serve to highlight the need for modeling tools to help shed light on the coupled roles of NO and hematocrit in maintaining vascular resistance.

1.1.1 A Question of Scales

Understanding (and modeling) how the microcirculation responds to changes in state (such as variations of pressure or of hematocrit) involves understanding a series of mechanisms occurring at different scales of organization. At the scale of an organ system, there are as yet many open questions about how best to model the structure of vascular networks and stemming from this, how to appropriately model the distributions of pressure, shear stress, hematocrit etc [145, 173, 134, 40, 86, 198].

The response of individual vessels comprising this network involves a complex

behavior, whereby vessel response to intraluminal pressure via a passive, elastic response [82] and an active, myogenic response. The net effect of these responses is that blood vessels constrict on exposure to pressure [181]. This solid mechanics response is coupled to fluid flow of blood through the vessel, since the myogenic response is offset by shear induced endothelial NO production, leading to dilation when NO concentrations are increased [91, 181]. Variations of hematocrit are then coupled to this fluid-solid problem, due to the coupling between hematocrit and NO concentrations discussed above. Hence, models that describe the response of individual vessels must account for a) the solid mechanics of a blood vessel b) NO transport and c) blood flow in microvessels.

Models of NO transport [30, 182, 103, 102, 66] rely on assumptions regarding the nature of endothelial NO production; specifically, whether any negative feedback exists and how NO production is related to variables such as shear stress, oxygen availability, the presence of metabolic substrates etc. An exploration of the sensitivity of these transport models to these variables requires a model for the biochemistry of Nitric Oxide at the scale of the individual endothelial cell. Models of the biochemistry of NO production have to date [142, 141, 37] been very limited, as discussed in chapter 6, highlighting the need for models that better represent the biochemistry associated with shear-induced NO production.

Hence, modeling vascular networks relies on models of multiple physiological processes occurring over a range of scales of organization. This is illustrated in figure 1.1.

1.2   Objectives of this Dissertation

1) To develop a mechanical model of a blood vessel that can be coupled with a model of blood flow in a vessel and a model of NO transport, enabling is to develop a comprehensive picture of the response of an individual blood vessel to changes in hematocrit.

2) To account for the means by which plasma expanders such as PEG-Alb help to restore cardiac function following severe hemorrhagic shock, in the process accounting for the strong shear-thinning non-Newtonian rheology of blood in the presence of PEG-Alb.
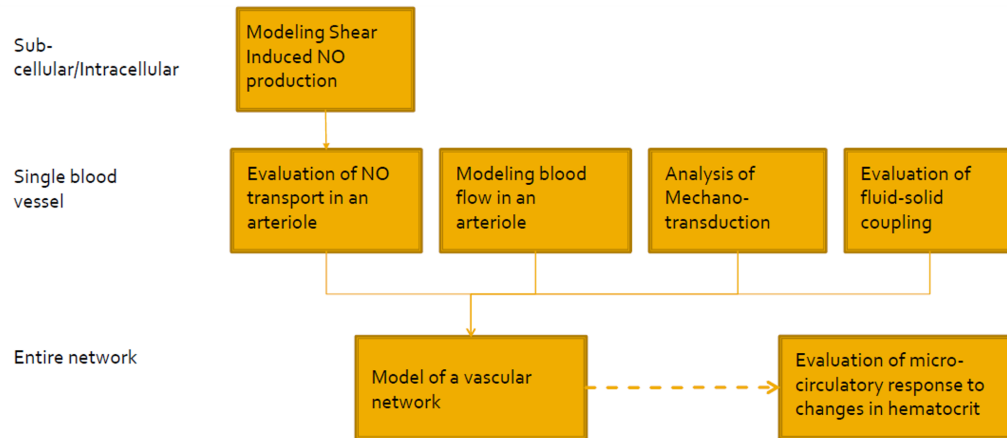
Figure 1.1: The multi-scale nature of the problem of modeling the microcirculation.

3) To develop a more complete model of blood flow in an arteriole, so as to account for both the non-homogeneous and non-Newtonian nature of blood flow in microvessels. To then leverage this model to develop a correction factor for calculation of wall shear stress in experimental setups that rely on the application of the Hagen-Poiseuille law for shear stress estimation.

4) To develop a model for a microvascular network, so as to account for hematocrit distributions in asymmetric networks, as well as overcoming many of the commonly encountered difficulties with Murray's 1/3rd law [145].

5) To develop a biochemical model of the process of NO production within endothelial cells, following exposure to shear stress. Such a model may be leveraged to study a number of aspects of endothelial NO production, especially the transient behavior of shear induced NO production.To then apply this model to evaluate the functional relationship of NO production vs shear stress and the importance of negative feedback.

1.3   The Components of this Dissertation

1.3.1   Modeling autoregulatory response of an arteriole

In chapter 2 of this dissertation, we develop a model for the solid mechanics of an arteriole, so as to describe the deformation of an arteriole due to small changes in intraluminal pressure. By coupling this model of vessel mechanics to a multiphase model of blood, we arrive at a mathematical description of arteriolar response to pressure variations that suitably describes auto-regulation by arterioles. The resulting model describes both the passive, elastic response and the active, myogenic response of arterioles, with the myogenic response being modulated by shear stress. Coupled to this model, is a model for NO transport; for calculated deformations due to variations in pressure, our model allows us to relate NO concentrations in smooth muscle with the extent of vessel dilation.

We then apply this model to analyze the variation of flow rate with hematocrit, given an experimentally determined variation of blood pressure with hematocrit [116, 117, 195]. Using this analysis, we were able to show that the dependence of flow rate (and hence cardiac output) with hematocrit depends on the balance of myogenic (active) vessel response vs passive (elastic) vessel response. The paradoxical behavior thus reported in [116, 117, 195] was found to arise as a result of the offsetting of the autoregulatory response of arterioles, a phenomenon also observed in [132]. We also showed that the reductions of vascular resistance were accompanied by significant increases in vascular NO concentrations.

1.3.2   Analysis of PEG-Albumin plasma expansion

In chapter 3, we utilize the Quemada rheological model [157], to develop a model of the non-Newtonian flow of blood through a microvessel. We leverage the work of [144] to develop a numerical solution for the velocity profiles of non-Newtonian blood flow, while assuming a non-uniform, sigmoid distribution of hematocrit across the vessel cross section. The model thus produced predicts blunted velocity profiles and elevated shear rates near the vessel walls.

We then applied this flow model to analyze the flow of various plasma expanders

(Dextran 70, Dextran 500 and PEG-Albumin) in animals suffering hemorrhagic shock, thus demonstrating very low hematocrits (11 %). The rheology of hemodiluted blood with each plasma expander was measured, with PEG-Alb found to exhibit very strong shear-thinning characteristics. As a result, PEG-Alb was found to be associated with sharply elevated shear stresses in microvessels, leading to the restoration of cardiac performance. We thus show that PEG-Alb is efficacious as a plasma expander due to it's shear-thinning properties, which lead to elevated apparent viscosities in arterioles.

1.3.3 Development of non-Newtonian blood flow models in arterioles and derivation of Wall shear stress correction factors

In chapter 4, we develop a model for the non-Newtonian, non-homogeneous flow of human blood through a microvessel. We model blood flow in a microvessel as consisting of two immiscible, homogeneous layers; a cell free layer (CFL) near the vessel walls and an RBC rich core layer near the vessel centerline. The rheology of of the core region was described using the Quemada model [157, 114], while the CFL was assumed to be Newtonian. Using previously published data [151] for the variation of apparent viscosity of blood flow vs hematocrit and vessel radius, we derived an expression for CFL thickness as a function of hematocrit.

The resulting flow model was validated by comparing our model predictions for velocity profiles, CFL thicknesses, core hematocrit and tube hematocrit at different discharge hematocrits and vessel radii vs published experimental data for these quantities. We thus demonstrate that our model satisfies a broad range of experimental data points to a greater degree than previous models of blood flow in arterioles [172, 182, 130].

We then apply our model to develop a correction factor to improve the experimental estimation of wall shear stress (WSS). Typically, WSS is estimated by measuring vessel centerline velocity and radius, followed by application of the Hagen-Poiseuille law to obtain a value of shear stress [160]. Due to the non-homogeneous and non-Newtonian nature of blood, this approach results in considerable errors [160]. We leverage our model to derive a correction factor that can be applied to the Hagen-Poiseuille law, so as to accurately determine WSS, given a measured centerline velocity and vessel radius. By this

method, we reduce the need for expensive experimental techniques such as micro-PIV for the accurate estimation of WSS.

1.3.4   Optimal branching in vascular networks

In Chapter 5, we discuss the development of a model to describe the branching and hematocrit distribution in asymmetric vascular networks. Our analysis builds on previous work in [2] to modify Murray's 1/3rd law [129] so as to account for the deviations from Murray's law observed in the microcirculation [145, 86]. We demonstrate that the resulting modification to Murray's law is able to account for the non-uniform WSS observed in vascular networks [106] and predicts realistic pressure distributions [34] as well.

We then apply this modified Murray's law to evaluate the distribution of hematocrit at vascular bifurcations. We show that RBC flux fractions vary linearly with blood flow fractions at bifurcations, in agreement with several previous studies [57, 47, 92, 174, 10, 11] but contradicted by others [150, 154, 77]. Using this analysis across successive vessel generations in a vascular network, we calculate distributions of vessel radii and hematocrit that indicate large degrees of scatter in the values of hematocrit across all vessels of any given vessel generation. We demonstrate that our modeled 'optimal' networks demonstrate a range of characteristics seen in vascular networks studied in-vivo, thereby providing us with a 'realistic' model for simulating vascular networks.

1.3.5   Modeling the biochemical cascade of shear induced endothelial NO production

In chapter 6, we present a model for the series of biochemical reactions that result in the production of NO by endothelial cells following the application of shear stress. We describe the set of biochemical reactions using a system of coupled ODEs, triggered by the application of shear stress, which activates mechanotransducers in endothelial cells. The mechanotransducers considered in our model are Mechanosensing Ion Channels (MSICs), Integrins and G-Protein Coupled Receptors (GPCRS). The activation of these mechanotransducers by shear stress is modeled using constitutive relations based on

previous modeling and experimental studies.

Subsequent to activation of mechanotransducers, our model describes the influx of calcium into the cell cytosol, as well as the activation of protein kinases. We then model the formation of complexes of the endothelial Nitric Oxide Synthase (eNOS) enzyme with calmodulin, followed by activation via phosphoryaltion. We then accounted for the production of cGMP stemming from elevated NO concentrations and account for the hypothesized negative feedback provided by cGMP due to the inhibition of calcium influx into the cytosol.

With this model constructed, we demonstrate agreement with experimental data for both transient and steady state NO production, as well as a number of other quantitative and empirical comparisons with published experimental data. We also evaluate the importance of the negative feedback cGMP loop, and demonstrate that negative feedback is relatively unimportant in this reaction cascade, under normal, physiological conditions.

Chapter 2

Autoregulation and mechanotransduction control the arteriolar response to small changes in hematocrit

2.1 Introduction

The existence of a direct relationship between blood viscosity (and hematocrit, Hct) and blood pressure is a widely held assumption, also supported by epidemiological studies [48, 111]. However, this finding may be more applicable to the older population where endothelial dysfunction mitigates the vasodilatory response of increased vessel wall shear stress (WSS), or when the induced hemoconcentration exceeds the variability of Hct found in the normal population [163]. The influence of changes in Hct on blood pressure and cardiac output (CO) within the range of changes found in the normal population has been studied experimentally [116, 117, 195] showing a counterintuitive behavior, wherein small Hct increases are associated with decreased blood pressure and increased CO. An explanation for this behavior is that increased Hct and fluid viscosity increases WSS [195] in arterioles, thus increasing nitric oxide (NO) production by the

endothelium [118, 122]. This increased NO production promotes vasodilation (2), causing blood pressure to decrease and CO to increase [195]. The existence of this mechanism was confirmed by experiments, in which the administration of L-NAME blocked NO production by the endothelium, negating this effect.

The administration of L-NAME causes general vasoconstriction of the vasculature, which may overcome additional vasodilator mechanisms induced by the increase in Hct and blood viscosity [195, 182]. Furthermore, the effects on blood pressure, CO and peripheral vascular resistance are comparatively large relative to the magnitude of the WSS stimulus, suggesting the existence of additional non-NO dependent mechanisms.

The behavior of the circulation (and corresponding regulation) is influenced by coupled physical and biochemical phenomena, including the myogenic response, stimulation by the sympathetic nervous system, effects of shear stress, etc. [45, 82]. In addition, blood oxygen carrying capacity increases with Hct, thereby reducing the blood flow required to maintain a constant level of oxygen delivery [17].

Several previous studies [8, 21, 91, 170] have focused on development of mathematical models of the blood flow regulation by the vasculature. These models describe the mechanics of the vascular wall exposed to internal pressure and the corresponding effects on vessel tone. They also provide mathematical descriptions of the myogenic response and WSS-induced effects, and of the coupled behavior of blood flow and the mechanics of the vessel wall. These studies model the behavior of vessel walls by relying on Laplaces law, which is rigorously valid for thin elastic cylinders [170] and remains accurate as long as the ratio of a vessels wall thickness to its diameter exceeds 10 (ideally 20 or more) [95]. While this condition is applicable to arteries, it breaks down for arterioles where this ratio can be as small as 2 or even less [143]. Finally, these models describe the effects of WSS on vascular tone by employing simple constitutive laws relating WSS with vessel wall tension, without accounting for the variation of NO bioavailability in the vascular wall due to WSS changes.

Motivated by the experimentally observed changes in blood pressure with Hct, we model the dependence of blood flow (and CO) on systemic Hct by treating arterioles as thick, elastic cylinders [189, 199] and coupling hemodynamics and vessel mechanics. The model enables us to investigate the effects of this coupling on autoregulation and to

describe changes in the wall thickness with changing intraluminal pressure. The latter is a crucial factor for calculating NO transport in the vasculature. We evaluate the concentration profiles of NO in the vessel wall [182] in order to account for vasodilation due to WSS-induced NO production.

Experimental studies to describe the mechanical properties of arteries and arterioles typically quantify elastic moduli [15] or develop length-tension curves for individual blood vessels. The observed mechanical behavior is reported as a constitutive law [91, 170], comprising of active and passive (elastic/viscoelastic) components. Our model accounts for both active and passive stresses. The passive stress is determined by intraluminal pressure; the active stress (the myogenic response) is a function of tension in the vessel wall [20, 82, 170]. We account for the relationship between pressure and radius of arterioles for small changes in pressure and then describe the effect of varying Hct on flow rate through the blood vessel (and hence cardiac output).

2.1.1 Symbols and Acronyms used

ν	Poisson's Ratio
R, R_0, r	Inner and outer vessel wall radii, radial distance from centerline
P	Intraluminal Pressure
τ	WSS (Wall Shear Stress)
λ	Plasma layer thickness
Q	Flow rate of blood in arteriole
μ_c, μ_p	Core blood viscosity and plasma viscosity
H_c, H_d	Core and systemic hematocrit
J	Pressure Gradient
R_{eq}	Equilibrium inner radius at baseline pressure
CO	Cardiac Output
VR	Vascular Resistance
r_g, $r_e n$, r_w, r_m	Radial distances to outer edge of glycocalyx, endothelium, vascular wall and s

2.2 Mathematical Model

2.2.1 Simulation domain

We consider an arteriole with vascular wall tethered to adjoining connective tissue, which prevents axial motion of the blood vessel [139]. The arteriole is modeled as

a thick cylinder composed of an isotropic, elastic material [20, 189]. We describe both the passive radial deformation of the vessel under internal pressure (i.e., the passive response of the arteriole to intraluminal blood pressure) and the myogenic response of the vessel walls to this pressure, which acts to reduce vessel diameter as intraluminal pressure increases [82]. Blood flow within the arteriole is assumed to be a two-layer flow, consisting of an RBC rich core and a plasma layer devoid of RBCs [172, 182, 199]. The arteriole is assumed to be surrounded by easily deformable tissue, which exerts negligible compressive stress on the vessel walls.

2.2.2 Blood flow

We consider steady one-dimensional flow in a cylinder (arteriole) of radius R. Blood is modelled as a two-layer fluid, consisting of an RBC-rich core and a plasma layer (Fig. 2.1). Following [102, 182], we assume a linear relationship between the plasma layer thickness δ and systemic hematocrit H_d,

$$\delta = a_3 H_d + a_4 \tag{2.1}$$

where a_3 and a_4 are fitting parameters. Data relating CFL thickness with H_d is plotted in appendix A.
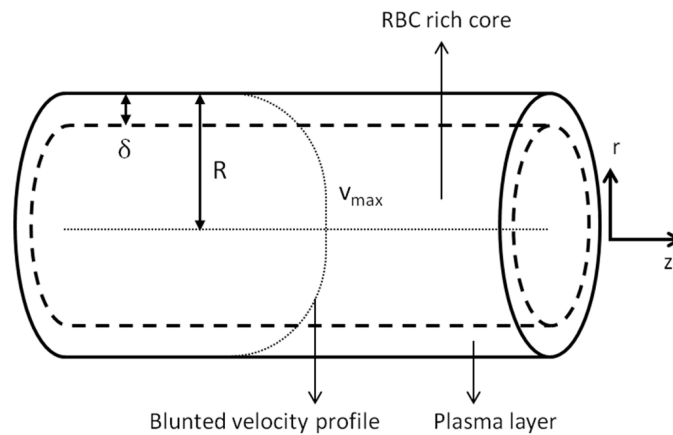
Figure 2.1: Two-layer flow of blood in a cross section of an arteriole with a cell free layer and RBC rich core, resulting in a blunted velocity profile.

Assuming steady-state fully developed flow in the inertial regime for the two-layer

flow of blood through the arteriole, the Stokes equations yield velocities of the core, u_c, and plasma, u_p, as [172], [182]:

$$u_c(\xi) = \frac{JR^2}{4\mu_p} \left\{ 1 - \lambda^2 + \frac{\mu_p}{\mu_c}(\lambda^2 - \xi^2) \right\} \text{ for } 0 \leq \xi \leq \lambda \tag{2.2}$$

$$u_c(\xi) = \frac{JR^2}{4\mu_p} \left\{ 1 - \xi^2 \right\} \text{ for } \lambda \leq \xi \leq 1 \tag{2.3}$$

Velocity profiles 2.2 and 2.3 are written in the dimensionless coordinate system $\xi = r/R$ with $\lambda = r_h/R$; and $J = \Delta P/L$ is the pressure gradient along the arteriole of length L and with pressures drop ΔP respectively. μ_c and μ_p are the viscosities of core blood and plasma, respectively. We make use of an experimentally obtained linear relationship for blood viscosity in the RBC-rich core as a function of H_c (30,51): $\mu_c = a_1 H_c + a_2$, where the constants are set to $a_1 = 0.1678$ and $a_2 = -4.4348$ cp. λ, is given as:

$$\lambda = 1 - \delta/R. \tag{2.4}$$

Flow rate Q is obtained by integrating the velocity profile given by expressions 2.2 and 2.3 over the cross-section of the arteriole with dimensionless radius $\xi = 1$ [172, 182],

$$Q = \frac{\pi JR^2}{8\mu_p} \left\{ 1 - \lambda^4 + \frac{\mu_p}{\mu_c}\lambda^4 \right\} \tag{2.5}$$

The corresponding WSS τ is given by

$$\tau = JR/2. \tag{2.6}$$

The systemic (H_c) and core (H_d) hematocrits are related by mass conservation as [102], [182]:

$$H_c \int_0^\lambda u_c(\xi)\xi d\xi = H_d \left[\int_0^\lambda u_c(\xi)\xi d\xi + \int_\lambda^1 u_p(\xi)\xi d\xi \right]. \tag{2.7}$$

For the velocity profile given by expressions 2.2 and 2.3, this gives

$$H_d = 2H_c\lambda^2(1 - \lambda^2 + \lambda^2\frac{\mu_p}{2\mu_c})(1 - \lambda^2 + \lambda^2\frac{\mu_p}{\mu_c})^{-1}. \qquad (2.8)$$

The positive root of equation [2] yields a relationship between H_c and H_d which is approximately linear over a physiologically relevant range of H_d [182]. For a constant flow rate of blood Q, WSS τ was shown to be linearly related to systemic hematocrit H_d, with $R^2 = 0.997$ in a previous study [182].

2.2.3 Vessel mechanics

Following [20, 21, 170], we assume the vessel to be elastic and to exhibit both active and passive responses to blood flow. The elastic model treats the blood vessel as a tethered cylinder, i.e., neglects strain in the axial direction [167], and postulates a linear relationship between the radial strain u and the radial (σ_r) and circumferential (σ_θ) components of the stress tensor on the vessel walls [189, 199]:

$$u(r) = \frac{r}{E}[\sigma_\theta(1 - \nu^2) - \nu\sigma_r(1 + \nu)]. \qquad (2.9)$$

Here $r \in [R, R_o]$ is the radial distance from the vessels centreline, which varies between the inner (R) and outer (R_o) radii of the vessels walls; E is the elastic modulus of the blood vessel; and ν is the Poisson ratio. We assume that E is constant [20] and that the vessel wall is incompressible. The latter assumption is justified by the high water content of the tissue [189, 199] and allows us to set $\nu = 0.5$ in all simulations reported below.

The vessels active and passive responses to blood flow are modelled by representing the radial and circumferential components of shear stress, $\sigma_r = \sigma_{rp} + \sigma_{ra}$ and $\sigma_\theta = \sigma_{\theta p} + \sigma_{\theta a}$, as the sums of their respective passive (denoted by the subscript p) and active (denoted by the subscript a) components. The passive response represents the stress induced by blood flow on the vessels wall. The corresponding components of the mechanical stress are derived from Lames equations as [189]

$$\sigma_{rp} = \frac{R^2 P}{R_0^2 - R^2}(1 - \frac{R_0^2}{r^2}). \qquad (2.10)$$

$$\sigma_{\theta p} = \frac{R^2 P}{R_0^2 - R^2}(1 + \frac{R_0^2}{r^2}). \tag{2.11}$$

where P is the intraluminal blood pressure. The active (myogenic) response accounts for the Bayliss effect, which acts to reduce the vessels radius in response to increasing pressure [39, 82]. It is assumed to be linearly proportional to the tension at the surface of the vessel wall, $PR/2$, such that [39, 82]

$$\sigma_{ra} = \frac{R^2 P}{R_0^2 - R^2}(1 - \frac{R_0^2}{r^2})\frac{-\phi CPR}{R_{eq}}. \tag{2.12}$$

$$\sigma_{\theta a} = \frac{R^2 P}{R_0^2 - R^2}(1 + \frac{R_0^2}{r^2})\frac{-\phi CPR}{R_{eq}}. \tag{2.13}$$

where R_{eq} is the vessel radius at equilibrium at baseline pressure, C is a fitting parameter, and

$$\phi = tanh(\frac{\alpha}{\tau}). \tag{2.14}$$

represents the modulation of the myogenic response by the WSS (which is normalized with a fitting parameter α) [91]. Expressions 2.11 and 2.14 account for experimental observations [85], according to which large values of WSS reduce the strength of the myogenic response.

2.2.4 Model closure

To close the system of equations 2.1 - 2.14, we employ the experimental observations [62] and the modelling assumption in [21], according to which changes in pressure gradient J in the arteriole are directly proportional to changes in intraluminal pressure P,

$$\Delta J \propto \Delta P. \tag{2.15}$$

This assumption is also justified by the role of autoregulation in ensuring a relatively constant hydrostatic capillary pressure [82, 45], which implies that larger MAPs
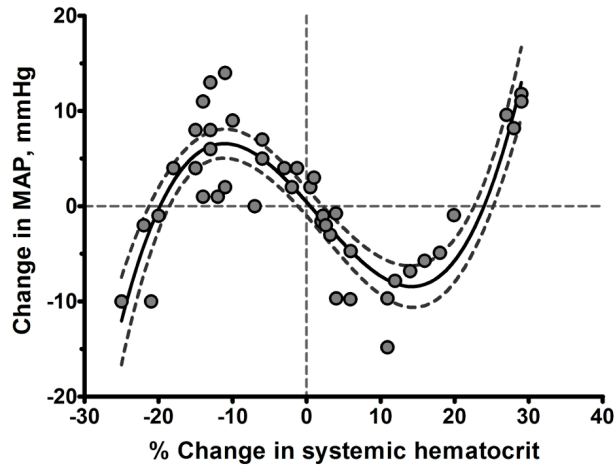
Figure 2.2: Experimental measurement of variation of MAP with small changes in hematocrit from baseline [116, 117, 195]. The same result was obtained for CD-1 mice, but not in eNOS-knockout mice [116].

(and hence larger intraluminal pressures) necessitate larger blood pressure gradients in arterioles.

Finally, we allow for variation of the intraluminal pressure P with H_d. We adapt a relationship in Figure 2.2 that mirrors the experimentally observed [21, 116] response of MAP (and, hence, intraluminal pressure) to small but acute changes in Hct during both hemoconcentration and hemodilution. The change in MAP (and, consequently, in intraluminal pressure P) from baseline with systemic hematocrit, H_d is given by

$$\Delta P = 0.01996 H_d^3 - 2.7048 H_d^2 + 120.32 H_d - 1758.8. \tag{2.16}$$

2.2.5 NO Production

Shear-induced NO production: The experimental data [118, 122] suggest that, for physiological levels of shear stress, the endothelial NO production varies approximately linearly with the WSS τ. We model this phenomenon by assuming that NO production follows Michaelis-Menten kinetics [23], so that the corresponding reaction rate R_e is given by

$$R_e = \frac{R_{NOm}P_{O2}}{P_{O2} + K_m}.$$ (2.17)

Here the maximum rate of NO production R_{NOm} increases linearly with τ, PO2 is the partial pressure of oxygen, and the value of the Michaelis-Menten constant K_m is given in Table A.1.

Stretch-induced NO production: The data reported in [8, 98] show that not only WSS τ but also mechanical stretch of the endothelium affects NO production. Furthermore, the experimental evidence [101] suggests that circumferential stretch increases NO production even when the WSS is kept constant. In the absence of detailed quantitative studies of this phenomenon, we assume that R_{NOm} is proportional to small variations of the vessel radius.

Combining these two mechanisms of NO production, we postulate that R_{NOm} responds to mechanical forces according to

$$R_{NOm} = R_{NOmax}\, \tau \left(1 + \frac{\Delta R}{R_{eq}}\right)^L.$$ (2.18)

where L is a fitting parameter and the constant R_{NOmax} is given in Table A.1. The simulation results presented below suggest that the stretch-induced mechanism is crucial to the vasodilatory activity of NO.

2.2.6   NO transport

We rely on the Krogh tissue model (Figure 2.3) to describe the various layers comprising vessel tissue and lumen, and on a system of reaction-diffusion equations [102, 182] to model radial (one-dimensional) transport of NO across these layers. Parameters for NO transport are given in table A.1.

RBC-rich core ($0 < r < R - \delta$). Partial pressure of oxygen P_{O2} is assumed to be constant [102], and NO concentration CNO satisfies a steady-state reaction-diffusion equation

$$\frac{D_{NO}}{r}\frac{\partial}{\partial r}(r\frac{\partial C_{NO}}{\partial r}) - \lambda_b C_{NO} = 0$$ (2.19)
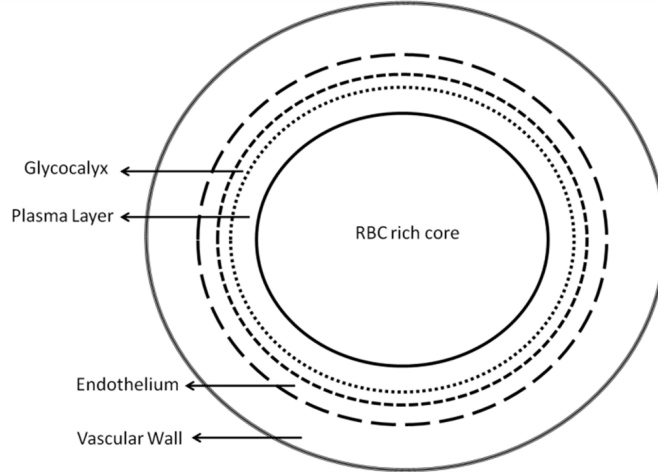
Figure 2.3: Cross-section of an arteriole. A version of the Krogh tissue cylinder model used in our analysis consists of RBC-rich core, RBC-free plasma layer, glycocalyx, endothelium, and vascular wall.

where D_{NO} is the diffusion coefficient of NO in the RBC-rich core, and λ_b is the reaction rate constant of NO scavenging by RBCs. For the value of membrane permeability determined in (58), λ_b is almost constant over the range of physiological Hct [194, 193]. We therefore set λ_b to be constant, specified in Table A.1.

Plasma layer $(R - \delta < r < R)$ and glycocalyx $(R < r < r_g)$. The absence of RBCs in the plasma layer and the glycocalyx allows us to describe transport of C_{NO} and P_{O2} using steady-state diffusion equations:

$$\frac{D_{NO}}{r} \frac{\partial}{\partial r}(r \frac{\partial C_{NO}}{\partial r}) = 0 \tag{2.20}$$

$$\alpha \frac{D_{O2}}{r} \frac{\partial}{\partial r}(r \frac{\partial P_{O2}}{\partial r}) = 0 \tag{2.21}$$

respectively. Here α denotes the O2 solubility, and the diffusion coefficients of NO D_{NO} and O2 D_{O2} in the plasma layer are larger than their counterparts in the glycocalyx and tissue layers [58, 113].

Endothelium $(r_g < r < r_e)$: The rate of oxygen consumption is assumed to be twice the rate of NO production [182, 30, 102]; C_{NO} and P_{O2} satisfy a coupled system of steady-state reaction-diffusion equations

$$\frac{D_{NO}}{r}\frac{\partial}{\partial r}(r\frac{\partial C_{NO}}{\partial r}) + R_e = 0 \tag{2.22}$$

$$\alpha\frac{D_{O2}}{r}\frac{\partial}{\partial r}(r\frac{\partial P_{O2}}{\partial r}) - 2R_e = 0 \tag{2.23}$$

Vascular wall ($r_e < r < r_w$) and smooth muscle tissue ($r_w < r < r_m$): Following [23, 30], we assume that NO undergoes a pseudo-first-order reaction with reaction rate constant λ_t, and that O2 consumption is inhibited by NO and follows Michaelis-Menten kinetics. The corresponding transport equations take the form

$$\frac{D_{NO}}{r}\frac{\partial}{\partial r}(r\frac{\partial C_{NO}}{\partial r}) - \lambda_t C_{NO} = 0 \tag{2.24}$$

$$\alpha\frac{D_{O2}}{r}\frac{\partial}{\partial r}(r\frac{\partial P_{O2}}{\partial r}) - R_m = 0 \tag{2.25}$$

where peak O2 consumption rate R_{O2max} is lower in the vascular wall than in the muscle tissue, and [23, 30]

$$R_m = \frac{R_{O2max}P_{O2}}{P_{O2} + K_{MO2}} \tag{2.26}$$

$$K_{MO2} = 1 + \frac{C_{NO}}{27nM} \tag{2.27}$$

2.2.7 Boundary Conditions

Transport equations 2.19 - 2.25 are subject to the following boundary conditions. NO concentration C_{NO} is symmetric about the arteriole center , $r = 0$

$$\frac{\partial C_{NO}}{\partial r}(r = 0) = 0 \tag{2.28}$$

We assume that both C_{NO} and P_{O2} reach their respective asymptotic concentrations in the vicinity of the outer boundary of the muscle tissue, $r = r_m$, so that [102]:

$$\frac{\partial C_{NO}}{\partial r}(r = r_m) = \frac{\partial P_{O2}}{\partial r}(r = r_m) = 0 \tag{2.29}$$

Mass conservation across the interfaces between adjacent layers requires that:

$$C_{NO}^+ = C_{NO}^-; \; P_{O2}^+ = P_{O2}^-; \; (D_{NO}\frac{\partial C_{NO}}{\partial r})^+ = (D_{NO}\frac{\partial C_{NO}}{\partial r})^-; \; (D_{O2}\frac{\partial P_{O2}}{\partial r})^+ = (D_{O2}\frac{\partial P_{O2}}{\partial r})^-$$

$$(2.30)$$

where the superscripts minus and plus indicate that the corresponding quantities are computed respectively inside and outside of each interface shown in Figure 2.1.

2.3 Numerical implementation

2.3.1 Autoregulation

Step 1. For a given value of Hct and ignoring the shear term ϕ in equations 2.12 and 2.13, we determine the constant C from the experimental data for myogenic response in vessels either with denuded endothelium [55] or in the absence of flow [85, 170]. The iterative procedure to determine the constant C in equations 2.12 and 2.13 is as follows.

1. Assume an initial value for the parameter C. We used an initial guess $C = 0$, which corresponds to purely elastic, passive behavior.

2. Use equations 2.9 and 2.13 to calculate the deformation of the vessel for each of the incremental increases in pressure from 50 mmHg to 60 mmHg. We used the increment $\Delta P = 0.001$ mmHg

3. Compute the slope of the resulting (approximately) linear relationship between vessel radius and pressure.

4. Compare the calculated slope with that estimated from experimental data, in this study the data from (22, 46). If the absolute difference between the calculated and experimentally observed slopes exceeds a prescribed tolerance ϵ_1, increase C by Δ_1. We used $\epsilon_1 = 10^{-3}$ and $\Delta_1 = 0.01$.

5. Repeat steps b) - d) until the convergence criterion is met.

Step 2. Once the value of C is computed, we account for shear stress. Specifically, we determine the constant α in equation 2.14 by enforcing autoregulation, i.e.,

the condition that flow rate Q in equation 2.5 remains constant with small changes in pressure. The iterative procedure to determine the constant α in equation 2.14 is as follows.

1. Assume an initial value for the parameter α. We used a initial guess of $\alpha = 0$, which corresponds to a situation wherein WSS completely eliminates myogenic response.

2. Use equations 2.9 - 2.14 to calculate the deformation of the vessel for each of the incremental increases in pressure from 50 mmHg to 60 mmHg.

3. Compute the flow rate Q corresponding to each value of pressure by using equations 2.1 - 2.5 and 2.10 - 2.13. Plot the resulting flow rate vs pressure curve.

4. If the curve has a non-zero (up to a prescribed tolerance ϵ_2) slope, increase α by Δ_2. We used $\epsilon_2 = 10^{-4}$ and $\Delta_2 = 0.0001$.

5. Repeat steps b) - d) until the slope is zero (up to a prescribed tolerance ϵ_2), i.e., until flow rate does not change with pressure.

2.3.2 Effect of varying Hct

We prescribe a functional dependence of intraluminal pressure on systemic Hct based on the experimental data [116, 117, 195]. For the parameters C and α computed in Steps 1 and 2, we calculate the vessels response to changes in systemic Hct by using the following algorithm.

1. Increase systemic hematocrit Hd by a small increment $\Delta H = 0.001\%$.

2. Use equation 2.16 to compute the new pressure for the new value of H_d.

3. Use equation 2.14 and 2.15 to calculate J and ϕ.

4. Use equations 2.9 - 2.13 to calculate the new vessel radius and thickness.

5. Use equations 2.1 - 2.5 to calculate the new flow rate, Q.

6. Repeat steps a) - e) to obtain a relationship between the flow rate and H_d
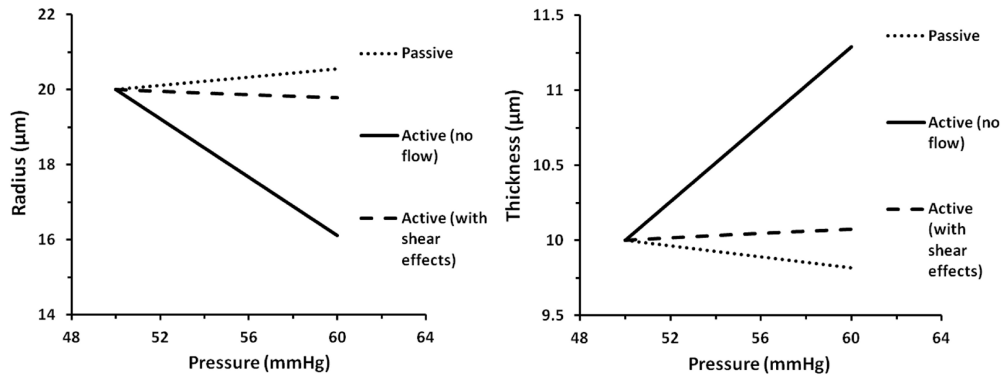
Figure 2.4: a) Variation of vessel radius with pressure, and, b) Variation of vessel thickness with pressure for different mechanical responses.

2.4 Results

Changes of vessel diameter with pressure. Figure 2.4a shows the variation of the arteriole inner radius with increasing intraluminal pressure. When the myogenic response is ignored (i.e., when only the passive response is considered) the vessel radius increases linearly with pressure. Conversely, including the myogenic response causes the arteriole radius to decrease. Ignoring the shear effects (and hence the endothelial NO production) enhances the strength of the myogenic response modulated by WSS [85, 131]. Setting $C = 8$ in equations 2.10 - 2.13 yields an active (no flow) response that matches well with the experimental data [110, 137, 169]. Figure 2.4b exhibits the corresponding variation in the vessel wall thickness. The passive and active mechanical responses to the small changes in pressure lead to a linear relation between the vessel radius and pressure. This finding is in agreement with the experimental data [110, 137, 169], providing a justification for the assumption that the vessel behaves like a linear, elastic material for small variations in intraluminal pressure.

Figure 2.5 illustrates the dependence of flow rate on intraluminal pressure, for several values of the parameter α in equation 2.14. For $\alpha = 0.1434$, the flow rate remains constant with small changes in pressure. This establishes autoregulation, which results from a balance between the relative strengths of the passive (elastic) and active (myogenic) responses in the blood vessel, with shear stress modulating active response. In

this autoregulatory regime, the vessel radius decreases marginally as pressure increases; small reductions in the vessel radius offset the increase in both pressure gradient and, according to equation 2.15, pressure; this process results in the approximately constant flow rate.
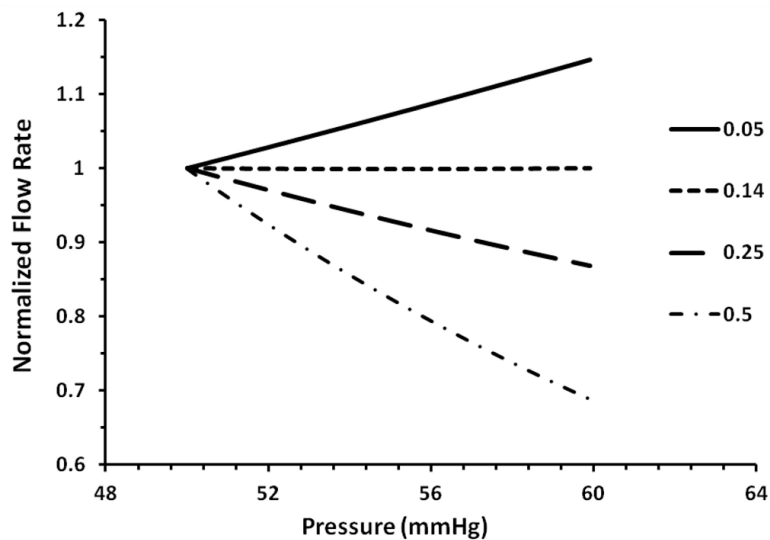
Figure 2.5: Effect of varying the parameter α on the dependence of flow rate with intraluminal pressure.
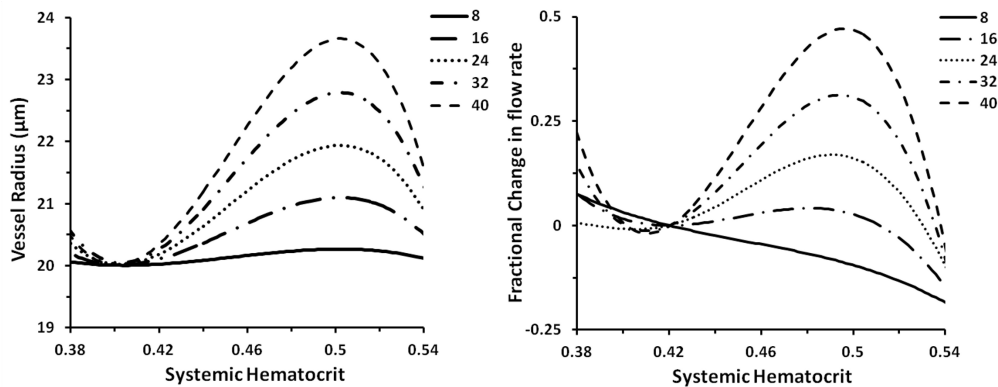
Figure 2.6: a) Variation of vessel radius, and, b) Flow rate with hematocrit for different strengths of myogenic response, governed by the parameter C in eq. 7.

2.4.1 The effect of varying Hct

Figures 2.6a and 2.6b demonstrate the dependence of both vessel radius and flow rate on systemic Hct, for pressure varying with Hct in a manner described in [116, 117, 195]. When all parameters are selected to ensure autoregulation (corresponding to constant Hct), we find that flow rate decreases significantly with Hct. This finding is supported by the experimentally observed variation of cardiac output with Hct [163], but is at odds with the experimental results in [116, 117, 195]. The predicted reduction in flow rate can be attributed to the increase in blood viscosity with Hct while vessel dilation remains negligible. For larger values of C in equations 2.10 - 2.13, i.e., for stronger myogenic response, the variation in flow rate with Hct resembles the behavior reported in [116, 117]. Stronger myogenic response offsets autoregulatory control by changing the balance between the active and passive components of mechanical stress in the vessel walls. This suggests that during acute hemoconcentration and hemodilution, the ability to autoregulate was offset; similar to previously reported data for cerebral tissue exposed to hemodilution [132, 175].

Figure 2.7 exhibits the corresponding variation in vascular resistance (cardiac index divided by blood pressure) (Figure 2.7a) and WSS (Figure 2.7b) with increasing Hct. For values of C, which predict variations in flow rate similar to those in [116, 117, 195], our model predicts a large reduction in vascular resistance and significant increases in WSS. This increases NO production and contributes to vasodilation. The predicted U-shaped curve for variations in vascular resistance is in agreement with calculations from experimental data [116, 117, 195]. Figure 2.8 presents experimental measurements of the dependence of vascular resistance on systemic hematocrit, accompanied by the model predictions for $C = 32$ in equations 2.10 - 2.13.

2.4.2 Analysis of NO concentration

Figure 2.9 illustrates the variation in NO concentration for different values of L in equation 2.18. This parameter controls the extent of stretch-induced NO production. For $L = 0$, i.e., in the absence of stretch-induced NO production, NO concentration in the vessel wall falls marginally as radius increases. This decrease in NO concentration
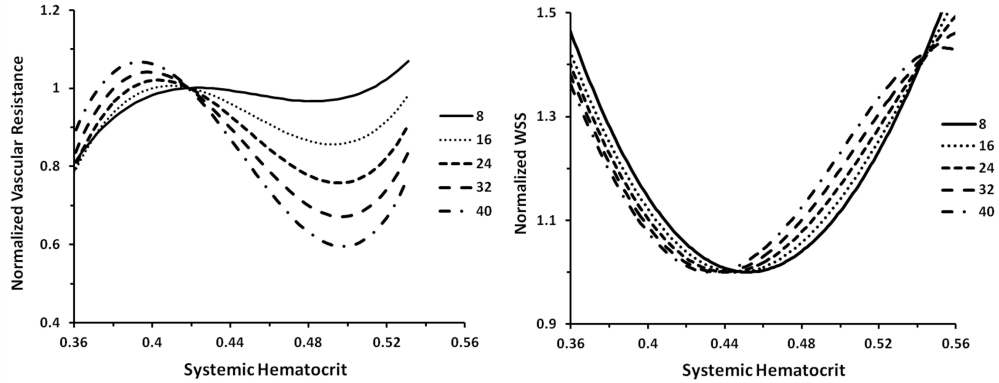
Figure 2.7: Variation of a) Vascular resistance, and, b) WSS with Hct for different strengths of myogenic response, governed by the parameter C in eqs 2.10 - 2.13.

occurs because the increasing vessel radius increases the surface area across which NO diffuses into the blood-stream and is scavenged by RBCs. This causes NO bioavailability to fall, since the blood-stream scavenges NO at a high rate [102] and because NO has higher diffusivity in blood than in tissue [58].

In other words, the increasing radius enhances diffusion of NO produced by the endothelium into the blood-stream where it is consumed by RBCs, as opposed to its diffusion into surrounding tissue. The net effect is to reduce NO bioavailability in the vessel walls. Higher values of L, i.e., higher stretch-induced NO production, result in an increase of NO concentration with stretch [98]. Clearly, for NO to have a role as a vasodilator in this system, stretch-induced NO production must be significant. For this study we take $L = 1$ as a representative value quantifying stretch-induced NO production.

Figure 2.10a exhibits the variation of average NO concentration with Hct for different values of C in equations 2.10 - 2.13. This parameter represents the strengths of active response, as seen in Figure 2.6a; $C = 48$ results in a flow vs. Hct relation that closely matches the results of [116, 117]. Figure 2.10a illustrates the action of NO as a vasodilator in this system, with larger vessel radii corresponding to larger NO concentrations. To illustrate the importance of stretch-induced NO production on the vasodilatory role of NO, we plot the variation of NO concentration with Hct for $C = 48$ and different values of the parameter L in equation 2.18. In the absence of stretch-

induced NO production, NO bioavailability in the vessel wall actually drops, reinforcing the idea that stretch-induced NO production is necessary for endothelial NO production to stimulate vasodilation in this system (Figure 2.10b).
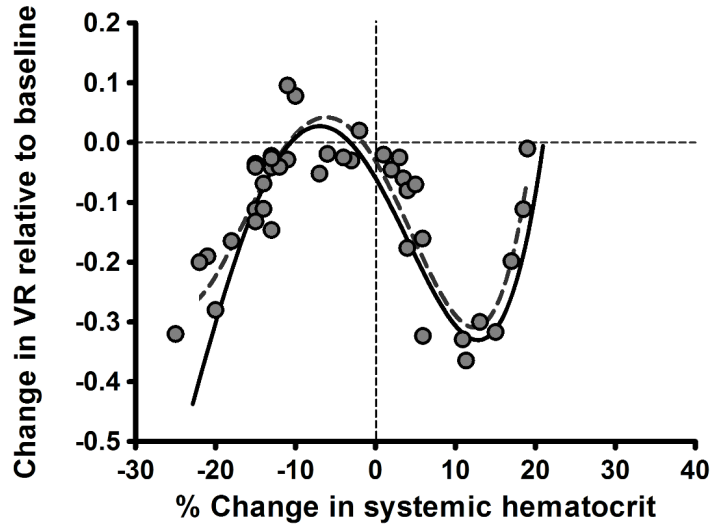
Figure 2.8: Change in Vascular Resistance (VR) with systemic Hct for $C = 32$ (solid line) and experimental data [116, 117, 195] (dashed line).

Table 2.1: Model Parameters for Vessel Mechanics

Parameter	Symbol	Value	Reference
Unstressed Arteriole diameter	R	20 μm	[102, 30, 182]
Elastic Modulus of Vessel Wall	E	10000 N/m^2	[15]
Stretch Induced NO Exponent	L	1	(refer text)
Myogenic Parameter	C	8 - 48	(refer text)
WSS autoregulation fitting parameter	α	0.1434	(refer text)

2.5   Discussion

We present a model for vessel mechanics that incorporates elastic response and myogenic response modulated by shear effects, for small changes in pressure and Hct. Comparison with the experimental data [116, 117, 195, 163] demonstrates that our model is capable of reproducing both active and passive responses of the arteriole over the range of pressure used in these experiments.
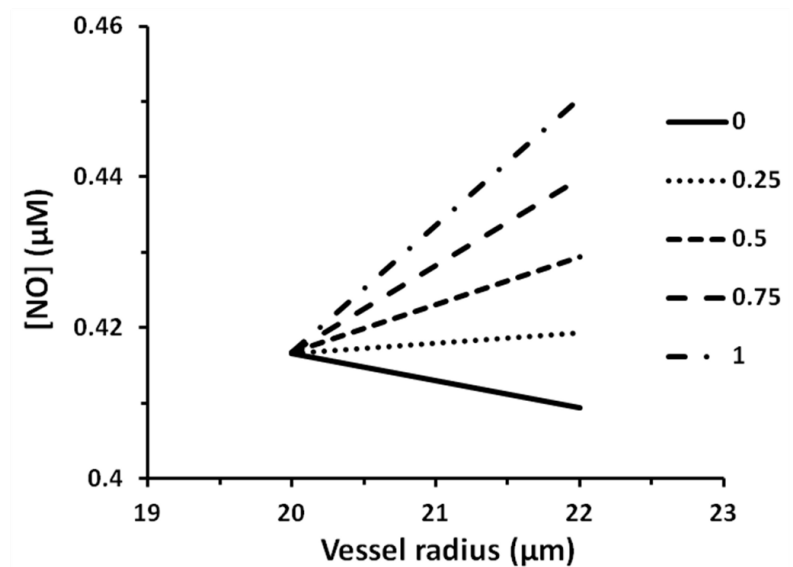
Figure 2.9: Effect of the parameter L in equation 2.18 on variation of NO concentration with vessel radius.
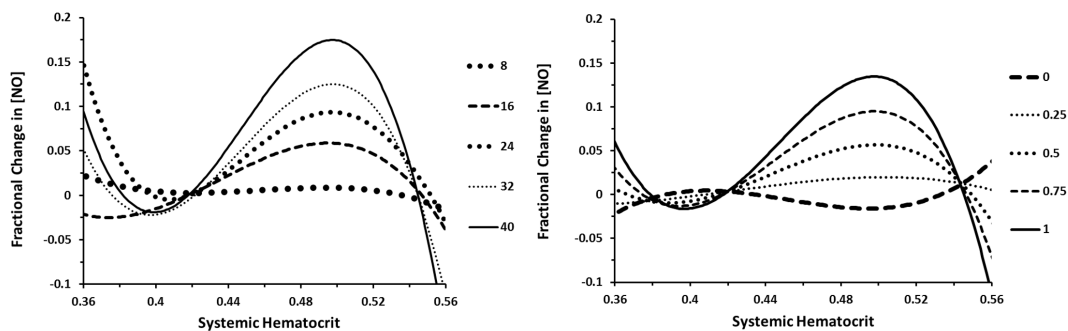
Figure 2.10: a) Fractional change with systemic hematocrit of average NO concentration in the vessel wall for different values of the parameter C in eqs 2.10 - 2.13 (and hence different strengths of myogenic response) with $L = 1$ in eq 2.18.; b) Fractional change with systemic hematocrit of NO concentration for different values of L in eq. 2.18 with $C = 32$.

Our model assumes that the primary contributing factor to NO bioavailability in the vasculature is endothelial NO production stimulated by WSS and stretch [8] due to increased activation of eNOS, and focuses on the effects of coupled of shear and myogenic responses on the autoregulation of blood flow. Figures 2.6 and 2.9 demonstrate that our model accounts for the effect of this change in NO concentration (produced by the WSS-stimulated endothelium) on the myogenic response [85, 101, 131], and show how NO concentration varies with WSS and vessel stretch.

Our results suggest that, in the range of pressure studied, a simple Hookean model for arteriolar mechanics is adequate to describe the passive and active responses of blood vessels, with myogenic response modelled by equations 2.10 - 2.13 as a function of tension in the vessel wall. Leveraging the thick-cylinder theory; our model accounts for variations in wall thickness as well as changes in the vessels inner radius. Employing the existing models of blood flow in arterioles [172, 182], the model couples the solid mechanics governing vessel deformation with the hemodynamics of arteriolar blood flow and relates changes in pressure to changes in flow rate. The two-layer fluid flow model used in this study accounts for the presence of a discrete plasma layer. An area of interest for future study is to understand how variations in plasma layer thickness and viscosity [190] influence this autoregulatory behavior. As shown in appendix B, our results for variations of flow rate with Hct are relatively insensitive to the choice of rheological model, justifying the selection of a simple 2-layer Newtonian model for blood flow used in this study.

Combined with the experimentally determined dependence of pressure on Hct [116, 117, 195], our model sheds new light on how variations in Hct affect the flow rate in an arteriole (and hence CO). We find that this variation is heavily dependent on the balance between active (myogenic) and passive (elastic) responses (controlled by the parameter C in equations 2.10 - 2.13). When these active and passive responses are balanced and achieve autoregulation (for constant Hct), the blood flow rate drops significantly as Hct increases. This behavior is due to the sharp increase in blood viscosity with increasing Hct [152]; it is in agreement with earlier studies [163], which report a linear decrease in cardiac output with increasing Hct. We also demonstrate that the nonlinear behavior reported in [116, 117, 195] is likely due to an offset in the balance

between the active and passive responses, with the active (myogenic) response dominating (see Figure 2.6). This sharper active response results in arteriolar dilatation (for reductions in pressure) and hence in increased flow rate. Previous studies [132] suggest a similar change in autoregulatory behavior in cerebral tissue for mild hemodilution.

The origin of this increased active response is a matter for future study. Possible explanations include this being a transient effect, since the mechanical response of blood vessels [15, 14, 52] and NO production [118, 122] vary with time; other aspects of the experimental procedure, such as the effect of anesthesia on muscle tone; or other stimuli, such as increased activation of the sympathetic nervous system, which has been associated with hemoconcentration [3]. Understanding this unexpected response to acute hemoconcentration is important, as the underlying physiology may be crucial for predicting responses to blood transfusion which are accompanied by acute fluctuations in Hct [69]. Future study in this area (both experimental and theoretical) is needed to better understand cardiac response due to RBC concentration/dilution and the underlying physiology.

We show mathematically that stretch-induced NO production is crucial to the role of NO as a vasodilator (see Figures 2.9 and 2.10). Without this stretch-induced mechanism, increasing vessel radius would cause NO levels in the vessel wall to drop; thereby eliminating the vasodilatory effect of NO. However, with stretch stimulating NO production by the endothelium, it is possible for NO levels to rise and be maintained at a higher level (relative to some baseline) as vessel radius is increased. This suggests the need for further study of stretch-induced NO production, especially in order to obtain more rigorous mathematical models of changes in NO production in response to changes in stretch. The importance of shear-induced NO production is qualitatively illustrated by the resulting NO bioavailability (Figure 2.6b). Figures 2.6a and 2.10a show a relationship between NO bioavailability and vasodilation. It suggests that, in the range of physiological concentrations, there exists a simple constitutive relationship between NO concentrations in the vascular wall and the extent of modulation of myogenic responses.

The curves for NO concentration, flow rate and vascular resistance lead us to conclude that the physiological response to Hct variations occurs as a result of the com-

bination of mechanical (i.e., fluid mechanics of blood flow and solid mechanics of vessel walls) and biochemical (i.e., metabolic factors and the vasodilatory effect of NO) effects. Each aspect influences the other since mechanical changes cause WSS variations, which in turn influence the biochemistry within the vessel wall (by increasing NO concentrations), which in turn influences the mechanical side of the problem by altering the strength of the Bayliss effect and hence changing vessel mechanics and blood flow. The result is a complex balance between various, often competing mechanical and biochemical processes.

A hamster experimental study [195], in which the increase in Hct was induced by transfusing RBCs whose Hb was converted to metHb and therefore did not scavenge NO, elucidates the role of changes in NO bioavailability due to the increased WSS. Increasing blood viscosity with metHb RBCs significantly extended the range of Hct increase before causing hypotension, since the increase of volume (concentration) of RBCs did not increase the rate of NO scavenging by Hb. In addition to these data, the paradoxical response of cardiac function to acute Hct variations was not observed in eNOS knockout mice [116, 117]. This finding further strengthens the hypothesis that the physiological response to Hct variations discussed in this study is strongly influenced by endothelial NO production and its increase due to increased WSS.

These results serve to explain in part the perception that the transfusion of a single unit blood could be of benefit, even though in general it is of little significance in terms of changes of oxygen carrying capacity. Furthermore, in restrictive transfusion practice it could help decide whether to transfuse a single unit or two units. This is because transfusion of a unit of blood increases hemoglobin (i.e., Hct) by 1 g/dl or 7 %, which is the range of the maximal reduction of VR, while two units or 14 % place the circulation in the range where VR increases above baseline [111]. These simplified calculations are based on Hct 45 % (Hemoglobin 14 g/dl), which would not justify a blood transfusion and assumes an isovolemic change in Hct that does not occur in blood transfusions. Moreover, they are derived for our experimental model where a scaling between experimental and human conditions has not been established.

In conclusion, our study establishes a mathematical model for the pressure response of arterioles by extending previous models [82, 169] and coupling this mechanical

response with fluid flow within an arteriole that treats blood as a two layer fluid with the presence of a distinct plasma layer. Applying this framework to model the regulatory response of arterioles with changes in Hct resulted in calculated variations in CO that match experimental data, depending on model parameterization. We find that the reported anomalous variations in CO [116, 117, 195] are due to the combination of increased NO production and bioavailability by the increased WSS and a shift in the balance between passive and active mechanical responses of the arteriole affecting the autoregulatory response. These results have considerable implications for understanding physiological response to acute Hct variations associated with blood transfusion and blood losses, since they suggest a significant increase in perfusion following a modest increase in Hct associated with the infusion of a unit of packed RBCs that is independent of the change in oxygen carrying capacity.

2.5.1 Model limitations and scope for future work

1) Our model neglects transient effects in both viscoelastic response of arteriole walls [21] and NO production in response to changes in WSS [118, 122]. These mechanical and biochemical phenomena suggest that modulation of the myogenic response by shear effects is time dependent.

2) Shear-induced NO production has steady and transient components; acute changes in WSS induce gradual changes in NO production, until a new steady state is reached [118, 122]. This effect can be analyzed by including a time dependent decay function for the transient element of shear induced NO production in equation 2.18, which relates NO production with WSS. Incorporation of these transient effects will establish the time scales needed for the system to reach the steady state examined in this study.

3) The arteriole has been modeled as an isotropic material with constant elastic modulus. However, arterioles elastic modulus in the longitudinal direction is higher than its counterpart in the circumferential direction [52]. Future studies will account for this anisotropy. Furthermore, arterioles elastic modulus is not constant, but varies with radius. For small deformations, this is not a significant problem, however for larger deformations (and variations in pressure), this variation of elastic modulus with radius

might become important.

The thick-cylinder theory employed in our analysis can be used in follow-up studies to better understand the mechanical behavior of the vessel wall, such as the effects of Poissons ratio of the vascular wall on vessel deformation [167].

4) Our study deals with a single arteriole rather than a network of blood vessels. Future studies of autoregulation in networks of blood vessels would provide a more realistic picture of autoregulation in a whole organ [156]. Completion of the description of the autoregulatory behavior of an entire network requires accounting for long-range "conducted" responses, whereby signals from individual blood vessels are conducted to neighboring vessels ultimately coupling the responses of most vessels. Thus, dilation/constriction of upstream large vessels results in corresponding dilation/constriction of vessels downstream. This effect can be accounted for by introducing an additional component into the active response component of our model, so that active stresses are also a function of signals conducted from other points in the network.

5) Future refinements of our model will also account for the action of vasoactive substances other than NO, e.g., the release of endothelin (a powerful vasoconstrictor which counteracts the dilatory effects of NO) from the endothelium and the release of prostacyclin (another potent vasodilator).

6) To make these studies relevant to conditions of transfusion medicine, it will be important to repeat the analysis and experimental program to deal with changes of Hct in animals that are at lower Hct baseline, as would be the case in medical practice.

2.6 Acknowledgements

This Chapter is a reprint of the material as it appeared in:

K. Sriram, B. Y. Salazar Vazquez, A. G. Tsai, P. Cabrales, M. Intaglietta, and D. M. Tartakovsky. Autoregulation and mechanotransduction control the arteriolar response to small changes in hematocrit. Am. J. Physiol. Heart Circ. Physiol.,

303(9):H1096-1106, 2012.

Chapter 3

PEG-albumin supra plasma expansion is due to increased vessel wall shear stress induced by blood viscosity shear thinning

3.1 Introduction

Hemodilution with conventional plasma expanders (including colloids) beyond a hematocrit (Hct) reduction of about 60 % decreases functional capillary density and blood flow. This problem can be avoided by using high viscosity plasma expanders, such as high molecular weight dextrans and alginates, which elevate plasma viscosity to about 2 cP [192]. This effect is due to increased vessel-wall shear stress (WSS) and NO bioavailability [26, 192]. Plasma expansion with polyethylene glycol conjugated albumin (PEG-Alb) shows the same effects as high-viscosity plasma expanders. This is despite the fact that (in hamsters) the plasma viscosity of about 1.3 cP - measured after hemodilution with 4 % PEG-Alb by weight (about 1

The low plasma viscosity attained with PEG-Alb hemodilution indicates a low WSS. It also suggests that PEG-Alb may operate via a mechanism other than the WSS-

based biochemical mechano-transduction, which causes flow-dependent vasodilatation in high-viscosity plasma expansion [124, 177]. The latter mechanism would be possible if plasma containing PEG-Alb behaved like a Newtonian fluid whose rheology were independent of shear rate. However, both PEG-Alb and PEG-Alb blood mixtures exhibit high viscosity at low shear rates and vice versa, a property that is known as shear thinning. Transfer of shear stress from the red blood cell (RBC) blood column core to the periphery of the flowing blood can increase WSS. A blood velocity profile that is blunted relative the parabolic (Poiseuille) profile typical of Newtonian fluids is a manifestation of such an effect.

To explore the influence of shear thinning on WSS during hemodilution with PEG-Alb, we develop a mathematical model that relies on the rheological properties of blood diluted with 4 % PEG-Alb determined in vitro Our analysis leads to a power-law relationship between WSS and both Hct and the rheological properties of blood/plasma expander mixtures. The latter were measured in blood samples obtained after hemodilution with PEG-Alb, dextran 70 kDa, and dextran 500 kDa of low and high viscosity, respectively. The rationale for this study is to explore the mechanisms of circulatory regulation in anemia and hemodilution. These mechanisms are not apparent in Hct reductions usually encountered under physiological and/or clinical conditions [27, 26]. These studies demonstrate the physiologically beneficial state of supra-perfusion caused by this new form of plasma expansion. They also advance a hypothesis that this condition is a physiological consequence of augmented NO bioavailability. Therefore we relate our findings to perivascular measurements and calculations of the vessel-wall NO concentration and cardiac output.

3.2   Materials

Albumin was conjugated with polyethylene glycol according to the Extension Arm Facilitated protocol (EAF PEGylation) described in [191]. Briefly, lyophilized preparations of albumin (Sigma Aldrich, St. Louis, MO) were subjected to cold ($4°C$) EAF PEGylation for overnight at a protein concentration of 0.5 mM in the presence of 5 mM 2-IT (for thiolation of the protein) using 10 mM maleimidophenyl PEG 5 kDa (cus-

tom synthesized). Under these experimental conditions, on average six-to-seven copies of PEG 5 kDa chains are conjugated to the protein. The hexaPEGylated albumin thus generated was purified through tangential flow filtration and concentrated to a 4 gm % solution with respect to albumin (2 gm % solution with respect to PEG; it is a 6 gm % solution with respect to EAF PEG albumin calculated based on the molecular mass of EAF PEG albumin to be 95 to 100 kDa) and stored at $-80°C$. Dextran solutions were obtained from Pharmacia, Uppsala, Sweden.

3.3   Measurement of hemodiluted blood viscosity

The rheological behavior of blood hemodiluted with plasma expanders was studied experimentally to characterize changes of fluid viscosity with shear rate. The plasma expanders used were: a) 4 % PEG-albumin solution, b) 6 % Dextran 70 kDa solution (a low viscosity plasma expander, or LVPE), and c) 6 % Dextran 500 kDa solution (a high viscosity plasma expander, or HVPE). These fluids were mixed with hamster blood to reproduce the plasma composition after hemodilution to 11 % Hct in previous experiments [192]. In these experiments, plasma was obtained from hamster blood collected in heparinized tubes and centrifuged.

A special protocol was followed in order to compare with in vivo data on extreme hemodilution that included NO measurements [192]. Progressive stepwise hemodilution to a final systemic Hct of 25 % of baseline was implemented with three exchange steps. Level 1 consisted of exchanging 40 % of the blood volume with 6

To measure rheological properties of the suspension, we employed a computerized cone-plate rheometer, AR-G2, (TA Instruments, New Castle, DE) with a 4 cm diameter and 2° angle cone cells. The rheometer was calibrated with the viscosity standards for fluids of low viscosity at $37°C$. The measurements were carried out under standardized temperature conditions ($37°C$) and shear rates between 0.18 and 450 s^{-1} in two steps, first the ascending shear rate and second the descending shear rate.

Plasma viscosities were measured after centrifugation of the suspension only using clean supernatant solution. The measurements were made with a cone-plate LVDV-II (Brookfield Engineering Labs., Middleboro, MA) using a CP-40 spindle. The measure-

ments were carried out at $37°C$ and shear rates between 50 and 450 s^{-1} in two steps, first the ascending shear rate and second the descending shear rate.

Table 3.1: Fitting parameters for the Quemada model for 11 % Hct blood diluted with Dextran 70, Dextran 500 and PEG-Alb plasma expanders to 11 % Hct. Also shown is data for 48 % Hct blood without any plasma expanders present.

Fluid	Plasma Viscosity (cP)	k_0	k_∞	γ_c (s^{-1})
Whole Blood (48 % Hct)	1.2	4.3	2.05	2.8
Blood diluted with Dextran70	1.2	7.1	2.4	6
Blood diluted with Dextran500	2.2	6.2	0.5	1.9
Blood diluted with PEG-Alb	1.3	11.9	0.3	7.3

3.4 Results

Results are shown in Figure 3.1 for blood diluted with the three plasma expanders under consideration. At shear rates below 20 s^{-1}, the blood diluted with PEG-Alb exhibits more pronounced shear-thinning behavior than the blood diluted with either Dextran 70 or Dextran 500. The PEG-Alb diluted blood has greater viscosities than the blood diluted with Dextran based plasma expanders up to a shear rate of 10 s^{-1}. At high shear rates, the viscosity of the PEG-Alb diluted blood is significantly lower. The Quemada rheological model (see equations 3.3 and 3.4 below) was fitted to these data, leading to the viscosity-shear rate curves shown in Figure 3.1. The corresponding fitting parameters are tabulated in Table 4.1.

3.5 Mathematical model of blood flow in arterioles

The mathematical model presented below allows one to compute flow velocity profiles in arterioles, WSS, and core Hct for a given value of systemic Hct. Our model qualitatively captures the blunted blood-velocity profiles observed in experiments [32, 109, 147, 188, 18], predicts the impact of various plasma expanders on WSS, and verifies the hypothesis that the introduction of either Dextran 500 kDa or PEG-albumin increases WSS.
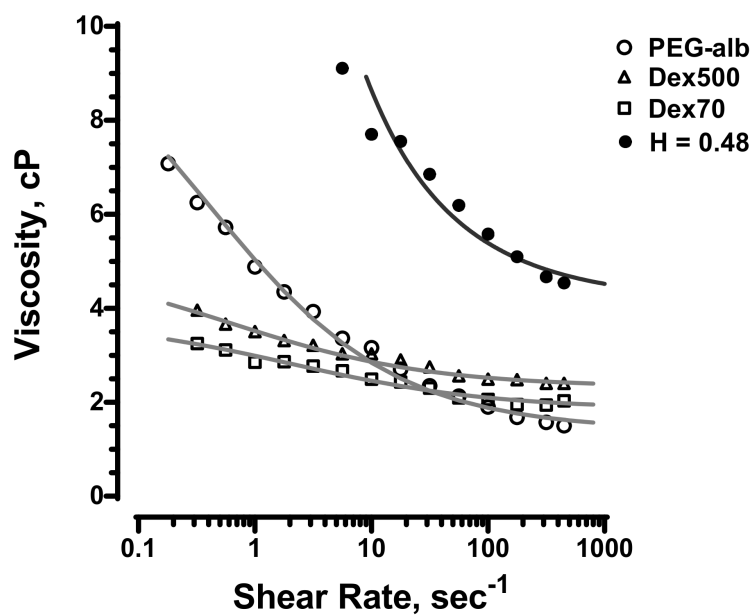
Figure 3.1: Variation of viscosity with shear rate for PEG-albumin, Dextran 70 (LVPE, Dex 70) and Dextran 500 (HVPE, Dex500) solutions mixed with blood, at 11 % Hct, with fitted curves using the Quemada model. Also shown for comparison are curves for whole blood without any plasma expanders present, at 48 % Hct.

Empirical power laws, which are often used to describe velocity profiles in arterioles [18, 94, 109], do not account for changes in the rheological properties of blood caused by Hct variations. To accommodate this phenomenon, we model blood as an inhomogeneous multi-phase fluid [182, 172] that exhibits both a non-uniform radial distribution of Hct in the vessel lumen [109, 147, 203] and a cell-depleted layer near the blood-vessel wall [90]. Non-Newtonian rheology of the RBC-rich core is described with the Quemada constitutive law [114, 157, 144], a three-parameter expression that captures the variation of blood viscosity with shear rate and Hct. Blood plasma is modeled as a Newtonian fluid. We consider pseudo-steady flow regimes, which are typical for arteriole flows characterized by low Womersley numbers [12].

Consider blood flow in an arteriole of fixed radius R. The flow is driven by an externally imposed pressure gradient ,with no-slip boundary and no-flow conditions imposed at the arteriole wall. Blood is modeled as a multi-phase fluid consisting of an inner region densely packed by RBCs and an outer plasma layer with fewer RBCs [30, 109, 147, 203]. The nominal plasma layer thickness δ (normalized with the arteriole radius R) varies linearly with systemic hematocrit H_d [182],

$$\delta = mH_d + c. \tag{3.1}$$

where $m = -7.55$; $c = 6.91/R$ for H_d up to 0.65. We assume that the localized hematocrit H decreases smoothly from its maximum value $H = H_c$ (the core hematocrit) at the arterioles center to $H = 0$ at the arterioles wall according to a sigmoidal curve

$$H(\xi) = H_c tanh(\frac{1-\xi}{a\delta}\pi). \tag{3.2}$$

where $0 \leq \xi < 1$ is the radial distance from the centerline (normalized with R) and a is a fitting parameter. Based on the data reported in [203], we set $a = 4$.

The Quemada rheological model [157, 114] postulates that the effective blood viscosity η varies with the localized hematocrit H and the shear rate γ as

$$\eta = \frac{\eta_p}{(1 - kH_c/2)^2}, \qquad k = \frac{k_0 + k_\infty\sqrt{\gamma/\gamma_c}}{1 + \sqrt{\gamma/\gamma_c}}. \tag{3.3}$$

Here η_p is the plasma viscosity, and the fitting parameters k_0, k_∞, and γ_c vary with H according to the experimental observations reported in [32, 114, 133]. For small shear rates ($\gamma \to 0$), equation 3.3 reduces to $\eta = \eta_p(1 - k_0H/2)^{-2}$. At low Hct ($H \to 0$), this equation yields the Einstein model for a dilute suspension of rigid spheres, $\eta = \eta_p(1 - k_0H)$ with $k_0 = 2.5$. Further, at low hematocrits, (less than 20 %), the parameters k_0, k_∞, and γ_c all become constant [133, 32]. Recalling that shear stress $\tau = \eta\gamma$, equation 3.3 can be rewritten as [144]

$$\frac{\tau}{\gamma} = (\sqrt{\eta_\infty} + \frac{\sqrt{\tau_0}}{\sqrt{\lambda} + \sqrt{\gamma}})^2 \tag{3.4}$$

where

$$\tau_0 = \eta_p \frac{\gamma_c H(k_0 - k_\infty)}{2(1 - k_\infty H/2)^4} \tag{3.5}$$

$$\eta_\infty = \eta_p(1 - k_\infty H/2)^{-2} \tag{3.6}$$

$$\lambda = \gamma_c(\frac{2 - k_0H}{2 - k_\infty H})^2 \tag{3.7}$$

The radial distribution of the shear stress $\tau(\xi)$ in the non-Newtonian fluid, whose viscosity $\eta(\xi)$ varies with the normalized radius ξ in accordance with equation 3.3, satisfies the steady-state axisymmetric Cauchy equations of motion,

$$0 = -J + \frac{1}{R\xi}\frac{\partial(\tau\xi)}{\partial\xi}, \qquad 0 \leq \xi \leq 1 \tag{3.8}$$

The resulting blood velocity profiles $v(\xi)$ must be symmetric with respect to the arterioles center ($\xi = 0$), i.e., $dv/d\xi = 0$ at $\xi = 0$. Recalling the definition of the shear stress τ, this yields a boundary condition for equation 3.8, $\tau(0) = 0$. A solution of this boundary-value problem gives the distribution of shear stress across the arteriole,

$$\tau = JR\xi/2 \tag{3.9}$$

Combining equations 3.9 and 3.4 yields the shear rate distribution across the arteriole [144] (from $0 \leq \xi \leq 1$)

$$\gamma = \frac{JR}{4\eta_\infty}(\xi - \alpha(1+q)\sqrt{\xi} + (\sqrt{\xi} - \alpha)\sqrt{\xi - 2\alpha q\sqrt{\xi} + \alpha^2}) \qquad (3.10)$$

where

$$\alpha = \frac{\sqrt{\tau_0} + \sqrt{\eta_\infty \gamma}}{\tau_w} \qquad (3.11)$$

$$q = \frac{\sqrt{\tau_0} - \sqrt{\eta_\infty \gamma}}{\sqrt{\tau_0} + \sqrt{\eta_\infty \gamma}} \qquad (3.12)$$

and $\tau_w = JR/2$ is the shear stress at the arteriole wall $\xi = 1$.

To compute the blood velocity distribution $v(\xi)$, we recall the definition of the shear stress τ in equation 3.9 and enforce the no-slip boundary condition at the arteriole wall ($\xi = 1$),

$$\frac{v}{\xi} = \frac{JR\xi}{2\eta H(\xi)}; \qquad v(\xi = 1) = 0. \qquad (3.13)$$

The interdependence between the parameters entering the relationship $2\eta H(\xi)$ given by equations 3.1 - 3.3 introduces an additional constraint. Specifically, mass conservation of RBCs inside the arteriole imposes the following relationship between the localized (H) and systemic (H_d) hematoctrits [102, 182]:

$$\int_0^1 H(\xi)v(\xi)\xi d\xi = H_d \int_0^1 (\xi)v(\xi)\xi d\xi. \qquad (3.14)$$

For a given value of the systemic hematocrit H_d , we use the iterative procedure in [182] to compute the blood velocity distribution $v(\xi)$ from the boundary-values problem 3.13 subject to the integral constraint 3.14.

1. Guess a value of the core hematocrit H_c (e.g., by adopting a linear relationship between the systemic and core hematocrits).

2. Use equations 3.1 and 3.2 to compute the localized hematocrit $H(\xi)$.

3. Use equation 3.3 to compute the blood viscosity $2\eta H(\xi)$.

4. Solve the boundary-value problem 3.13 to compute the blood velocity distribution $v(\xi)$.

5. Use equation 3.14 to verify if the resulting velocity profile $v(\xi)$ yields H_d consistent with the given value of the systemic hematocrit (with prescribed tolerance ϵ). If yes, the simulation is completed. If not, set $H_c = H_c + \Delta$ (where Δ is a prescribed constant) and go back to step 2.

In the simulations reported below, we set $\epsilon = 10^{-6}$ and $\Delta = 10^{-4}$.

The resulting velocity profiles $v(\xi)$ are shown in Figure 3.2a for several values of the systemic hematocrit . These profiles are qualitatively similar to the observed velocity profiles [18, 109, 94] in that they are continuous across the arteriole. This is in contrast with models that treat blood as a two-phase liquid, e.g., [172], yielding velocity jumps at the interface between the RBC-rich core and the plasma layer. As H_d increases, the non-Newtonian nature of blood flow becomes more pronounced, with the velocity profiles becoming blunter. Figure 3.3 compares the velocity profile predicted with our model and the experimentally observed velocity profile for $R = 27.1\mu m$, $H_d = 0.335$, $J = 3726 dynes/cm^3$.

Higher H_d values imply higher WSS, as larger pressure gradients are required to drive the flow and hence. Figure 3.2b demonstrates the rapid increase of WSS with H_d. Figures 3.2c and 3.2d show the spatial variability of flow velocity and shear rate near the arteriole walls for different values of systemic hematocrit H_d. As H_d increases, both velocity and shear-rate profiles become steeper near the arteriole wall and blunter near the arteriole centerline. This phenomenon is a manifestation of the non-Newtonian behavior of blood that increases with H_d.

It is worthwhile emphasizing that the model presented above is valid for both steady (constant J) and quasi-steady (pulsating J) flows in small arterioles, for which the Womersley number is small. (The arterioles considered in this study have $R = 20\mu m$, resulting in the Womersley numbers on the order of 10^{-2}.) This is because this flow regime allows one to neglect the inertial term in the Navier-Stokes equations even if $J = J(t)$ [12].
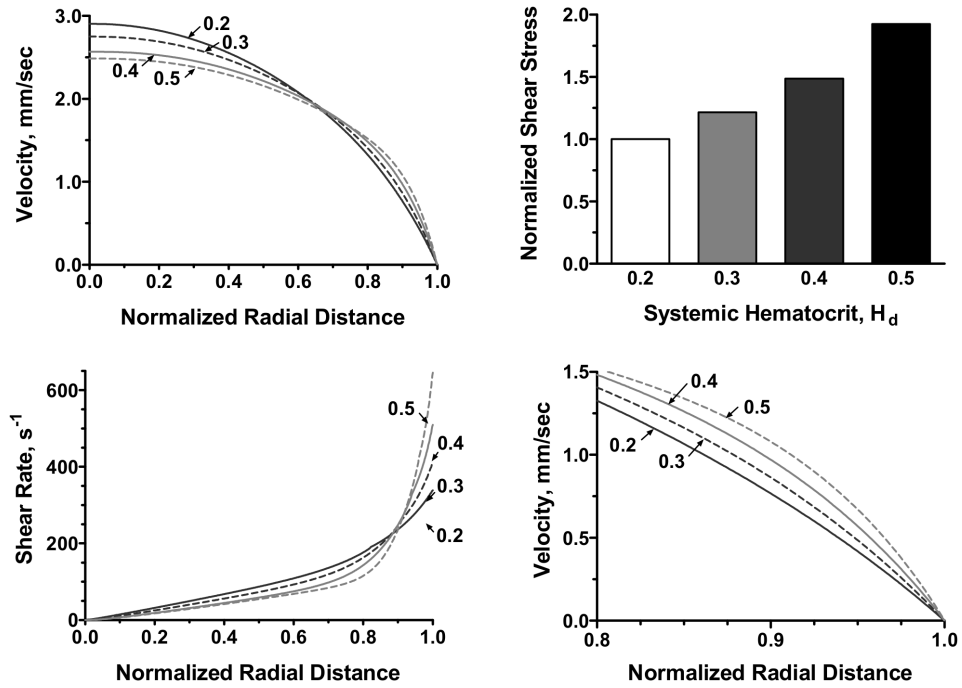
Figure 3.2: (clockwise from top left): a) Velocity profiles corresponding to the sigmoidal Hct profile (eq. 3.2), for fixed vessel radius $R = 27.1\mu m$ and several values of systemic Hct H_d and constant flow rate; b) Corresponding variation in WSS; c) Velocity profiles near the vessel wall; d) Variation of shear rate near the vessel wall.
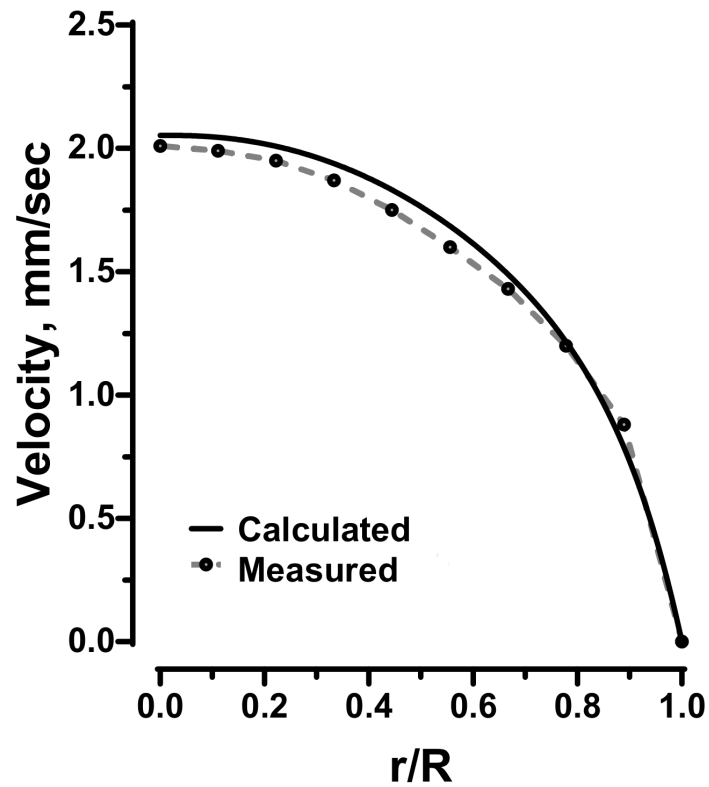
Figure 3.3: Experimentally determined velocity profile for human blood at $H_d = 33.5\%$ in a $54.2\mu m$ diameter glass tube at pressure gradient of 3736 dyn/cm^3, as reported in [109] (dotted line) compared with theoretically modeled velocity profile using the Quemada model (solid line) under same flow conditions.

3.6   Flow in presence of plasma expanders

We employed our mathematical model of blood flow to assess the effectiveness of plasma expanders (PEG-Alb, Dextran 70, and Dextran 500) by analyzing their impacts of WSS. Experimental data was used to parameterize the flow model as follows. First, we used the data presented in Figure 3.1 to parameterize the Quemada model for the mixtures of blood and plasma expanders. Second, we used data from [27] which measured how vessel radius and centerline velocity vary from baseline upon hemodilution with each plasma expander. For a prescribed vessel radius and centerline velocity at baseline we used this data to fix the vessel radius and centerline velocity associated with hemodilution using each of the three plasma expanders.

With these inputs, we applied our flow model to determine the pressure gradients needed to maintain the experimentally determined (centerline) flow velocities associated with each plasma expander. Using the calculated pressure gradients, we computed the shear-rate and velocity profiles that are shown in Figures 3.4 and 3.5, respectively. Finally, we used both the calculated value of pressure gradient and the experimentally determined variation of vessel radius to predict variation of WSS associated with each plasma expander (Figure 3.6). All the calculations were carried out for arterioles with two baseline diameters: 40 μm and 60 μm.

To elucidate the importance of shear thinning, Figures 3.4 and 3.5 also present the shear rates and velocities computed by treating blood as a Newtonian fluid, i.e., by relying on Poiseuilles law. Our non-Newtonian model predicts a sharp increase in shear rate near the arteriole wall (Figure 3.4), which implies that the reliance on Poiseuilles law would significantly underestimate WSS. This effect, and the underlying blunting of the velocity profiles (Figure 3.5), is more significant in a baseline 40 μm diameter arteriole than in a baseline 60 μm diameter arteriole, as smaller vessel have lower shear rates and hence more pronounced shear-thinning behavior. Both PEG-Alb and Dextran 500 lead to appreciable increases in WSS relative to Dextran 70.

Viscosity values measured at high shear rates (at which viscosity becomes independent of shear rate and rheological behavior becomes Newtonian) were assumed for calculation of the Poiseuille flows, with the same pressure gradients and vessel radii as
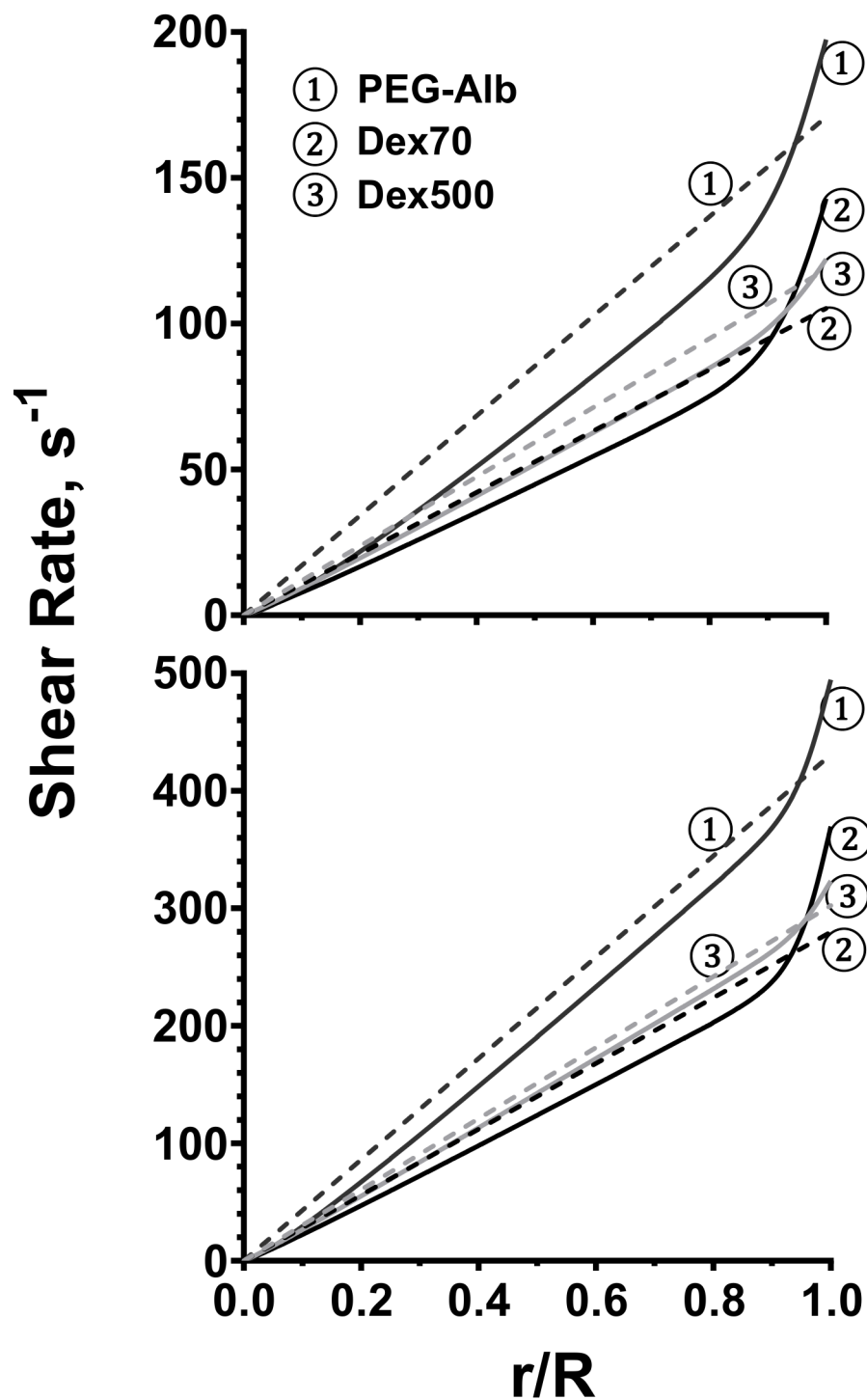
Figure 3.4: Radial variation of shear rate for the flow of blood diluted with the three plasma expanders used for a) Arteriole of 40 μm baseline diameter. b) Arteriole of 60 μm baseline diameter (solid lines). Corresponding velocity profiles for equivalent Poiseuille flows at the same pressure gradients are also shown (dashed lines).
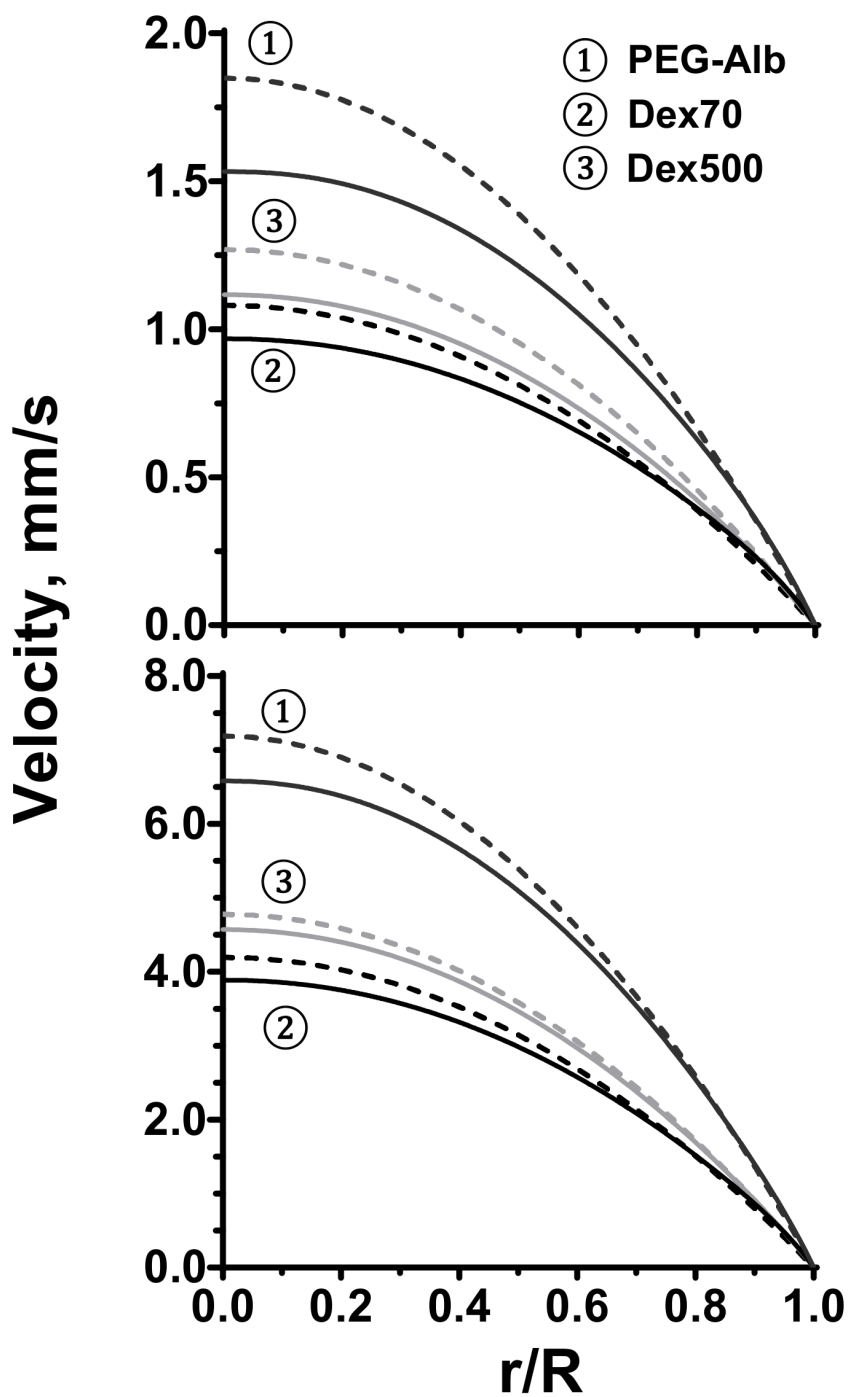
Figure 3.5: Velocity profiles for flow of blood diluted with the three plasma expanders in: a) Arteriole of baseline 40 μm diameter; b) Arteriole of baseline 60 μm diameter (solid lines). Corresponding velocity profiles for equivalent Poiseuille flows at the same pressure gradients are also shown (dashed lines).

the corresponding non-Newtonian flows.

Hemodilution with Dextran 500 and PEG-Alb increased vessel diameters and flow rates above the baseline. The pressure gradients required to produce the flow rates for each plasma expander (and vessel radius) were then calculated using equations 3.1 - 3.14.

Model results are under the assumption of steady flow, with the oscillatory component of the flow neglected. The resulting calculations for WSS are hence equivalent to a time-averaged value, with the average of the oscillatory component of flow equal to zero.

3.7 Measurement of perivascular NO

We used the experimental technique [192] to measure the concentration of nitric oxide (NO) in the vessel wall. The experimental procedure relies on carbon electrodes coated with Nafion to measure the current produced by the application of a +0.8 volts potential relative to a silver-silver chloride reference electrode. It was used to measure NO concentrations in arterioles and venules of the hamster window chamber model; detailed descriptions of the 3-step procedure used to study perivascular NO levels for HV and LV in extreme hemodilution can be found in [19]. The present study followed the same procedure, except the finial hemodilution step was performed using 4 % PEG-Alb.

In brief, the method consists in removing the cover glass of the window chamber after the third exchange, and superfusing the tissue with a physiological Krebs salt solution (33-34 Celcius). Perivascular measurements are made by penetrating the perivascular tissue with the micropipette so that the tip is close to the microvessel without visibly touching and deforming the wall [19]. The electrode current was measured with a potentiostat and electrometer (Keithley model 619C, Cleveland, OH).

3.8 Results of perivascular NO measurements

Six animals were entered into this study for the measurement of NO, and all animals tolerated the hemodilution protocol without visible signs of discomfort. Two an-
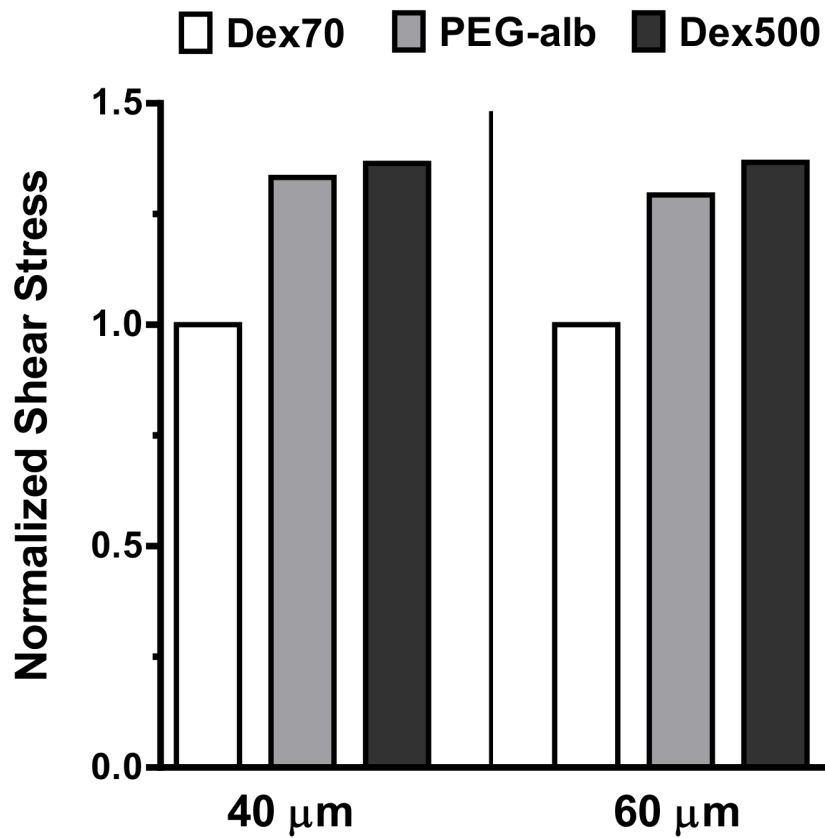
Figure 3.6: Increase in WSS values calculated for Dextran 500kDa and PEG-albumin plasma expanders relative to WSS calculated for Dextran 70kDa plasma expander: a) Arteriole of baseline 40 μm diameter. b) Arteriole of baseline 60 μm diameter. Values of WSS (in $dyne/cm^2$) calculated for a) Dextran 70: 2; Dextran 500: 2.73; PEG-Alb: 2.67 b) Dextran 70: 5.175; Dextran 500: 6.95; PEG-Alb: 6.68.

imals were used as controls to insure that the system calibration and animal preparation was the same as previous control measurements [191]. However, PEG-Alb perivascular NO levels have not been previously published.

Physiological conditions and the rheological properties of blood after level 3 exchange are presented in Table 2. For comparison, data on low viscosity hemodilution using Dextran 70, and high viscosity hemodilution using Dextran 500 from the previous study by Tsai et al. [190] is also included. NO measurements in all experiments were performed during a period of 1 - 2 hr after hemodilution.

Figure 3.7 presents the principal finding from these measurements: increased perfusion found in extreme hemodilution using PEG-Alb is associated with increased arteriolar and venular perivascular NO. These NO concentrations were significantly greater than in control and when extreme hemodilution was performed using Dextran 70. NO concentrations were the same as those found using Dextran 500.

Table 3.2: Hemodilution with low viscosity Dextran 70, high viscosity Dextran 500 and PEG-Alb.

	Control (*)	Dextran 70 (*)	Dextran 500 (**)	PEG-Alb (*)
Hct (%)	49.3 ± 1.8	11.1 ± 0.9	11.0 ± 0.6	11.2 ± 0.7
MAP, mmHg	103.6 ± 6	64 ± 8	87 ± 6	79 ± 7
Heart rate, bpm	414 ± 35	418 ± 41	453 ± 38	460 ± 31
Cardiac Output, ml/min	17.8 ± 1.6	14.2 ± 1.9	19.6 ± 3.5	24.2 ± 1.6
Plasma Viscosity, cP	1.2 ± 0.1	1.4 ± 0.2	2.2 ± 0.2	1.3 ± 0.1
Blood Viscosity, cP	4.1 ± 0.4	2.1 ± 0.2	2.8 ± 0.2	1.8 ± 0.1

Data is from (*): [26]; (**): [27]

3.9 Effect of NO synthase inhibition

In order to further support the hypothesis that enhanced NO production is the primary cause for the observed increase of perfusion, we performed hemodilution with PEG-Alb followed by treatment with the NO synthase inhibitor L-NAME. This allowed us to determine the extent of the dependence of supra-perfusion on enhanced NO production. In these experiments, it was not possible to apply L-NAME after extreme hemodilution to 11 % since the combination of significant decrease in intrinsic oxygen
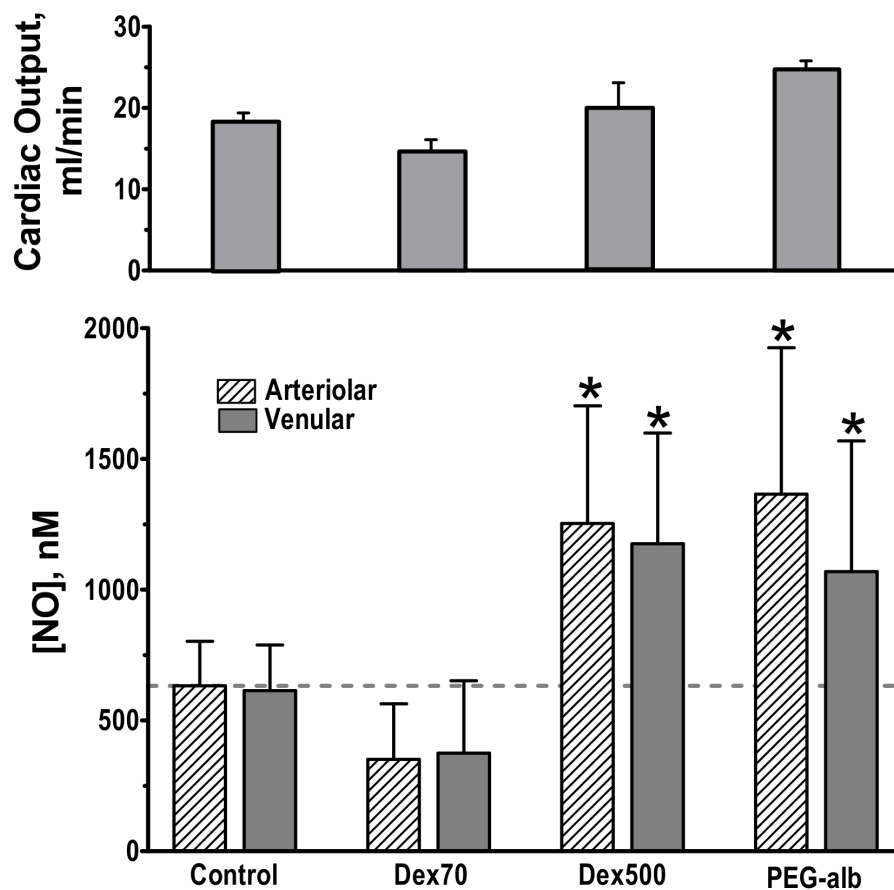
Figure 3.7: Perivascular microelectrode NO measurements during hemodilution at 11 % Hct using a 3 steps protocol that starts with hemodilution with 6 % Dextran 70 kDa, resulting in a final concentration of 1 % by weight of either Dextran 70, Dextran 500 or PEG-Alb at the time of measurement. Comparison with cardiac output measured at the same time point by thermodilution. All measurements are statistically different from baseline, p ¡ 0.05.

carrying capacity due to hemodilution and perfusion due to L-NAME administration caused all animals to succumb. Therefore we hemodiluted the animals to 35 % Hct with Dextran 70 kDa and then carried a second hemodilution to Hct 18
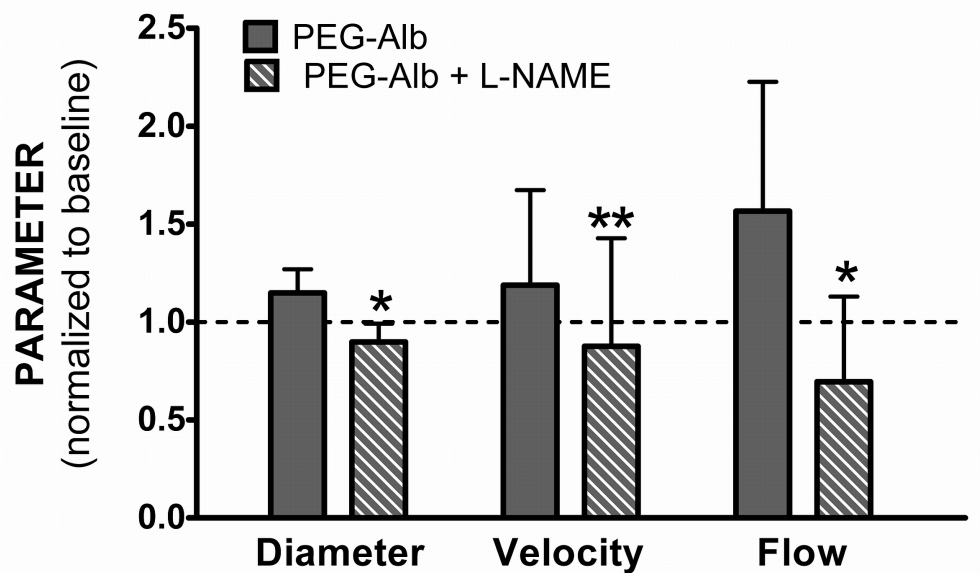
Figure 3.8: Vessel diameter, centerline velocity, and blood flow rate in arterioles of the hamster widow model. Animals were first hemodiluted with 6 % Dex70 to 35 % Hct and then subsequently to 18 % Hct using 4 % PEG-Alb (n= 5, 25 arterioles, 4060 μm diameter) and finally treated with N-nitro-L-arginine methyl ester (L-NAME). Data were normalized relative to baseline. Significance of differences between untreated and L-NAME-treated PEG-Alb hemodilution: $*P < 0.001$ and $**P < 0.05$.

3.10   Discussion

This study shows that the supra-perfusion condition established during extreme hemodilution with PEG-Alb is directly associated with increased WSS and related increased NO vessel wall concentration. The increase in WSS is shown by mathematical modeling to be a consequence of the shear thinning properties that PEG-Alb confers to Dextran 70 diluted blood. The significance of these findings is that extreme hemodilution with PEG-Alb results in a greater than 40 % reduction of peripheral vascular

resistance and a corresponding increase in blood flow and perfusion, a condition that we term supra-perfusion (Table 4.2 and Figure 3.7).

The increase in WSS increases NO production by the endothelium as evidenced by its direct measurement in the vessel wall with microelectrodes. In principle, increased WSS requires increased plasma viscosity and/or flow, of the fluid component directly in contact with the endothelium. This is the case of high viscosity plasma expanders such as Dextran 500, whose rheology is nearly Newtonian at the low value of Hct down to which hemodilution is performed. By contrast, blood diluted with PEG-Alb is strongly shear thinning, even at 11 % Hct. This effect redistributes shear rate energy expenditure from the bulk of the flow to the periphery and also increases the apparent viscosity of the fluid, accounting for the increase in WSS.

The increase of NO production with shear stress is consistent with previous experimental studies of endothelial response to WSS conducted in flow chambers [118, 122]. While these experiments do not exactly reproduce in-vivo conditions due to the absence of pulsatility, they show that NO production increases with increasing WSS in steady (and slowly varying) flow regimes. Flow in arterioles is pulsatile [12] in synchrony with the heart, and has a random variability in the region of the cell free plasma layer due to the continuous realignment of the RBCs that limit the cell free plasma layer on the blood side [9] and the spatial variability of the endothelial surface layer [138].

The increase of WSS in microvessels associated with PEG-Alb is a property of laminar flow at low shear rates; in the heart, where most fluid volumes have significant velocity gradients (and high shear rates), the viscosity of blood mixed with PEG-Alb is low. Conversely, if blood is diluted with a high viscosity plasma expander, the fluid in the heart has the corresponding higher viscosity. This leads to a different mechanical expenditure by the heart in pumping blood diluted with these different plasma expanders.

Table 4.2 and Figure 3.7 show that these effects are important, with perivascular NO concentrations being higher with dilution with PEG-Alb and Dextran 500 than with Dextran 70 or baseline conditions. Simply lowering blood viscosity by hemodilution with a conventional colloidal plasma expander such as Dextran 70 significantly lowers blood viscosity and blood pressure, but not peripheral vascular resistance. This occurs because microcirculatory WSS is not sufficient to sustain NO production and maintain

normal vasodilation. Increasing plasma viscosity with a Newtonian fluid pressurizes the circulation, and improves flow and WSS, lowering peripheral vascular resistance; however the effect on peripheral vascular resistance is partially negated by the increased blood viscosity throughout the circulation. PEG-Alb increases viscosity in the blood vessel core, and lowers blood viscosity in the high shear rate regions of the circulation, synergistically increasing perfusion. In accounting for this synergistic mechanism by which PEG-albumin increases perfusion, we ruled out hypoxic vasodilation by RBCs as a contributing factor since the hemodilution achieved in these experiments corresponds to pO2 levels in the range of 23.5 - 48.0 mmHg (vs. 45.0 - 58.8 mmHg for normal baseline) [192] which is above the range of pO2 levels where the phenomenon of RBC facilitated vasodilation is expected to occur [49].

Our model of blood flow in an arteriole treated blood as a non-Newtonian fluid with the Quemada constitutive model. The model yields velocity profiles and radial variations of shear rate that are in qualitative agreement with the experimental data reported in [109, 18, 188, 94]. Since our model is suitable for a wide range of hematocrit, it can be used to analyze data from blood flow experiments in vivo and in vitro.

The shear thinning effect is expected to be due to PEG-Alb inducing an increase in the interaction between RBCs, although by a mechanism different to the one causing aggregation by Dextran 500 kDa. Aggregation due to Dextran 500 kDa causes large RBC aggregates at higher Hcts but not in extreme hemodilution. Aggregation due to the presence of PEG-proteins was not evident in our experiments, even at higher Hcts. The increase in WSS evidenced by our modeling study of the effect of shear thinning is primarily due to the increase in shear rate in the proximity of the vessel wall due to a combination of factors including the increased flow, the blunting of the velocity profile and the small increase in plasma viscosity (from 1.2 to 1.3 cP). The potential beneficial effect of increased blood aggregability has been reviewed and discussed in [12].

This study shows that treating blood as a non-Newtonian shear-thinning fluid predicts significantly higher shear rates (and hence shear stresses) at the vessel walls relative to shear rate estimates obtained from Poiseuilles law. Hence, previous studies of plasma expanders [26, 27, 192] probably underestimated the relative increase of WSS with the introduction of Dextran 500 and PEG-Alb plasma expanders.

3.11 Alternative mechanisms for supra-perfusion

A host of other mechanisms may play a role in enhancing perfusion.

Extreme hemodilution and changes in blood viscosity significantly change the distribution of pressure in the circulation, interacting with the mechanical properties of blood vessels and the Bayliss effect. In previous studies we modeled the effects of a 10

Increased NO bioavailability is a factor in hemodilution, because it increases the cell free layer (CFL) width. Our analytically study [182, 181] shows that in hemodilution the effect due to WSS dominates the effect of NO-scavenging by RBC hemoglobin. Both blood viscosity and RBC aggregability influence the CFL width. Since RBC aggregability causes shear thinning, it is likely that PEG-Alb increases NO bioavailability relative to colloids that induce low or no aggregability.

Acidosis due to massive dilution with sodium chloride causes dilatation and could be a factor, however this was not observed in our studies as shown in Table 2.

In order to verify that increased perfusion associated with PEG-Alb was due to increased NO production we carried out hemodilution with PEG-Alb, followed by treatment with L-NAME. The introduction of L-NAME (which serves to inhibit NO production) effectively eliminated improvements in perfusion achieved with the use of PEG-Alb as a plasma expander. This helps to justify our claim that the introduction of PEG-Alb induces higher WSS in the microcirculation, thereby stimulating NO production and increasing perfusion.

In summary, Dextran 70, Dextran 500 and PEG-Alb mixed with blood in conditions of extreme hemodilution exhibit the behavior of non-Newtonian shear thinning fluids. Previous hemodilution experiments using the plasma expanders studied [26, 27, 192] indicated that Dextran 500 and PEG-Alb increased blood flow and diameter to a significantly greater extent than Dextran 70. It was hypothesized that both Dextran 500 and PEG-Alb used as plasma expanders improved cardiac performance by elevating WSS, thereby increasing NO bioavailability and inducing vasodilation. We tested this hypothesis by developing a mathematical to calculate WSS in arterioles under hemodilution with each plasma expander. Results (Figure 3.6) show that both Dextran 500 and PEG-Alb significantly increase WSS. This leads to significant increases in perivascular NO

concentration relative to Dextran 70 hemodilution and baseline conditions.

The significance of these findings is that they explain why PEG-Alb hemodilution produces a state of supra-perfusion. This occurs because blood is diluted, lowering blood viscosity in high shear rate zones of the circulation, like the heart and major vessels; while apparent viscosity and WSS increase in the microcirculation promoting the production of NO by the endothelium and vasodilatation. An extreme case of this effect is the conversion of the fluid in the blood vessel core into a solid piston (maximum viscosity at zero shear rate), with a thin peripheral lubricating layer between the piston and cylinder. This synergy of such mechanisms, including a possible contribution from the Bayliss mechanism not explored in the present study, should also be operational in the heart muscle, allowing the heart to maintain blood pressure and to increase cardiac output, leading to the beneficial effect found in using PEG-Alb plasma expander.

The clinical significance of our findings is expressed by the recent meta-analysis [67] of the hemodynamic factors that determine survival of high-risk surgical patients. This study found that "for most high-risk patients, the main cause of death is more often related to tissue perfusion dysfunction than to a cardiac problem" and concluded that in "high-risk surgical patients with no evident organ dysfunction before surgery, maintaining tissue perfusion preoperatively according to a specific protocol reduces postoperative mortality and morbidity".

3.12   Acknowledgements

This Chapter is a reprint of the material as it appeared in:

K. Sriram, B. Y. Salazar Vazquez, A. G. Tsai, P. Cabrales, M. Intaglietta, and D. M. Tartakovsky. Autoregulation and mechanotransduction control the arteriolar response to small changes in hematocrit. Am. J. Physiol. Heart Circ. Physiol., 303(9):H1096-1106, 2012. The dissertation author was the primary investigator and author on this paper.

Chapter 4

Calculating Velocity Profiles and Shear Stress in Arterioles

4.1 Introduction

Velocity profiles of blood flowing in glass tubes [109, 59, 4] and in vivo [18, 94, 188] are observed to be blunted, rather than the parabolic velocity profiles characteristic of Newtonian fluids. Both the CFL [90, 109] and non-Newtonian behavior of blood [114, 133, 157, 180] in the microcirculation have been used to explain the experimentally observed bluntness of blood velocity profiles in narrow glass tubes [109, 59, 4] and in-vivo micro-vessels [109, 18, 94, 188].

Blunting of the parabolic (Newtonian) velocity profiles observed in microvessels is indicative of changes in blood viscosity within the blood vessel cross section. This redistribution affects the overall rate of energy dissipation by the flow and the distribution of shear stress within the profile. Of particular physiological significance is the shear stress developed at the microvessel vessel wall that modulates the production of shear stress dependent materials by the endothelium, a significant effect due to the large endothelialized surface of the microcirculation [145, 95, 12]. The bluntness of blood velocity profiles also has significant implications on indirect measurements of wall shear stress (WSS), which are typically inferred from direct measurements of centerline velocity and vessel radius by invoking the Poiseuille law [160, 25, 87]. The mismatch between the ex-

perimentally observed blunt velocity profiles and their parabolic counterparts predicted by the Poiseuille law introduces interpretive errors in WSS measurement [87, 160].

A typical CFL thickness is on the order of 1 μm [90, 149, 159, 186]. It is relatively insensitive to vessel radius, but decreases significantly with hematocrit [56, 164, 186]. While plasma in the CFL can be treated as a Newtonian fluid, the RBC-rich core displays non-Newtonian shear-thinning properties. In this study, we assume a general functional dependence of CFL thickness on hematocrit and then calculate velocity profiles of blood flow through a tube, comprising two discrete fluid layers: the non-Newtonian RBC core and the CFL (which is assumed Newtonian).

Experimental work on blood rheology has demonstrated the dependence of blood viscosity on shear rate and hematocrit, showing that the relationship between shear stress and shear rate for blood is non-linear (and non-Newtonian), with shear thinning properties [32, 114, 133] which are enhanced by increasing hematocrit. This shear-thinning rheology of blood in the RBC core was mathematically represented in our flow model via the Quemada rheological model. The Quemada model is a three-parameter constitutive rheological model that accurately describes shear thinning blood rheology over a wide range of shear rates and hematocrit [114, 133, 157]. Due to this robustness, the Quemada model is superior to other blood rheological models of comparable complexity [114] and was hence utilized in our flow model.

Previous mathematical models of blood flow in microvessels have typically treated both fluid layers (the CFL and RBC core) as Newtonian fluids, with the viscosity of the RBC core being larger than the viscosity of the CFL [130, 172, 179]. Our model builds upon these previous studies; we compare results for our non-Newtonian model with the 2-layer Newtonian model and demonstrate that significant differences between the two models exist. We demonstrate that our model is a significant improvement over previous Newtonian models, more accurately predicting CFL thickness, velocity profiles and apparent viscosities.

We then leverage our flow model to develop a general method for correcting experimental estimation of WSS. Typically, WSS in a blood vessel is estimated in experimental studies by measuring the centerline velocity and the vessel radius; with these values the WSS is then calculated using the Poiseuille law [25, 87, 160]. The problem with

this approach is that blood flow in microvessels does not follow the Poiseuille law (due to the inhomogeneous and non-Newtonian behaviors discussed above). This introduces errors in the measurement of WSS [87, 160].

These errors may be avoided by direct measurement of velocity profiles, using methods such as in [109]. This allows precise estimation of shear rate at the vessel wall; for a known plasma viscosity, WSS can then be calculated once wall shear rate is known. The difficulty with this alternative is that direct measurement of velocity profiles is a difficult and complicated task; repeatedly measuring velocity profiles every time WSS estimates are needed is relatively impractical (and expensive) with current technology and experimental techniques [87].

In this study, we compute the magnitude of these WSS estimation errors arising from the use of the Poiseuille law and demonstrate that these errors are significant. We propose two methods to eliminate these errors: an iterative numerical algorithm which leverages our flow model, and the use of a simple correction factor that can be incorporated into the Poiseuille law. Given a rheological model of the RBC-rich core, both approaches allow one to infer WSS from measurements of vessel radius, centerline velocity and discharge hematocrit.

4.2   Mathematical model of blood flow in arterioles

Symbols Used

R, r	Vessel radius and radial coordinate
μ_p	Plasma viscosity
γ_c, k_0 and k_∞	Parameters in the Quemada rheological model
μ, μ_{eff}, μ_{rel}	Medium, Effective medium and Relative medium viscosity
τ, τ_w	Shear stress and Wall shear stress (WSS)
δ	CFL thickness
Q	Flow rate of blood in blood vessel
γ	Shear rate
H, H_c, H_d, H_t	Localized, core, discharge and tube hematocrit
J	Pressure gradient
v_z	Axial velocity
$v_{\max}$	Centerline (maximum) velocity
ϕ	WSS correction factor

We consider steady-state blood flow in an arteriole of fixed radius R. The flow is
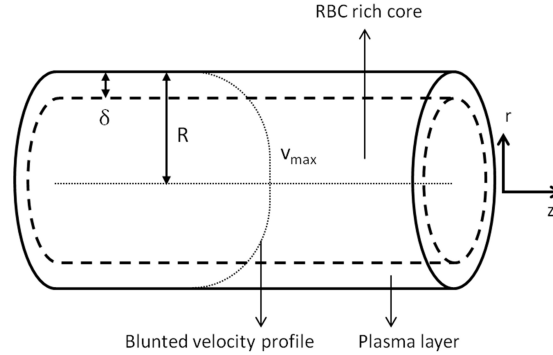
Figure 4.1: Cell-free layer (CFL) and red-blood-cell (RBC) rich core in an arteriole. The CFL is occupied by plasma, a Newtonian fluid whose viscosity is lower than that of the non-Newtonian fluid comprising the RBC-rich core.

driven by an externally imposed pressure gradient J, with no-slip boundary conditions prescribed at the (non-deformable) vessel walls. Blood is treated as a two-layer inhomogeneous fluid: an RBC-rich core region near the vessel centerline [172, 179] occupies the cylinder of radius $(R - \delta)$ and a CFL of thickness δ occupies the rest of the vessel (Figure 4.1). Plasma in the CFL is modeled as a Newtonian fluid with a constant viscosity μ_p, independent of both hematocrit H and shear rate γ. Hematocrit distribution in the RBC-rich core is assumed to be uniform. The Quemada rheological model [114, 133, 157] is used to describe the non-Newtonian, shear-thinning behavior of the RBC-rich core.

The Quemada constitutive law postulates a nonlinear relationship between shear stress τ and shear rate γ in the RBC-rich core,

$$\tau = \frac{\gamma \mu_p}{(1 - k H_c/2)^2}, \qquad k = \frac{k_0 + k_\infty \sqrt{\gamma/\gamma_c}}{1 + \sqrt{\gamma/\gamma_c}}. \tag{4.1}$$

The model parameters γ_c, k_0 and k_∞ vary with core hematocrit H_c (the value of hematocrit H in the RBC-rich core) [32, 133]. We fit the parameter data reported in [133] with second-degree polynomials in H_c. Figure 4.2 exhibits both the data and the fitted curves (with the goodness-of-the-fit $\mathcal{R}^2$ exceeding 0.99 for all three curves). The Quemada model (4.1) reduces to a linear (Newtonian) relationship between τ and γ when either H_c is small or γ is large.

The normalized (dimensionless) effective viscosity μ_{eff} of blood is defined from
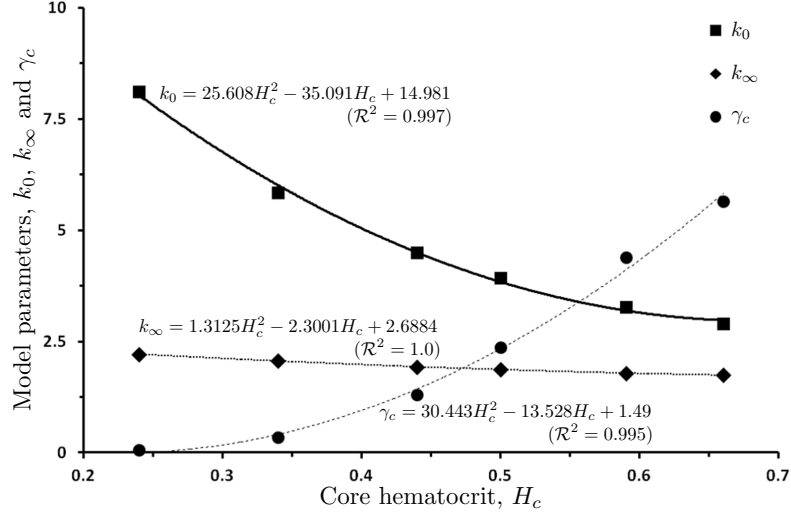
Figure 4.2: The data reported in [133] show the dependence of the Quemada model parameters γ_c, k_0 and k_∞ on the core hematocrit H_c. These data are fitted with second-degree polynomials in H_c.

Eq (4.1) as

$$\mu_{\text{eff}} = \frac{\tau}{\gamma \mu_p} = \frac{1}{(1 - kH_c/2)^2}. \tag{4.2}$$

According to this expression, the normalized effective viscosity μ_{eff} decreases with the shear rate γ and increases with the core hematocrit H_c increases (Figure 4.3). At large values of γ (above 200 s^{-1}), the viscosity is approximately constant and the fluid is essentially Newtonian.

Regardless of the fluid properties, the Cauchy equations of motion for steady (or pseudo-steady for low Womersley numbers), axisymmetric laminar flow have the form

$$0 = -J + \frac{1}{r}\frac{\partial}{\partial r}(r\tau). \tag{4.3}$$

Integrating this equation across the RBC-rich core (from 0 to $R-\delta$) and across the CFL (from $R-\delta$ to R) yields respectively

$$\tau(r) = \frac{Jr}{2} + \frac{C_1}{r}, \qquad 0 \leq r \leq R - \delta \tag{4.4}$$

and

$$\tau(r) = \frac{Jr}{2} + \frac{C_2}{r}, \qquad R - \delta \leq r \leq R \tag{4.5}$$
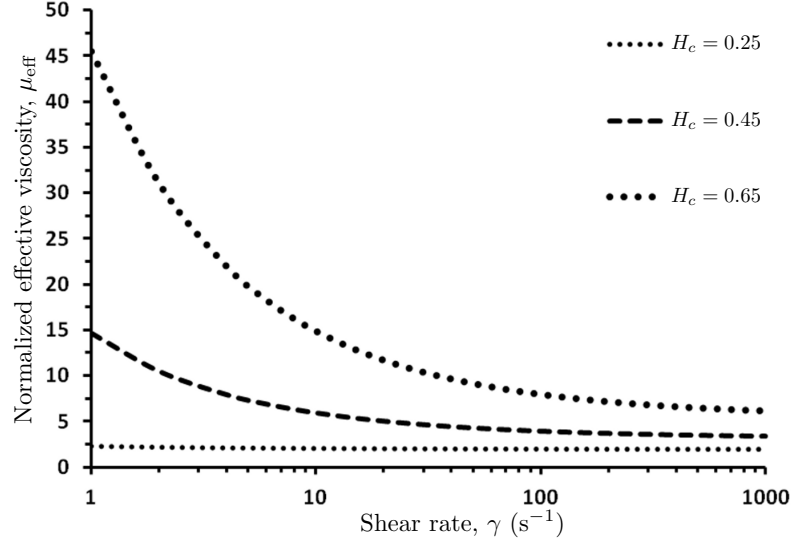
Figure 4.3: Variation of normalized (dimensionless) effective viscosity $\mu_{\text{eff}} = (1 - kH_c/2)^{-2}$ with shear rate γ and core hematocrit H_c.

where C_1 and C_2 are constants of integration. Since the shear stress $\tau(r)$ must remain finite throughout the blood vessel, including its centerline $r = 0$, we set $C_1 = 0$. The continuity of the shear stress at the interface between the two fluids (at $r = R - \delta$) requires $C_2 = 0$. Therefore, the shear stress $\tau(r)$ is given by

$$\tau(r) = \frac{Jr}{2}, \qquad 0 \le r \le R \tag{4.6}$$

throughout the blood vessel ($0 \le r \le R$).

Combining Eqs (4.6) and (4.1) yields an implicit expression for the radial distribution of shear rate $\gamma(r)$ within the RBC-rich core,

$$\gamma = \frac{Jr}{2\mu_p} \left(1 - \frac{H_c}{2} \frac{k_0 + k_{\text{inf}} \sqrt{\gamma/\gamma_c}}{1 + \sqrt{\gamma/\gamma_c}} \right)^2, \qquad 0 \le r \le R - \delta. \tag{4.7}$$

Since the CFL is occupied by plasma (a Newtonian fluid with viscosity μ_p), $\tau = \mu_p \gamma$ for $R - \delta \le r \le R$ and Eq (4.6) yields

$$\gamma = \frac{Jr}{2\mu_p}, \qquad R - \delta \le r \le R. \tag{4.8}$$

Equations (4.7) and (4.8) are coupled by the continuity of flow velocity at the interface $r = R - \delta$ separating the RBC-rich core and the CFL,

$$v_z^+ = v_z^- \tag{4.9}$$

where $v_z(r)$ is the flow velocity, and the superscripts $+$ and $-$ indicate the core and plasma velocities on either side of the interface, respectively. The flow velocity is related to the corresponding shear rate by $\gamma = \mathrm{d}v_z/\mathrm{d}r$. At the vessel wall $(r = R)$ we impose a no-slip boundary condition, $v_z(R) = 0$.

Given a value of the CFL thickness δ, both the shear rate $\gamma(r)$ and the flow velocity $v_z(r)$ are calculated by solving Eqs (4.7)–(4.9). The data reported in [56, 164] suggest that δ is relatively insensitive to the blood vessels radius R, but decreases appreciably with the discharge hematocrit H_d. The latter is related to the core hematocrit H_c by mass conservation [179],

$$H_c \int_0^{R-\delta} v_z(r)r\mathrm{d}r = H_d \int_0^R v_z(r)r\mathrm{d}r. \tag{4.10}$$

While one can choose any functional relation between δ and H_d, for the sake of concreteness we adopt a polynomial relationship

$$\delta = a_2 H_d^2 + a_1 H_d + a_0. \tag{4.11}$$

The parameters a_0, a_1 and a_2 are determined by fitting our model predictions to the measurements of apparent viscosity [151]. An initial guess for δ ($a_2 = 0$, $a_1 = 0$ and $a_0 = 1$ μm, which gives $\delta = 1$ μm) is refined by using the procedure outlined in Section 4.4.

4.3 Numerical algorithm for calculating velocity profiles

For given values of the discharge hematocrit H_d and the pressure gradient J, we use the following algorithm to compute the shear rate $\gamma(r)$ and the flow velocity $v_z(r)$.

1. Make an initial guess for H_c. (In the simulation reported below, the linear relationship $H_c = 0.9797 H_d + 0.0404$ [179] is used as an initial guess.)

2. Calculate the value of δ by using Eq (4.11).

3. Compute the shear rate $\gamma(r)$ in the RBC rich core and the CFL by using Eqs (4.7) and (4.8), respectively.

4. Compute the flow velocity $v_z(r) = \int_0^r \gamma(r')\mathrm{d}r'$.

5. Refine the previous guess for H_c by using Eq (C.4).

6. Repeat steps 3–5 until the absolute difference between the values of H_c obtained from two sequential iterations is smaller than prescribed tolerance ε (in the simulations reported below we set $\varepsilon = 10^{-6}$).

4.4 Model calibration

Pries et al. [151] compiled a number of measurements of human blood viscosity conducted in tubes of various radii R for several values of discharge hematocrit H_d. We use these data to calibrate our model, i.e., to determine the values of parameters a_0, a_1 and a_2 in Eq (4.11). That is accomplished in three steps as follows.

The first step is to evaluate the relative (dimensionless) apparent viscosity μ_{rel} that is defined as [151]

$$\mu_{\text{rel}} = \frac{\pi J R^4}{8 Q \mu_p}. \tag{4.12}$$

This quantity is routinely inferred from experiments by measuring Q and invoking the Poiseuille law. Instead, for a given value of the CFL thickness δ, we compute Q from the flow velocity v_z determined in Section 4.7.1 as

$$Q = 2\pi \int_0^R v_z(r) r \mathrm{d}r. \tag{4.13}$$

This calculation of Q is then used in Eq (4.12) to obtain the value of μ_{rel} associated with an assumed value of δ. Figure 4.4 exhibits the resulting dimensionless apparent viscosity μ_{rel} as a function of vessel radius R for discharge hematocrit $H_d = 0.45$ and several values of the CFL thickness δ.

The second step is to compare the relative apparent viscosity curves $\mu_{\text{rel}} = \mu_{\text{rel}}(R)$ in Figure 4.4 with their counterparts predicted by the data-fitted curve of Pries et al. [151], $\mu_{\text{Pr}} = \mu_{\text{Pr}}(R)$. The latter is given by

$$\mu_{\text{Pr}} = 1 + (\mu_{\text{Pr},0.45} - 1)\frac{(1 - H_d)^\alpha - 1}{(1 - 0.45)^\alpha - 1}, \tag{4.14a}$$

where $\mu_{\text{Pr},0.45}$ is the dimensionless apparent viscosity at reference discharge hematocrit $H_d = 0.45$ fitted with a curve

$$\mu_{\text{Pr},0.45} = 220\, e^{-1.3(2R)} + 3.2 - 2.44\, e^{-0.06(2R)^{0.645}}, \tag{4.14b}$$
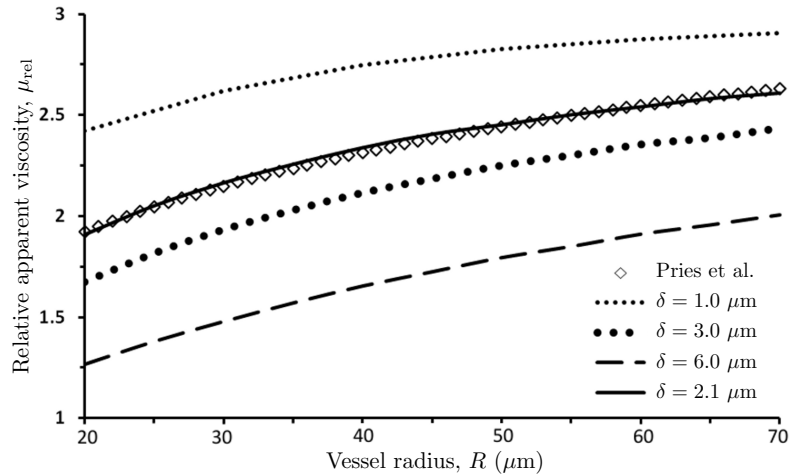
Figure 4.4: Dependence of relative apparent viscosity μ_{rel} on vessel radius R, for discharge hematocrit $H_d = 0.45$ and several values of the CFL thickness δ. Also shown is the dimensionless apparent viscosity obtained with the data-fitted curve (4.14) of Pries et al. [151].

and

$$\alpha = (0.8 + e^{-0.075(2R)}) \left[-1 + \frac{1}{1 + 10^{-11}(2R)^{12}} \right] + \frac{1}{1 + 10^{-11}(2R)^{12}}. \tag{4.14c}$$

In the relations above, R is reported in μm and α is dimensionless. The value of the CFL thickness δ that provides the best agreement between the two approaches is selected. For discharge hematocrit $H_d = 0.45$ used in Figure 4.4 this value is $\delta = 2.1$ μm. The fact that agreement between our model (Steps 1 and 2) and the Pries et al. [151] curves persists over a wide range of vessel radii R serves to validate our assumption that the CFL thickness δ is a function of discharge hematocrit H_d alone.

The final step consists of repeating the above procedure for multiple values of discharge hematocrit H_d, tabulating the δ vs. H_d values, and fitting the second-degree polynomial (4.11) to the resulting dataset. This step results in

$$\delta = -2.265H_d^2 - 1.4377H_d + 3.2131. \tag{4.15}$$

where values of δ are in μm. The use of the parameterized constitutive law (4.15) in our model yields predictions of apparent viscosity $\mu_{\text{rel}}(R)$ that are in close agreement

with their counterparts based on the Pries et al. [151] calculations over a physiologically relevant range of discharge hematocrit H_d and micro-vessel radii R (Figure 4.5).
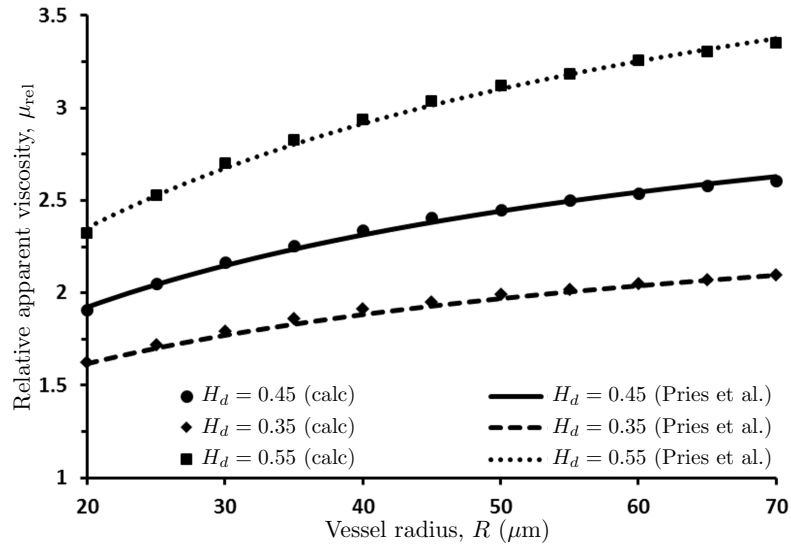
Figure 4.5: Relative apparent viscosity $\mu_{\rm rel}$ calculated with our model and the data-fitted curve of Pries et al. [151] over physiologically relevant ranges of micro-vessel radii R and discharge hematocrit H_d.

We used the data reported in [151] for blood vessels of radius $R \geq 20$ μm to calibrate the constitutive law $\delta = \delta(H_d)$ in Equation (4.15). We chose $R = 20$ μm as the lower range of the vessel radius because a continuum description of blood flow in smaller vessels might not be reliable [12] due to the finite diameter of RBCs (around 6 μm for human RBCs). However, the smallest radius below which continuum models of blood flow become invalid is still in dispute; for example, the limit of $R = 10$ μm was suggested in [172]. Figure 4.6 shows the predictions of the relative effective viscosity $\mu_{\rm del}$ over an expanded range of the vessel radius, starting with $R = 10$ μm. Since the predictions of our model and those due to Pries et al. [151] begin to diverge at about $R = 10$ μm, we suggest this value as the minimum vessel diameter at which our model may be applicable.
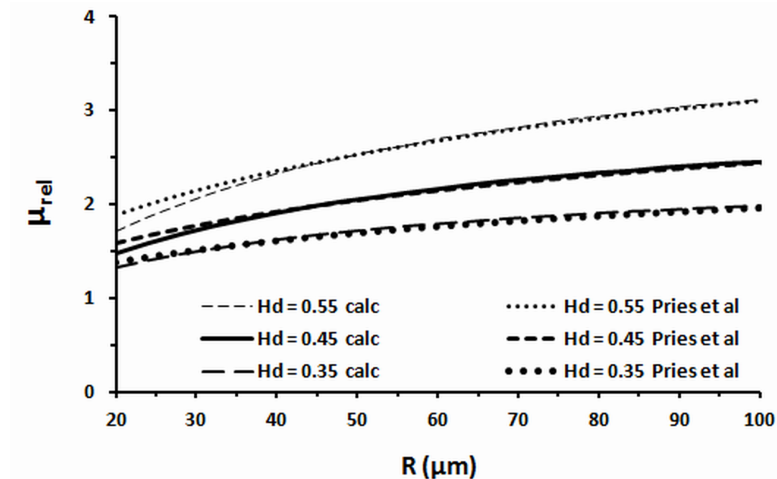
Figure 4.6: Relative apparent viscosity μ_{rel} calculated with our model and the data-fitted curve of Pries et al. [151] over physiologically relevant ranges of micro-vessel radii R and discharge hematocrit H_d.

4.5 Model validation

To validate our model, we compare its predictions of the CFL width, blood velocity profiles, and tube hematocrit (defined below) with their experimentally observed counterparts. These comparisons are carried out on the experimental data that were not used to parameterize our model.

4.5.1 CFL thickness

The values of CFL thickness δ predicted with the constitutive law (4.15) fall within a generally accepted range of around 2 to 3 μm [90, 149, 159, 186]. Figure 4.7 provides a further confirmation of the ability of our model to predict the CFL thickness for a wide range of micro-vessel radii. It compares the dependence of the relative CFL thickness δ/R on vessel radius R predicted with our model and observed in the experiments [149, 159, 186], for discharge hematocrit $H_d = 0.45$. Our model qualitatively captures the observed decrease of the CFL thickness δ with vessel radius R, underestimating the observed CFL thickness by 13% for $R = 15$ μm, 20% for $R = 30$ μm and 25% for $R = 47$ μm. This level of agreement is significantly better than that achieved

with the earlier models [56, 172, 179].
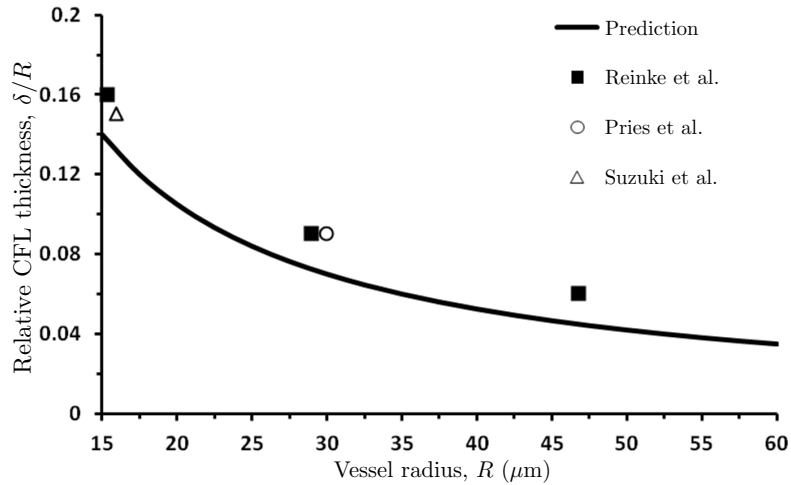
Figure 4.7: Predicted and experimentally observed values of relative CFL thickness δ/R as a function of vessel radius R for discharge hematocrit $H_d = 0.45$. Experimental data are from [149, 159, 186].

4.5.2 Flow velocity profiles

We compare the velocity profile $v_z(r)$ predicted with our model with its counterpart constructed from experimental micro-PIV (Particle Image Velocimetry) measurements of velocity profiles of human blood flow in glass tubes [109]. Figure 4.8 shows the predicted and observed velocity profiles for discharge hematocrit $H_d = 0.335$, pressure gradient $J = 3732$ dyn/cm^3 and tube radius $R = 27.1$ μm used in the experiment [109]. The mean square-root error between the data and predictions is 0.068.

A location of the kink in the experimentally measured velocity profile ($r/R \approx 0.92$ in Figure 4.8) indicates a position of the core/CFL interface $r = R - \delta$). Applied to the experimental data in [109] (see Figure 4.8), this yields $\delta \approx 2.2$ μm. This estimate of the CFL thickness δ is much closer to that predicted by our model ($\delta = 2.48$ μm) than values for δ reported in earlier models [56, 172].
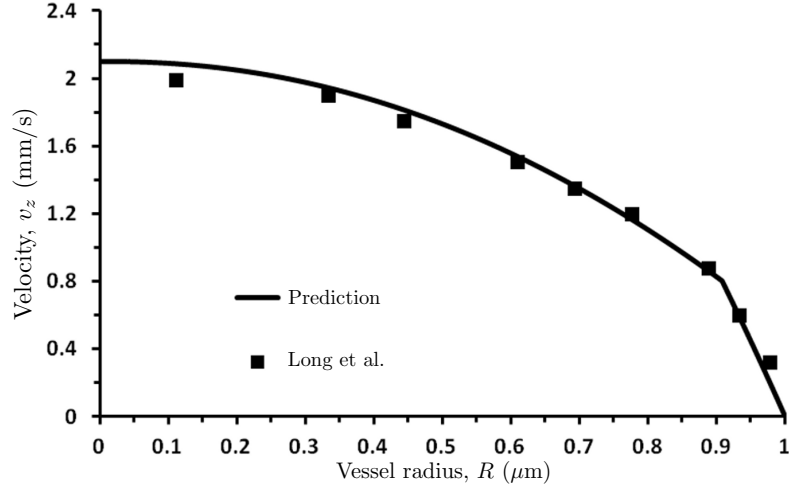
Figure 4.8: Predicted and observed velocity profiles, plotted against normalized radial distance from centerline r/R, for discharge hematocrit $H_d = 0.335$, pressure gradient $J = 3732$ dyn/cm^3 and tube radius $R = 27.1$ μm used in the experiment [109].

4.5.3 Tube hematocrit

As a final validation test, we investigate the ability of our model to reproduce measurements of tube hematocrit H_t, which is defined as the average (over a vessel's cross-section) hematocrit [172],

$$H_t \equiv \frac{2}{R^2} \int_0^R H(r) r \mathrm{d}r. \tag{4.16}$$

In the two-phase fluid model under consideration, $H(r) = H_c$ inside the RBC-rich core $(0 \leq r \leq R - \delta)$ and $H(r) = 0$ inside the CFL $(R - \delta < r \leq R)$. Therefore, this equation predicts a linear relationship between tube hematocrit H_t and core hematocrit H_c [172],

$$H_t = \frac{(R - \delta)^2}{R^2} H_c. \tag{4.17}$$

Measurements of tube hematocrit H_t are typically reported relative to discharge hematocrit H_d, i.e., as the ratio H_t/H_d. This ratio is observed to be smaller than unity, a phenomenon that is referred to as the Fahraeus effect [54]. The disparity between values of tube hematocrit H_t and discharge hematocrit H_d is due to the presence of the CFL; the difference between the three types of hematocrit diminishes, $H_t \approx H_c \approx H_d$, as $\delta/R \to 0$.

Figure 4.9 shows the observed [56, 72, 78, 149] and computed dependence of H_t/H_d on vessel diameter D for $H_d = 0.405$. While the mean root-mean-square error (RMSE) between the data and predictions is relatively large (RMSE = 0.052), our model captures the key features of this dependence. The ratio H_t/H_d increases as with vessel radius R, approaching its limiting value of 1 at large R ($\delta/R \rightarrow 0$). Moreover, the absolute difference between our calculations and the experimental data does not exceed 11 % and is significantly smaller (less than 4 %) for many data points over a wide range of vessel diameters.
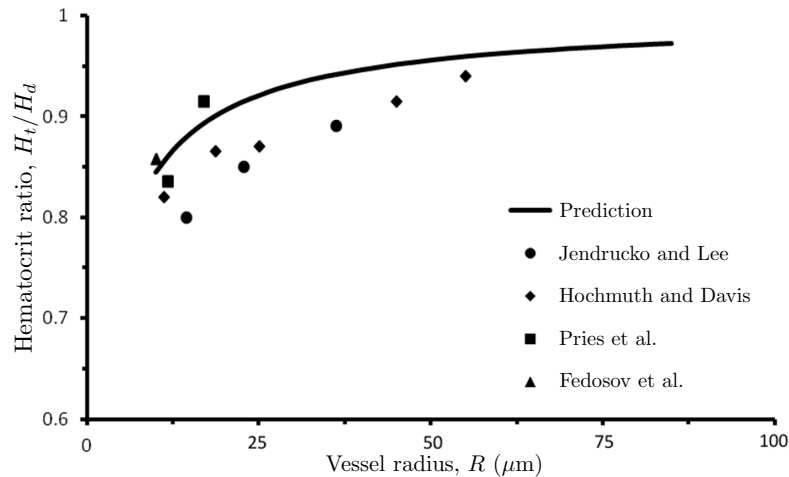
Figure 4.9: Calculated and measured values of H_t/H_d as a function of vessel radius R, for $H_d = 0.405$. Experimental data are from [56, 72, 78, 149].

4.6 Simulation results

The results presented in this section are for pressure gradient $J = 40,000 \text{ dyn/cm}^3$. The latter corresponds to wall shear stress of 40 dyn/cm^2 at $R = 20$ μm, a value consistent with in-vivo WSS measurements [106] typically observed in the microcirculation.

4.6.1 Flow velocity profiles

The velocity profiles $v_z(r)$ computed with our model are blunted, rather than parabolic (Figure 4.10). Each profile is normalized with the corresponding maximum (centerline) velocity $v_{\max}$. In a blood vessel of radius $R = 20$ μm, $v_{\max} = 14.9, 11.0$

and 7.4 mm/s for discharge hematocrit $H_d = 0.35$, 0.45 and 0.55, respectively. In a blood vessel of radius $R = 40$ μm, these increase to $v_{\max} = 25.1$, 39.0 and 55.0 mm/s for the respective values of discharge hematocrit H_d. Figure 4.10 also shows the parabolic velocity profiles that arise from the Poiseuille solution for pipe flow.
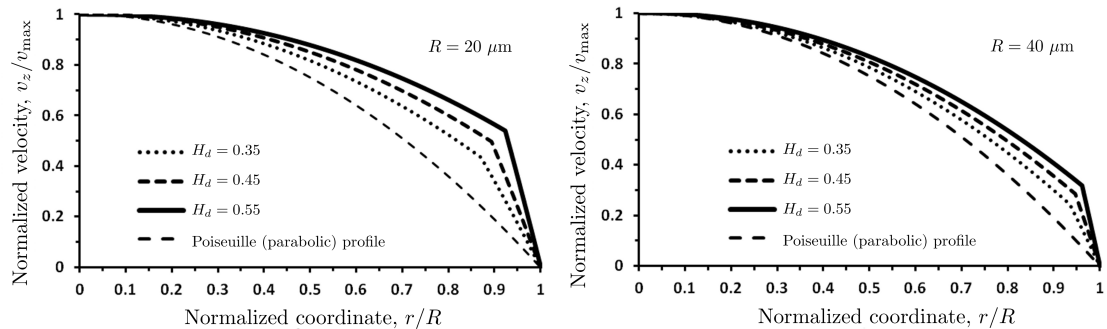
Figure 4.10: Velocity profiles $v_z(r/R)$, normalized with corresponding maximum (centerline) velocities $v_{\max}$, for vessel radii $R = 20$ μm (left) and 40 μm (right) and several values of discharge hematocrit H_d. Also shown is the (normalized) parabolic velocity profile predicted by the Poiseuille law.

The bluntness of the velocity profiles increases with the discharge hematocrit H_d due to two reasons. First, the non-Newtonian behavior of blood becomes more pronounced as hematocrit increases. Second, higher levels of hematocrit lead to higher viscosities of the RBC-rich core, increasing the contrast between the viscosities of the core and the CFL.

Figure 4.10 also reveals that the non-Newtonian behavior of blood is less pronounced, i.e., the deviation from the Poiseuille's parabolic velocity profile is less significant, in larger vessels. This observation is in line with the standard modeling practice of modeling blood in large vessels as a Newtonian fluid.

4.6.2 Relationship between core and discharge hematocrits

Mass conservation of RBCs, as expressed by Eq (C.4), establishes a linear relationship between the core (H_c) and discharge (H_d) hematocrits (see, also, [179]). Additionally, it defines the (nonlinear) dependence of the hematocrit ratio H_c/H_d on the blood vessel radius R. This dependence, computed with the algorithm of Section 4.7.1,

is displayed in Figure 4.11 for several values of the discharge hematocrit H_d. As vessel radii become larger, the difference between the core and discharge hematocrits becomes less significant, i.e., the ratio $H_c/H_d \to 1$.
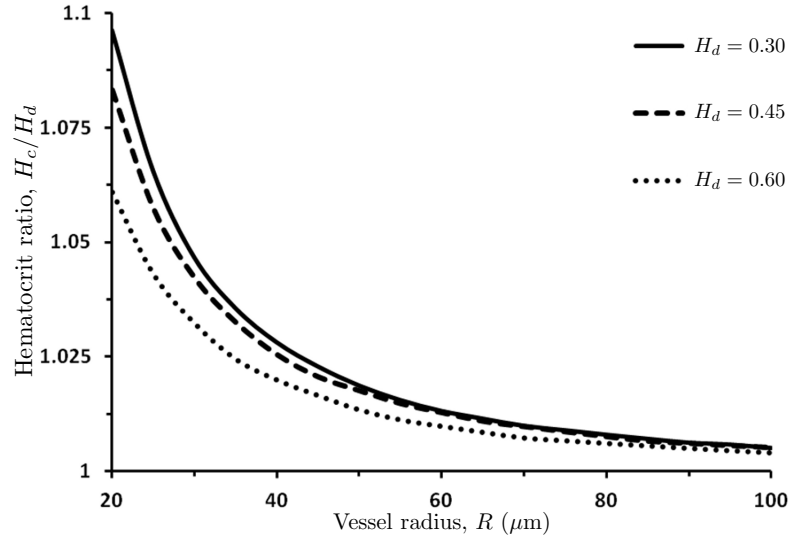
Figure 4.11: Hematocrit ratio H_c/H_d as a function of blood vessel radius R for several values of discharge hematocrit H_d.

4.6.3 Comparison with the two-layer Newtonian model

Several studies, e.g., [130, 172, 179], treated blood as a two-phase fluid (as we do) but assumed that both the RBC-rich core and the CFL exhibit Newtonian behavior. Comparison of these models with ours sheds light on the impact of the non-Newtonian effects on predictions of both the flow velocity v_z and the relative apparent viscosity $\mu_{\rm rel}$.

Figure 4.12 shows the velocity profiles $v_z(r)$ in a vessel of radius $R = 20$ μm, computed with the two-phase Newtonian model [130, 172, 179] (see Appendix C) and our two-phase Quemada model. Each of these velocity profiles is normalized with its maximum (centerline) velocity $v_{\rm max}$ (= 1.845 and 1.286 mm/s for the Newtonian and Quemada and models, respectively). Both profiles differ significantly from the parabolic profile predicted by the Poiseuille law. The Newtonian assumption significantly overestimates flow velocity ($v_{\rm max}$ by about 50%) and underestimates the degree of bluntness of the velocity profile. This is despite the fact that the CFL thickness δ predicted with
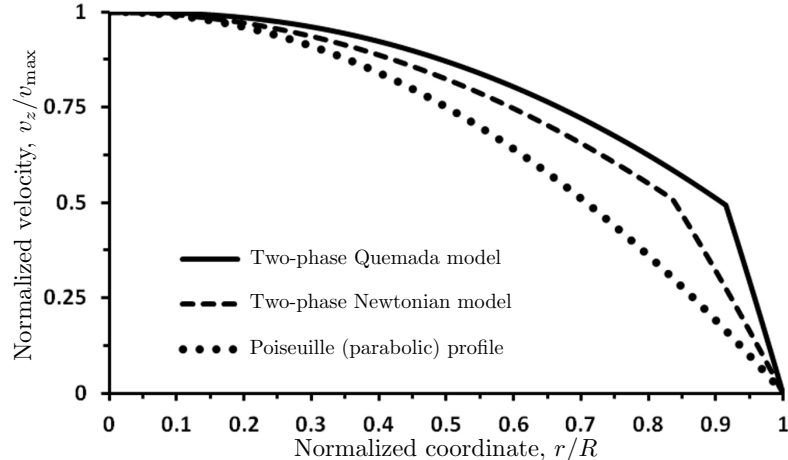
Figure 4.12: Normalized velocity profiles computed with the two-phase Newtonian model [130, 172, 179], our two-phase Quemada model, and the Poiseuille law. Each velocity $v_z(r/R)$ is normalized with its maximum (centerline) velocities v_{max}. The vessel radius is $R = 20$ μm and discharge hematocrit is $H_d = 0.45$.

our model is smaller than that suggested in [172]. It is worthwhile emphasizing that the values of δ predicted with our model fall within the experimentally observed range (1.5 - 3.0 μm), while the estimates of δ in [172] (3.5 - 4.0 μm) do not.

Figure 4.13 exhibits the dependence of relative apparent viscosity μ_{rel} on vessel radius R predicted with the two-phase Newtonian model [130, 172, 179], our two-phase Quemada model, and the data-fitted curve (4.14) of Pries et al. [151]. The Newtonian model [130, 172, 179] underestimates the apparent viscosity, as compared to both our Quemada model and the experimental data in [151]. This demonstrates the importance of accounting for non-Newtonian shear-thinning behavior of the RBC-rich core.

4.7 Consequences for WSS measurements in blood vessels

Measurements of WSS in arterioles are typically done (e.g., [87, 160]) by employing the Poiseuille law, $Q = \pi J R^4/(8\mu)$, to express WSS $\tau_w = \tau(R)$ in terms of observable quantities such as flow rate Q, average flow velocity $v_{ave} \equiv Q/(\pi R^2) = J R^2/(8\mu)$ or centerline velocity $v_{max} = 2v_{ave}$. This is accomplished by combining Eq (4.6) with $\tau = \mu\gamma$, the Newtonian relationship between shear stress τ and shear rate $\gamma = dv_z/dr$. Since for
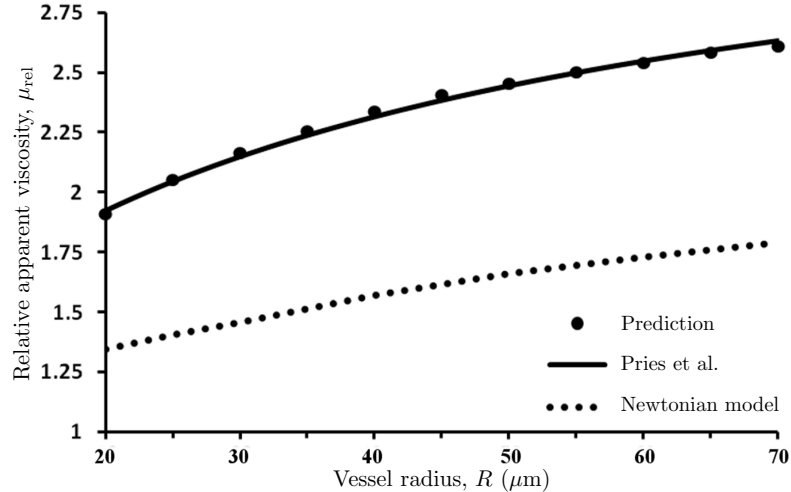
Figure 4.13: Dependence of relative apparent viscosity μ_{rel} on vessel radius R, computed with the two-phase Newtonian model [130, 172, 179], our two-layer Quemada model, and the data-fitted curve of Pries et al. [151]. Discharge hematocrit is $H_d = 0.45$.

a Poiseuille flow the shear rate at the wall is given by $\gamma_w \equiv \gamma(R) = 2v_{\mathrm{max}}/R$, one obtains

$$\tau_{w,\mathrm{P}} = \frac{2\mu_p v_{\mathrm{max}}}{R}. \tag{4.18}$$

While Eq (4.18) is routinely used to estimate the WSS τ_w from experiments [87, 160], it is important to recognize that it is based on the assumption that blood can be treated as a homogeneous Newtonian fluid.

Many theoretical and experimental studies, including our analysis in Section 4.6, demonstrate the importance of accounting for the non-Newtonian behavior of blood flow in micro-vessels. Experimental techniques, such as microparticle image velocimetry [109], enable one to obviate the need for this assumption by inferring the WSS τ_w from measurements of the entire velocity profile $v_z(r)$. However they are expensive and operationally challenging, which hinders their in-vivo use [87, 160]. We propose an efficient alternative that utilizes standard experimental procedures to determine the discharge hematocrit H_d and a flow characteristic (Q, v_{ave} or v_{max}), relies on the modeling algorithm in Section 4.7.1 to compute the wall shear rate $\gamma_w = \gamma(R)$, and makes use of the Quemada constitutive law (4.1) to relate the wall shear rate γ_w to the WSS τ_w.

4.7.1 Algorithm for inference of WSS from blood flow measurements

Given measurements of the vessel radius R, centerline velocity $v_{\max}$ and discharge hematocrit H_d, we employ the following algorithm to determine the WSS τ_w.

1. Set the counter to $n = 0$, the algorithm tolerance to $\epsilon = 10^{-4}$, and the iteration factor to $\kappa = 0.9$.

2. Compute an initial guess for the WSS $\tau_w^{(n)}$ by using the Poiseuille relation (4.18).

3. Compute the corresponding values of the pressure gradient $J^{(n)} = 2\tau_w^{(n)}/R$ from Eq (4.6).

4. Calculate the velocity profile $v^{(n)}(r)$ by using the algorithm in Section 3 with given $J^{(n)}$.

5. Compare the resulting centerline velocity $v_{\max}^{(n)}$ with its measured value $v_{\max}$. If

$$\left| \frac{v_{\max} - v_{\max}^{(n)}}{v_{\max}} \right| \leq \epsilon$$

then go to Step 7. Otherwise, modify the value of the pressure gradient according to

$$J^{(n+1)} = \left[1 + \kappa \frac{v_{\max} - v_{\max}^{(n)}}{v_{\max}} \right] J^{(n)}.$$

6. Set $n = n + 1$. Go to Step 4.

7. Compute the WSS $\tau_w = J^{(n)}R/2$ from Eq (4.6).

For $\kappa = 0.90$ and $\epsilon = 0.0001$, this algorithm converged in fewer than 20 iterations in all the cases we examined.

We use the relative error $\varepsilon_{\mathrm{WSS}} = (\tau_w - \tau_{w,\mathrm{P}})/\tau_w$ to quantify the errors introduced by relying on the Poiseuille relation (4.18) to infer the WSS ($\tau_{w,\mathrm{P}}$), i.e., by ignoring the inhomogeneity and non-Newtonian properties of blood flow in micro-vessels. Figure 4.14 reveals that the error $\varepsilon_{\mathrm{WSS}}$ is significant over wide ranges of the discharge hematocrit H_d and the blood vessel radius R. This demonstrates that the Poiseuille-law-based experimental inference of the WSS systematically underestimates the WSS in microcirculatory flows. The bias increases with the discharge hematocrit H_d and decreases with the vessel
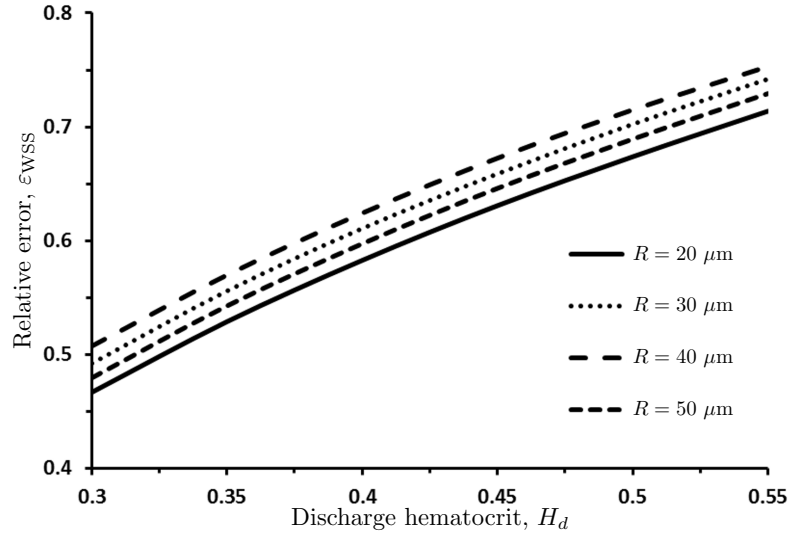
Figure 4.14: Relative error $\varepsilon_{\mathrm{WSS}} = (\tau_w - \tau_{w,\mathrm{P}})/\tau_w$ in estimation of the WSS τ_w introduced by relying on the Poiseuille relation (4.18) to infer the WSS ($\tau_{w,\mathrm{P}}$), for several values of vessel radius R.

radius R. Both phenomena are to be expected, since they amplify the non-Newtonian behavior of the blood flow in microcirculation (see Section 6).

4.7.2 Empirical WSS correction factor

The numerical algorithm described in Section 4.7.1 provides a rigorous means for inferring the WSS from measurements of R, H_d and v_{max}. Here we use it to pre-compute a correction factor $\phi(R, H_d)$, which would allow us to determine the WSS without resorting to numerical simulations. This correction factor allows one to determine the actual WSS τ_w from its Poiseuille-law estimate $\tau_{w,\mathrm{P}}$ given by Eq (4.18) by simple multiplication, $\tau_w = \phi(R, H_d)\tau_{w,\mathrm{P}}$, i.e.,

$$\tau_w = \frac{2\mu_p v_{\mathrm{max}}}{R}\phi(R, H_d). \tag{4.19}$$

The correction factor $\phi(R, H_d) = \tau_w/\tau_{w,\mathrm{P}}$ is calculated as follows. First, we employ the iterative algorithm of Section 4.7.1 to compute the WSS $\tau_w(R, H_s)$ for multiple values of $R \in [15\,\mu\mathrm{m}, 70\,\mu\mathrm{m}]$ and discharge hematocrit $H_d \in [0.25, 0.55]$. Then, for each of these computed values of the WSS, we obtain the correction factor as $\phi(R, H_d) = \tau_w/\tau_{w,\mathrm{P}}$. Finally, we interpolate this $\phi = \phi(R, H_d)$ data set with the curve

(with the goodness-of-the-fit exceeding 0.99)

$$\phi(R, H_d) = c_1 \ln R + c_0 \quad \text{where} \quad c_1 = 0.0515 \mathrm{e}^{4.732 H_d}, \quad c_0 = 0.6134 H_d + 1.0548. \quad (4.20)$$

Figure 4.15 exhibits the dependence of the WSS correction factor ϕ on the vessel radius R and discharge hematocrit H_d. Equation (4.20) and its graphical representation in Figure 4.15 show that the correction factor ϕ (and, hence, the errors introduced by the reliance of the Poiseuille law) grows exponentially with the discharge hematocrit H_d. Its dependence on the vessel radius R becomes more pronounced as the discharge hematocrit H_d increases.
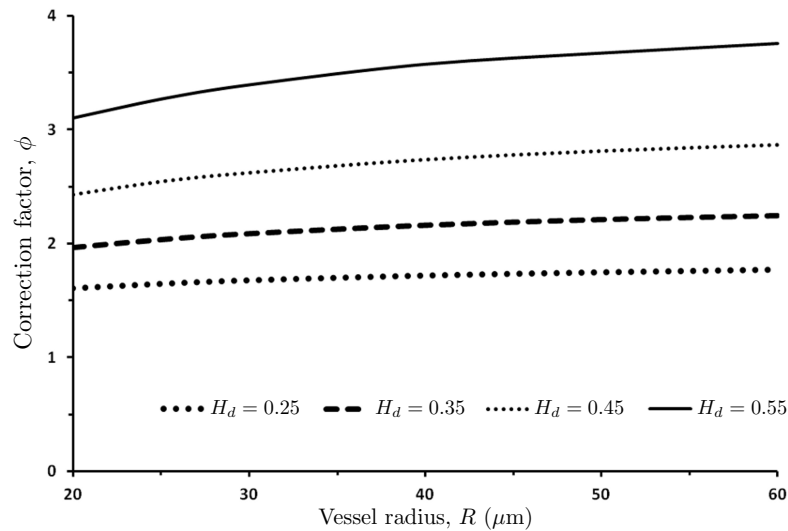
Figure 4.15: WSS correction factor ϕ as a function of vessel radius R, for several values of discharge hematocrit H_d.

We compared the WSS values computed with Eq (4.19), the iterative algorithm of Section 4.7.1 and the correction factor in Eq (4.20) for a physiologically relevant ranges of R and H_d. This comparison reveals that the iterative algorithm and the correction factor yield the nearly identical (within 3 %) estimates of WSS. Both sets of estimates are significantly higher than their counterparts predicted with the Poiseuille relation (4.18).

The results presented in this study are obtained for parameter values typical of human blood. Therefore, they are applicable both for in-vitro experiments in glass tubes [109] and tissue cultures [118], and for in-vivo observations such as retinal [165] or MRI [31] studies. For experiments that involve blood from other species, the approach used in

this study may be replicated with suitable rheological data for the type of blood under consideration as an input. This would require the measurements of the dependence of the CFL thickness δ on H_d and R, and blood rheology data (which is readily available in the literature for a number of species).

4.8   Discussion

We presented a two-layer fluid mechanics model in this study, with a non-Newtonian RBC core layer and a Newtonian cell free layer near the vessel wall. The rheology of the RBC core was modeled using the Quemada model [114, 133, 157] which accurately describes the shear thinning properties of blood over a large range of shear rates and hematocrits. Each fluid layer was assumed homogeneous and immiscible, with the resulting flow assumed to be laminar and axisymmetric.

In order to calculate velocity profiles using this model, we assumed a general functional form of the CFL thickness, δ as a function of discharge hematocrit H_d. We then used Eqs (4.7)–(4.11) to calculate flow velocities, flow rates and relative apparent viscosity μ_{rel}. We calibrated our expression for δ, given by Eq (4.11), so that our predictions for apparent viscosity at different hematocrits and radii were in agreement with the work of Pries et al. [151]. Figure 4.5 shows that our model was successfully able to match the predictions of Pries et al., providing validation to the assumption that δ is an almost linear function of discharge hematocrit and is independent of tube radius.

We were further able to validate our model by comparing i) the predicted velocity profiles with experimental data [109], ii) the predicted hematocrit ratio H_t/H_d vs values reported in the literature (both experimental data and numerical models), and iii) δ/R values with those estimated in experimental studies [159, 149, 186].

Agreement between our calculated and measured velocity profiles [109] is shown in Figure 4.8. The calculated values of velocity, shape of velocity profile and CFL thickness are in reasonable agreement with the experiment (see Section 5). Furthermore, our predictions for H_t/H_d fall within the broad range of values suggested in the literature (Figure 4.9). The scatter in the range of values reported is unfortunately rather large, with very few experiments being carried out in recent years with modern experimental

techniques. New experiments to measure tube vs discharge hematocrit would be very useful to help better calibrate flow models of blood flow in microvessels.

Our predictions of CFL thickness δ also seem to be in reasonable agreement with the experiments [90, 149, 159, 186]. Our estimates of δ are closer to the experimentally observed values than those reported in other theoretical studies [172, 56, 179]. The range of δ predicted for physiological levels of hematocrit (in the vicinity of 0.45) falls between 1.5 μm and 3 μm in most experimental studies. Our predictions of δ in the range of 2.5-1.8 μm over a range of hematocrits from 0.35 to 0.55 are within this range of experimentally measured values. Figure 4.7 shows that our estimates of δ/R vs R for $H_d = 0.45$ are in general agreement with the experimental observations [149, 159, 186].

We also demonstrated the resulting dependence of core hematocrit H_c on discharge hematocrit H_d in small to intermediate sized arterioles, as shown in Figure 4.11. As the vessel size increases, the importance of the Fahraeus effect [54] reduces and core and systemic hematocrit become essentially indistinguishable, due to the fact that the width of the cell depleted layer becomes negligible compared to vessel radius. Hence, we expect core hematocrit to be almost the same as discharge hematocrit in large blood vessels (where the core is essentially the entirety of the vessel cross section), but in smaller blood vessels the core hematocrit should be significantly elevated over systemic (or discharge) hematocrit.

We examined whether our model makes predictions that are different from the Newtonian model of blood flow used previously in [172, 179, 130]. Figure 4.12 provides a comparison of our predictions of the velocity profiles with those computed with the two-layer Newtonian model, for the vessel radius $R = 20$ μm and the pressure gradient $J = 40,000$ dyn/cm^3. Our two-layer non-Newtonian model predicts significantly smaller axial velocities and blunter velocity profiles than the two-layer Newtonian model does. Sharply blunted velocity profiles are commonly reported in the experimental literature [109, 59, 4, 18, 94, 188].

We also analyzed the dependence of the relative apparent viscosity on the vessel radius (see Figure 4.13, for $H_d = 0.45$). The Newtonian model significantly underestimates the relative apparent viscosities both predicted with our model and observed experimentally (see the data in [151]). Since, with a single optimized set of parameters

our model is able to simultaneously predict realistic values of apparent viscosity, CFL thickness, tube hematocrit and velocity profiles that are in broad agreement with the experimental literature, we submit that our model is a significant improvement over prior Newtonian flow models.

The blunting of velocity profiles discussed in this study has a number of consequences. Typical in vivo measurements of WSS in the microcirculation are based on the Poiseuille relation (4.18), which assumes the Newtonian behavior and results in parabolic velocity profiles [160, 87]. The errors introduced by this assumption lead to a significant underestimation of WSS. We proposed two methods to eliminate these errors: an iterative numerical algorithm which leverages our flow model, and the use of a simple correction factor that can be incorporated into the Poiseuille law. Given a rheological model of the RBC-rich core, both approaches allow the inference of WSS from measurements of vessel radius, centerline velocity and discharge hematocrit. Since the WSS values calculated with these two methods differ by approximately 3 %, one can rely on the correction factor without sacrificing the measurement accuracy. This correction factor varies with the discharge hematocrit H_d and vessel radius R, as shown in Figure 4.15. The proposed approach is also useful in models where WSS is an input for calculations of quantities such as shear-induced NO production [179, 178].

This analysis and the proposed correction factors should aid in evaluating the changes in shears stress induced by the changes of the composition of blood due to the application of plasma expanders that affect the blood's shear thinning properties [178]. The effects of this type of transfusional intervention appear to be significantly dependent on the rheological changes induced in diluted blood and are becoming the focus of research and development in designing new transfusion strategies [24].

sectionAcknowledgements

Chapter 5

On Optimal Branching of

Vascular Networks

Important Symbols used

Q, Q_n, Q_{n1}, Q_{n2}	Flow rate, Flow rate in parent vessel, in daughter vessel 1 and 2
H, H_n, H_{n1}, H_{n2}	Discharge hematocrit, in parent vessel, daughter vessel 1 and 2
R, R_n, R_{n1}, R_{n2}	Vessel radius, radius of parent vessel, daughter vessel 1 and 2
μ	Viscosity
μ_p	Plasma viscosity
ϕ_{ox}	Oxygen flux
a	Flux asymmetry parameter
W	Cost function
l	vessel length
τ	Wall Shear Stress (WSS)
J	Pressure gradient
P	Intraluminal Pressure

5.1 Introduction

Quantitative modeling of physiological processes in vasculatures requires an accurate representation of network topology, including vessel branching. The standard conceptualization of a vascular network assumes both that each blood vessel bifurcates at successive levels of the network and that each bifurcation follows Murray's

law [129, 128] or its empirical modifications that are usually based on morphometric data [134, 86, 153]. In its general form, Murray's law states that a parent blood vessel of radius R_p branches into N daughter vessels of (possibly different) radii R_{d_i} ($i = 1, \ldots, N$) such that $R_p^3 = R_{d_1}^3 + \ldots + R_{d_N}^3$; bifurcating networks correspond to $N = 2$. A fundamental consequence of Murray's law is the predicted uniformity of wall shear stress (WSS) throughout the vasculature [173, 145, 86]. While Murray's law generally holds in the macrocirculation [100, 121], a number of in-vivo studies demonstrate its breakdown in microcirculatory networks.

Of particular physiological significance are observations, e.g., [153, 145, 86] among many others, of the WSS variability between various generations of the blood vessels in vascular networks. While the WSS remains relatively constant over much of the vascular network, it increases significantly in the microcirculation, particularly in the smallest segments of the pre-capillary arteriolar network [153, 107, 86]. This deviation from Murray's law has been attributed to the non-Newtonian shear-thinning behavior of blood in the vessels of small radii [2, 161]. Murray's law fails to capture such a behavior, since it is derived by assuming blood to be a Newtonian fluid, whose flow within each vessel obeys Poiseuille law [129].

The rheology of blood and, therefore, its non-Newtonian behavior depends on hematocrit. Specifically, both the blood viscosity and the shear-thinning rate increase with hematocrit [168, 145, 152, 155]. This phenomenon was ignored by Revellin et al. [161], who modified Murray's law by treating blood as an Ostwald de Waele fluid whose rheology and apparent viscosity are independent of either hematocrit or vessel radius. The latter assumptions contradict in vitro [152] and in vivo [155] observations that revealed the strong dependence of apparent viscosity on both hematocrit and vessel radius. Alarcon et al. [2] accounted for these effects by employing the Pries et al. [155] constitutive relation, according to which apparent blood viscosity varies with vessel radius and hematocrit. This generalization of Murray's law rests on the assumption that hematocrits in the parent and daughter vessels are given by the ratio of average velocities in each daughter vessel. It leads to predictions of hematocrit values in the terminal regions of the network, which are unrealistically low [2].

The question of how hematocrit is partitioned between the parent and daughter

vessels remains open. In-vivo and in-vitro experimental data on hematocrit partition at bifurcations typically relate the flux fraction F_{RBC}, i.e., the fraction of RBCs flowing from the parent vessel into the larger daughter vessel, to the flow fraction F_{blood}, i.e, the fraction of total fluid flow from the parent vessel that enters the larger daughter vessel (see [12] and the references therein). Mathematical models [10, 11] of hematocrit partitioning at bifurcations are limited to two-dimensional channel flows. They suggest an approximately linear dependence of F_{RBC} on F_{blood} over a wide range of F_{blood}. While some experimental studies [57, 47, 92, 174] observed a linear relation between F_{RBC} and F_{blood}, the others [150, 154, 77] found this relationship to be highly non-linear. Even when the linear behavior is observed, the corresponding slopes and intercepts tend to be different.

We propose a mathematical framework for construction of vascular networks, which possess both an optimal vessel bifurcation and an optimal partition of hematocrit between daughter vessels. These two goals are achieved by postulating that healthy vasculatures are constructed in a way that optimizes oxygen delivery to the surrounding tissue. Our model builds upon the analysis of Alarcon et al. [2] in the sense that it generalizes Murray's law by accounting for both the non-Newtonian nature of blood flow in microcirculation and the dependence of blood rheology on hematocrit. Unlike Alarcon et al. [2], we impose no prior restrictions on the hematocrit partition between daughter vessels. Instead it is determined by solving an optimization problem. The outcome of our model is a vascular network in which both the bifurcation asymmetry and WSS vary from one generation of the network to the next. We demonstrate that the resulting vascular networks satisfy a number of properties of vascular networks identified from in-vivo studies, such as non-uniform shear stress and capillary hematocrit, branching exponents, and sharply amplified pressure gradients at the terminal vessels.

5.2   Problem Formulation

We consider blood flow in a regular vascular network composed of branching (bifurcating) vessels. Blood is treated as a non-Newtonian fluid whose apparent dynamic viscosity μ varies with a vessel radius R and hematocrit H in accordance with an

empirical rheological law of Pries et al. [155],

$$\mu(R, H) = \mu_p \left[1 + (\mu_{0.45} - 1) \frac{(1 - H)^\theta - 1}{(1 - 0.45)^\theta - 1} \left(\frac{2R}{2R - 1.1} \right)^2 \right] \left(\frac{2R}{2R - 1.1} \right)^2. \qquad (5.1)$$

Here μ_p is the dynamic viscosity of plasma, the dynamic viscosity of blood at hematocrit $H = 0.45$ is related to the vessel radius R by

$$\mu_{0.45}(R) = 3.2 + 6\,e^{-0.17R} - 2.44\,e^{-0.06(2R)^{0.645}}, \qquad (5.2)$$

and the exponent θ varies with the vessel radius R according to

$$\theta(R) = (0.8 + e^{-0.15R}) \left(-1 + \frac{1}{1 + 10^{-11}(2R)^{12}} \right) + \frac{1}{1 + 10^{-11}\,(2R)^{12}}. \qquad (5.3)$$

This dependence of the blood viscosity μ on vessel radius R and hematocrit H is shown in Figure 5.1.
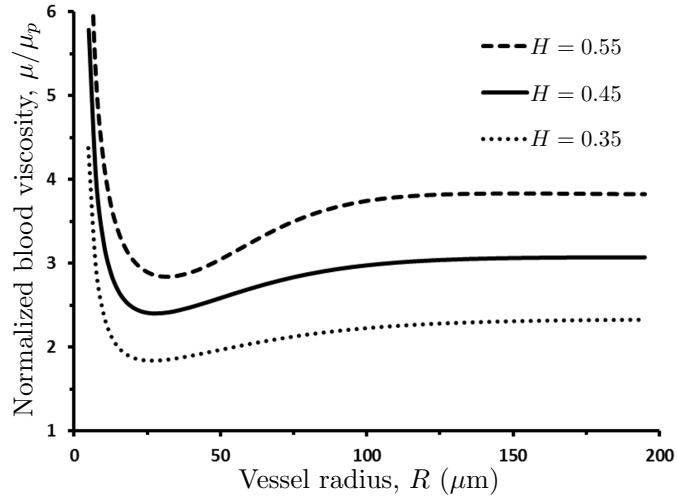
Figure 5.1: Dependence of the normalized apparent blood viscosity, μ/μ_p, on the vessel radius R and hematocrit H predicted with the rheological law of Pries et al. [155].

Following [12] we assume flow within each vessel to be steady, laminar, and fully developed, i.e., to obey a Poiseuille-like relationship between Q (the volumetric flow rate) and J (the pressure drop over the vessel's length L),

$$Q = \frac{JR^4}{8\pi\mu(R, H)}. \qquad (5.4)$$

In the n-th generation of the network, a parent vessel of radius R_n bifurcates into smaller daughter vessels with radii $R_{n,1}$ and $R_{n,2}$. The discharge hematocrit H_n in the parent

vessel partitions into the discharge hematocrits $H_{n,1}$ and $H_{n,2}$ in the corresponding daughter vessels. If the oxygen flux in a parent vessel is Q_{O_2}, then the mass conservation requires the oxygen fluxes in its daughter vessels to be aQ_{O_2} and $(1-a)Q_{O_2}$; the flux-asymmetry parameter a is a number between 0 and 1. In the following sections, we compute the daughter vessel radii and hematocrits by postulating that *the daughter vessels bifurcate in a way that minimizes the total cost associated with oxygen delivery to the tissue downstream of the bifurcation.*

5.3 State-of-the-Art in Vasculature Representation

5.3.1 Optimal vessel radius

The starting point of our analysis is the Murray cost function [128],

$$W = QJL + \alpha\pi R^2 L, \tag{5.5}$$

which combines the mechanical work (QJL) necessary to drive blood through a blood vessel of radius R and length L with the "metabolic cost" ($\alpha\pi R^2 L$). The latter is linearly proportional to the vessel's volume $\pi R^2 L$ with the coefficient of proportionality α. According to Murray's law, blood vessels have radii that minimize the cost function W for given flow rate Q and pressure gradient J, i.e., satisfy an equation $\mathrm{d}W/\mathrm{d}R = 0$. Combined with Eq. (5.4) this defines the optimal vessel radius $R^\star$ as a solution of

$$\frac{\mathrm{d}}{\mathrm{d}R}\left(\frac{8\mu Q^2}{\pi R^4} + \alpha\pi R^2\right) = 0. \tag{5.6}$$

If the blood viscosity μ were independent of the vessel radius R, this equation would yield Murray's law, according to which Q is proportional to R^3 [128]. For the blood viscosity $\mu(R, H)$ that varies with the vessel radius R in accordance with Eq. (5.1), the optimal radius $R^\star$ is a solution of [2]

$$Q = \frac{\pi\sqrt{\alpha}}{2}\frac{R^3}{\Lambda}, \qquad \Lambda(R, H) = \sqrt{4\mu - R\frac{\mathrm{d}\mu}{\mathrm{d}R}}. \tag{5.7}$$

For small H and large R (larger than 200 μm), the correction factor Λ is approximately constant (Figure 5.2) and Murray's law is recovered. For physiological values of hematocrit and vessel radii typically seen in the microcirculation (less than 100 μm), Λ has a strong dependence on R that is not captured by Murray's law.

Substituting the optimal Q and $R^\star$ into Eq. (5.5) gives the optimal (minimum) cost of supplying a volume of blood to a block of tissue,

$$W^\star = \alpha \pi L R^{\star 2} \left[\frac{2\mu(R^\star, H)}{\Lambda^2(R^\star, H)} + 1 \right]. \tag{5.8}$$

This analysis enables one to determine the optimal radius of a single blood vessel, if the discharge hematocrit H and the flow rate Q are known. The identification of the radii of daughter vessels of a bifurcating parent vessel requires additional assumptions.
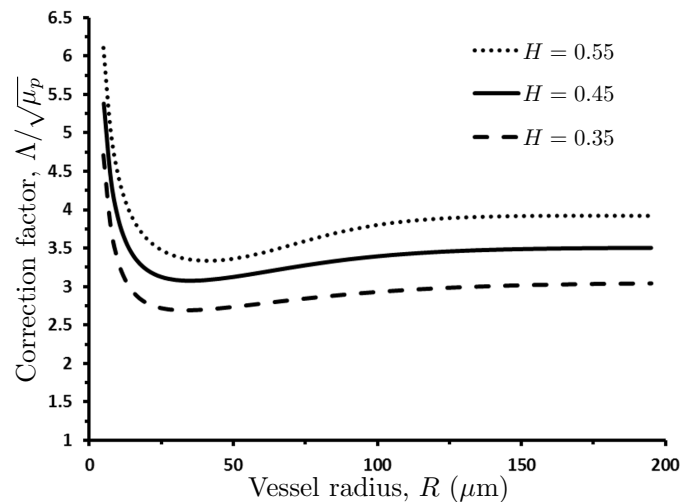
Figure 5.2: Dependence of the normalized correction factor, $\Lambda/\sqrt{\mu_p}$, in the modified version [2] of Murray's law on vessel radius R and hematocrit H. For vessel radii $R \geq 200$ μm and small values of hematocrit H, Λ is approximately constant and Murray's law is recovered.

5.3.2 Models of vessel bifurcation

The bifurcation of a parent vessel of radius R_n into daughter vessels with radii $R_{n,1}$ and $R_{n,2}$ is accompanied by the partitioning of the discharge hematocrit H_n in the parent vessel into the discharge hematocrits $H_{n,1}$ and $H_{n,2}$. The volumetric flow rates of blood in the parent (Q_n) and daughter ($Q_{n,1}$ and $Q_{n,2}$) vessels satisfy mass conservation,

$$Q_n = Q_{n,1} + Q_{n,2}. \tag{5.9}$$

Mass conservation of red blood cells imposes a constraint on the discharge hematocrits in the parent (Q_n) and daughter ($Q_{n,1}$ and $Q_{n,2}$) vessels,

$$Q_n H_n = Q_{n,1} H_{n,1} + Q_{n,2} H_{n,2}. \tag{5.10}$$

The volumetric flow rates in each vessel are given by the modified Murray's law (Eq. 5.7),

$$Q_n = \frac{\pi\sqrt{\alpha}}{2} \frac{R_n^3}{\Lambda(R_n, H_n)}; \qquad Q_{n,1} = \frac{\pi\sqrt{\alpha}}{2} \frac{R_{n,1}^3}{\Lambda(R_{n,1}, H_{n,1})}; \qquad Q_{n,2} = \frac{\pi\sqrt{\alpha}}{2} \frac{R_{n,2}^3}{\Lambda(R_{n,2}, H_{n,2})}. \tag{5.11}$$

Substituting Eq. (5.11) into Eqs. (5.9) and (5.10) yields

$$\frac{R_n^3}{\Lambda(R_n, H_n)} = \frac{R_{n,1}^3}{\Lambda(R_{n,1}, H_{n,1})} + \frac{R_{n,2}^3}{\Lambda(R_{n,2}, H_{n,2})} \tag{5.12a}$$

and

$$\frac{H_n R_n^3}{\Lambda(R_n, H_n)} = \frac{H_{n,1} R_{n,1}^3}{\Lambda(R_{n,1}, H_{n,1})} + \frac{H_{n,2} R_{n,2}^3}{\Lambda(R_{n,2}, H_{n,2})}. \tag{5.12b}$$

Since these two equations contain four unknowns ($R_{n,1}$, $R_{n,2}$, $H_{n,1}$, and $H_{n,2}$), the determination of the optimal bifurcation radii requires additional assumptions. For example, one can postulate that the daughter vessels have identical radii, $R_{n,1} = R_{n,2} \equiv R_{n,d}$ (i.e., $Q_{n,1} = Q_{n,2} = Q_n/2$), and assume that the discharge hematocrit in all the vessels is the same, $H_n = H_{n,1} = H_{n,2} \equiv H$. This model implies that the discharge hematocrit remains constant throughout the vascular network and relates the daughter-vessel radius to the radius of its parent by an implicit relation $2R_{n,d}^3/\Lambda(R_{n,d}, H) = R_n^3/\Lambda(R_n, H)$. Unfortunately the symmetrically bifurcating networks are not representative of typical vasculatures.

The construction of asymmetrically bifurcating vascular networks relies on Eqs. (5.12) supplemented with the following two assumptions. First, one assumes the ratio of the two daughter-vessel radii, $R_{n,1}/R_{n,2}$, to be known [134, 2, 86]. Second, one postulates a constitutive relation that governs the partition of discharge hematocrit between the two daughter vessels [2]. The shortcomings of the latter assumption are discussed the Introduction.

5.4 Bifurcations Optimal for Oxygen Delivery

We posit that biological vascular networks are structured in a way that maximizes its ability to deliver oxygen. Specifically, we postulate that

1. asymmetric bifurcations occur because the volumes of tissue downstream of each daughter vessel have different oxygen needs;

2. these needs are quantified by a known constant a $(0 < a < 1)$, which serves to partition the oxygen flux Q_{O_2} in any given parent vessel into the oxygen fluxes aQ_{O_2} and $(1 - a)Q_{O_2}$ in its two daughter vessels;

3. an optimal bifurcation is one in which the oxygen demands of each downstream tissue volume are supplied at a "minimal total cost"; and

4. the amount of oxygen transported through a blood vessel is proportional to the number of red blood cells flowing through that vessel [183], i.e., the oxygen flux is given by $Q_{O_2} = Q_n H_n$.

The value of a depends on the physiology of the downstream volumes of tissue supplied by each daughter vessel (symmetric bifurcations imply that these volumes are identical, so that $a = 0.5$).

If the oxygen flux in the n-th vessel is Q_{O_2}, then the oxygen fluxes in the two daughter vessels are $aQ_{O_2} = Q_{n,1}H_{n,1}$ and $(1 - a)Q_{O_2} = Q_{n,2}H_{n,2}$. It follows from Eq. (5.11) that the oxygen flux in the n-th vessel,

$$Q_{O_2} = \frac{\pi\sqrt{\alpha}}{2} \frac{R_n^3 H_n}{\Lambda(R_n, H_n)}, \tag{5.13}$$

partitions into the oxygen fluxes in its two daughter vessels, aQ_{O_2} and $(1 - a)Q_{O_2}$, according to

$$aQ_{O_2} = \frac{\pi\sqrt{\alpha}}{2} \frac{R_{n,1}^3 H_{n,1}}{\Lambda(R_{n,1}, H_{n,1})} \quad \text{and} \quad (1 - a)Q_{O_2} = \frac{\pi\sqrt{\alpha}}{2} \frac{R_{n,2}^3 H_{n,2}}{\Lambda(R_{n,2}, H_{n,2})}. \tag{5.14}$$

A constraint on the hematocrit partitioning between the two daughter vessels is obtained by substituting $Q_n = Q_{O_2}/H_n$, $Q_{n,1} = aQ_{O_2}/H_{n,1}$ and $Q_{n,2} = (1 - a)Q_{O_2}/H_{n,2}$ into Eq. (5.9), which yields

$$\frac{1}{H_n} = \frac{a}{H_{n,1}} + \frac{1 - a}{H_{n,2}}. \tag{5.15}$$

Three Eqs. (5.14) and (5.15) contain four unknowns ($R_{n,1}$, $R_{n,2}$, $H_{n,1}$, and $H_{n,2}$). The fourth equation needed to close this system is obtained by assuming that vascular networks are formed in a way that minimizes the work necessary to distribute oxygen throughout the vasculature. The cumulative work of forcing the blood through the two daughter vessels of the n-th parent vessel is computed from Eq. (5.5) as $W = (Q_{n,1}J_{n,1}L_{n,1} + \alpha\pi R_{n,1}^2 L_{n,1}) + (Q_{n,2}J_{n,2}L_{n,2} + \alpha\pi R_{n,2}^2 L_{n,2})$, where $L_{n,1}$ and $L_{n,2}$ are the (yet unknown) lengths of the daughter vessels. In analogy with Eq. (5.8), for any given partitioning of the hematocrit the minimum Murray's work has the form

$$W^\star = \alpha\pi L_{n,1} R_{n,1}^2 \left[\frac{2\mu(R_{n,1}, H_{n,1})}{\Lambda^2(R_{n,1}, H_{n,1})} + 1\right] + \alpha\pi L_{n,2} R_{n,2}^2 \left[\frac{2\mu(R_{n,2}, H_{n,2})}{\Lambda^2(R_{n,2}, H_{n,2})} + 1\right]. \quad (5.16)$$

The optimal hematocrit partitioning minimizes the total work in Eq. (5.16), giving rise to the fourth equation,

$$\frac{\mathrm{d}W^\star}{\mathrm{d}H_{n,1}} = 0, \quad (5.17)$$

where Eq. (5.15) is used to express $H_{n,2}$ in terms of $H_{n,1}$.

The system of Eqs. (5.14), (5.15) and (5.17) remains unclosed due to the presence of two additional unknowns: the daughter vessel lengths $L_{n,1}$ and $L_{n,2}$. These are often related to the corresponding vessel radii $R_{n,1}$ and $R_{n,2}$, e.g., by assuming the radius-to-length ratio $R_{n,1}/L_{n,1} = R_{n,2}/L_{n,2}$ to be constant throughout the vascular network (i.e., for any n) [134, 86, 40, 41]. This assumption is supported by in-vivo morphological studies of arterial trees [68, 119]. Rather then forcing the radius-to-length ratio to be constant, we supplement the four postulates listed above with the following hypothesis:

5. A blood vessel's volume, $\pi R^2 L$, is linearly proportional to the volume of tissue it oxygenates.

We show in the Appendix that this assumption leads to a radius-to-length relationship,

$$L = \frac{\kappa H R}{\Lambda(R, H)}, \quad (5.18)$$

where κ is a constant model parameter. Setting $\kappa = 650\sqrt{\mu_p}$ in Eq. (5.18) results in the L/R ratios between 50 and 100 depending on the value of discharge hematocrit H (Figure 5.3), which falls within the range of the reported length-to-radius ratios [134, 40, 86, 68].

Figure 5.3 reveals that in blood vessels with $R > 150$ μm the length-radius ratios do become constant, with their value decreasing with hematocrit H. This leads us to conclude that the length-to-radius ratio (L/R) may be assumed constant over the bulk of a vascular tree, with deviations from its constant value occurring in small, pre-capillary arterioles.
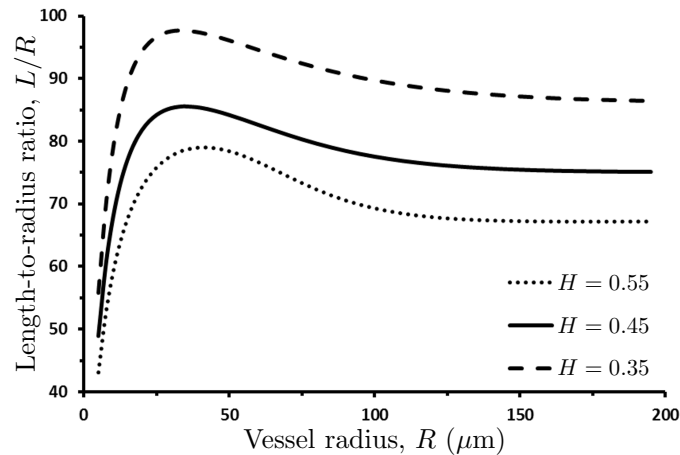
Figure 5.3: Variation of length-radius ratio, L/R with vessel radius R for several values of discharge hematocrit H. The length-to-radius ratio L/R may be assumed constant over the bulk of a vascular tree, with deviations from its constant value occurring in small, pre-capillary arterioles.

Given values of the discharge hematocrit H_n and the oxygen flux Q_{O_2} in the n parent vessel and its radius R_n, the radii ($R_{n,1}$ and $R_{n,2}$) and lengths ($L_{n,1}$ and $L_{n,2}$) of, and the hematocrits ($H_{n,1}$ and $H_{n,2}$) in, the bifurcating daughter vessels are uniquely determined by the system of nonlinear Eqs. (5.14), (5.15), (5.17) and (5.18).

The radii of the daughter vessels, $R_{n,1}$ and $R_{n,2}$, predicted with our model are reported in Figure 5.4 in terms of their ratio $R_{n,1}/R_{n,2}$. The symmetric bifurcation ($R_{n,1} = R_{n,2}$) occurs when the bifurcation parameter $a = 0.5$. The values $0.5 < a < 1$ result in $R_{n,1} > R_{n,2}$, while values $0 < a < 0.5$ (not shown in Figure 5.4) yield $R_{n,1} < R_{n,2}$. The bifurcation asymmetry increases with the parent vessel's radius R_n, as long as $R_n \leq 80$ μm. After that threshold the ratio $R_{n,1}/R_{n,2}$ is independent of R_n, so that the curves $R_{n,1}/R_{n,2}$ vs a overlap with that for $R_n = 80$ μm.
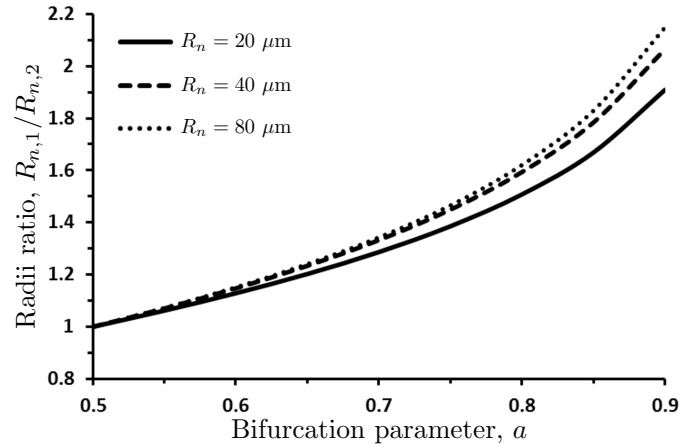
Figure 5.4: Ratio $R_{n,1}/R_{n,2}$ of the radii of the two daughter vessels as a function of the bifurcation parameter a for several values of the parent vessel radius R_n and hematocrit $H_n = 0.45$. The symmetric bifurcation ($R_{n,1} = R_{n,2}$) occurs when the bifurcation parameter $a = 0.5$.

Figure 5.5 shows the partitioning of hematocrit $H_n = 0.45$ in the parent vessel into hematocrits $H_{n,1}$ and $H_{n,2}$ in the daughter vessels for several values of the parent vessel radius R_n and the bifurcation parameter a. While hematocrit in the larger daughter vessel ($H_{n,1}$) is nearly the same as hematocrit in the parent vessel (H_n), hematocrit in the smaller daughter vessel ($H_{n,2}$) is significantly different from H_n. This is consistent with the observations reported in [57, 77, 47] and supports the idea that discharge hematocrit at the bifurcation partitions in a way that minimizes the work necessary to induce blood flow in microcirculation.

Dependence of the hematocrit ratio $H_{n,1}/H_{n,2}$ on the parent vessel radius R_n is elucidated further in Figure 5.6. Bifurcations of parent vessels with $R_n < 40$ μm result in the hematocrit ratios $H_{n,1}/H_{n,2} > 1$, i.e., hematocrit in the larger daughter vessel exceeds hematocrit in the smaller daughter vessel. The situation is reversed in parent vessels with $R_n > 40$ μm, which yield $H_{n,1}/H_{n,2} < 1$. As R_n increases, the hematocrit ratio $H_{n,1}/H_{n,2}$ asymptotically tends to 1. The inflection point of the $H_{n,1}/H_{n,2}$ vs R_n curves corresponds to the inflection point in the relationship between the apparent viscosity and vessel radius in Figure 5.1.
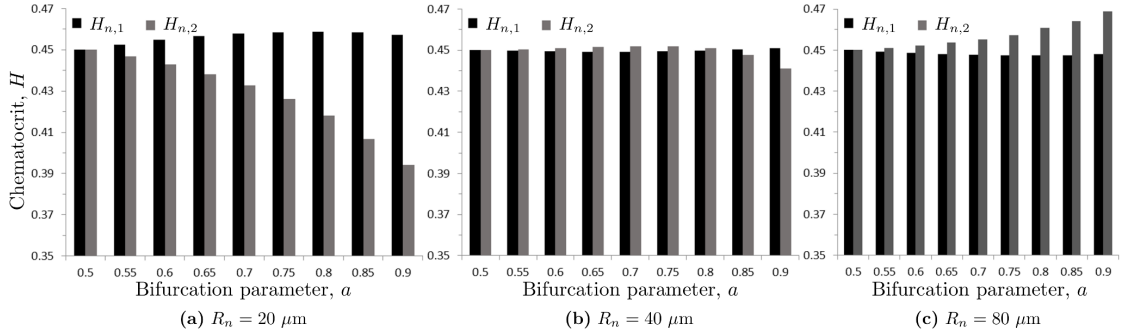
Figure 5.5: Partitioning of hematocrit $H_n = 0.45$ in the parent vessel into hematocrits $H_{n,1}$ and $H_{n,2}$ in the daughter vessels as a function of the bifurcation parameter a, for the parent vessel radius (a) $R_n = 20$ μm, (b) $R_n = 40$ μm and $R_n = 80$ μm. The symmetric bifurcation ($a = 0.5$) results in the uniform hematocrit in all three vessels, $H_n = H_{n,1} = H_{n,2} = 0.45$.

Experimental data on flow behavior at vessel bifurcations are typically reported in terms of the RBC flux fraction F_{RBC} and the blood flow fraction F_{blood} [174, 150, 57, 47]. These are defined as

$$F_{\text{RBC}} = \frac{Q_{n,1} H_{n,1}}{Q_n H_n}, \qquad F_{\text{blood}} = \frac{Q_{n,1}}{Q_n}. \tag{5.19}$$

Our model predicts the RBC flux fraction F_{RBC} to vary linearly with the flow fraction F_{blood} (Figure 5.7), in agreement with the results reported in [57, 47, 174] but disputed by others [77, 154, 150]. Our model also indicates that the relationship between F_{RBC} and F_{blood} is relatively insensitive to R_n and H_n. Moreover, Figure 5.7 suggests that $F_{\text{RBC}} \approx F_{\text{blood}}$ for all cases which, combined with Eq. (5.19), implies that $H_{n,1}$ is within a few percent of H_n (see also Figures 5.5 and 5.6). However, the analysis in the section below demonstrates that these small differences in hematocrit cannot be neglected since they accumulate from one generation of vessels to the next, resulting in large intra-vessel variability of hematocrit in terminal sections of the vascular network.
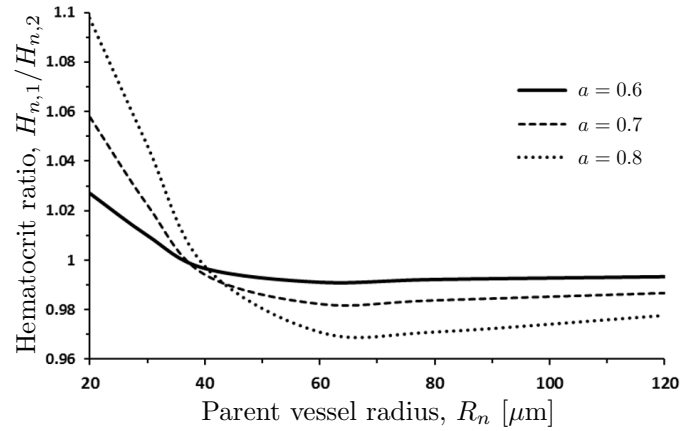
Figure 5.6: Ratio $H_{n,1}/H_{n,2}$ of the hematocrits the two daughter vessels as a function of the parent vessel radius R_n for several values of the bifurcation parameter a and hematocrit $H_n = 0.45$. Bifurcations of large vessels $(R_n > 200 \ \mu\text{m})$ preserves the hematocrit H_n, i.e., $H_n = H_{n,1} = H_{n,2}$.
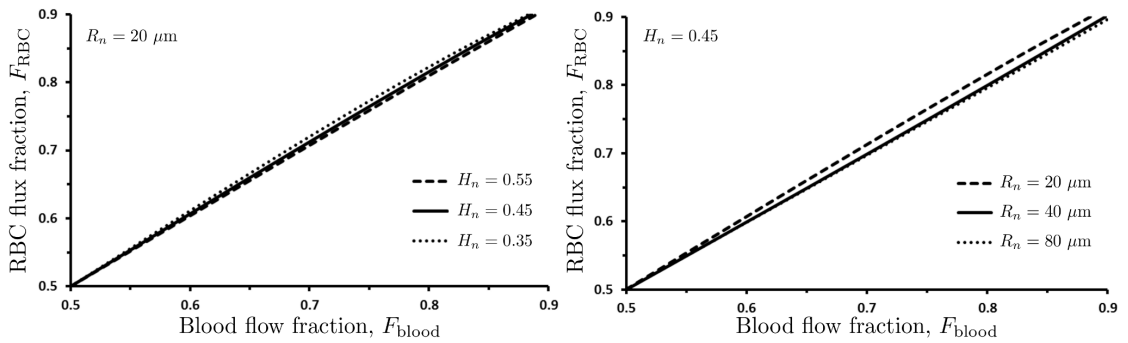
Figure 5.7: Dependence of the RBC flux fraction F_{RBC} on the blood flow fraction F_{blood} for several values of the parent vessel radius R_n and hematocrit H_n.

5.5 Results

5.5.1 Comparison with Murray's Law

The radii of the daughter vessels are but one metric by which to compare the vascular networks predicted with our model and that given by Murray's law; while the former requires one to solve a system of nonlinear Eqs. (5.14), (5.15), (5.17) and (5.18) in order to obtain these radii, the latter is given by a closed-form relation $R_n^3 = R_{n,1}^3 + R_{n,2}^3$. Other metrics include the distributions of pressure P and WSS τ throughout the vascular network.

According to our model, the WSS $\tau_n \equiv J_n R_n/2$ in an n-th generation vessel is computed from Eqs. (5.4) and (5.7) as

$$\tau_n = 2\,\pi^2\sqrt{\alpha}\,\frac{\mu(R_n, H_n)}{\Lambda(R_n, H_n)}. \tag{5.20}$$

Since $J \equiv \Delta P/L$, it follows from Eqs. (5.4), (5.7) and (5.18) that the pressure drop ΔP across a vessel of length L is given by $\Delta P = 4\kappa\pi^2\sqrt{\alpha}\,H\mu/\Lambda^2$. Let us suppose that a vascular network consists of N generations of vessels, and ends in the capillary bed where the blood pressure is P_{cap}. Then intraluminal pressure P_n at the start of an n-th generation vessel is

$$P_n = P_{\mathrm{cap}} + \sum_{i=0}^{n-1}\Delta P_{N-i}, \qquad \Delta P_m = 4\kappa\pi^2\sqrt{\alpha}\,\frac{H_m\mu(R_m, H_m)}{\Lambda(R_m, H_m)^2}. \tag{5.21}$$

A vascular network that obeys Murray's law has the constant length-to-radius ratio $\epsilon = L_n/R_n$ and the bifurcation relation $R_n^3 = R_{n,1}^3 + R_{n,2}^3$ for all $n \leq N$. Murray [129, 128] and subsequent studies [173] treat the viscosity of blood, μ^{M}, flowing through such a network as constant. Under these assumptions, Eqs. (5.4) and (5.7) predict the WSS τ^{M} that is constant throughout the vasculature,

$$\tau^{\mathrm{M}} = \pi^2\sqrt{\alpha\mu^{\mathrm{M}}}, \tag{5.22}$$

and the intraluminal pressure P_n^{M} in an n-th generation vessel that is given by

$$P_n^{\mathrm{M}} = P_{\mathrm{cap}} + 2\,n\,\pi^2\epsilon\,\sqrt{\alpha\mu^{\mathrm{M}}}(N - n + 1). \tag{5.23}$$

In the simulations reported in Figure 5.8, we consider a symmetrically bifurcating network ($a = 0.5$ or $R_{n,1} = R_{n,2}$ for all $n \leq N$) that consists of $N = 22$ generations,

terminating with capillaries of radius $R_N = 3$ μm. The capillary pressure is set to $P_{\text{cap}} = 30$ mmHg [33]. To facilitate the comparison between the two models, we chose the value of the constant blood viscosity μ^{M} in the Murray model to coincide with the asymptotic value of $\mu(R, H)$, which corresponds to large vessel radii. Setting $H = 0.45$ and $R = 1000$ μm this gives $\mu^{\text{M}} = 3.198$ cP.
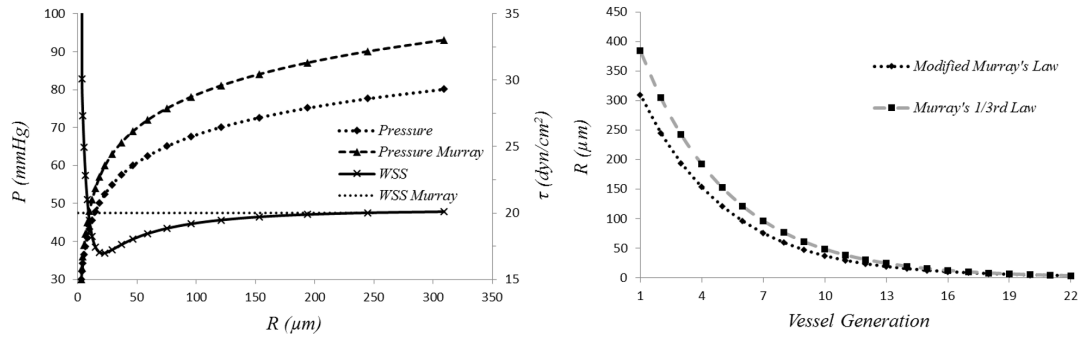
Figure 5.8: Distributions of (a) vessel radii R and (b) intraluminal pressure P and WSS τ predicted with our model and the model based on Murray's law.

The vessel radii of the vascular networks reconstructed with the two models are shown in Figure 5.8a. The difference between the two predictions exceeds 20% for the larger vessels (early generations of the network). The predicted distributions of the WSS τ (Figure 5.8b) highlight the physiological differences between the two models. While Murray's law implies a constant WSS τ^{M} across the entire network [145], our model captures the experimentally observed variability in the WSS τ between the vessels of different generations. Specifically, it predicts the amplification of the WSS in the microcirculation (vessel radii $R < 25$ μm), wherein the WSS appreciably increases as the vessel radii R become smaller (the vessel generation n becomes larger), reaching its maximum in the terminal, pre-capillary arterioles. This behavior is in agreement with the observed amplification of WSS in the microcirculation [107, 153, 86, 108]. In larger vessels ($R > 25$ μm), the WSS increases by a small amount with R, reaching a constant value in large arterioles. This is in general agreement with the observations reported in [184, 153].

Both models predict that the intraluminal blood pressure P increases with vessel

radius R, with the bulk of the pressure drop occurring in the smaller vessels (Figure 5.8b). As R approaches the values typical of large arterioles and small arteries, blood pressure in these vessels becomes almost equal to systemic arterial pressure. This indicates that the smaller arterioles contribute most to vascular resistance. These small vessels are often referred to as "resistance vessels". The predicted dependence of intraluminal pressure P on vessel radius R is in qualitative agreement with the observations [33, 107, 153].

5.5.2   Impact of branching asymmetry

The results presented in Figure 5.8 are obtained for a symmetric vascular network (the bifurcation parameter $a = 0.5$). Figure 5.9 demonstrates the effect of network asymmetry on the distributions of vessel radii and hematocrit throughout the networks with $a = 0.7$ and $a = 0.9$. The largest vessel in these simulations has radius $R_1 = 500$ μm and hematocrit $H_1 = 0.45$. Since each branch of the network terminates once the daughter vessel radius reaches $R = 3$ μm, the network asymmetry ($a \neq 0.5$) causes the number of vessels in each branch to vary. This implies that asymmetric vascular networks defy idealized fractal descriptions, which is in line with several in-vivo studies [134, 86, 92, 73, 148]. Only the first seven generations of the vessels (i.e., before any branch reaches the $R = 3$ μm threshold) are shown in Figure 5.9, with each circle representing a blood vessel with the radius R or hematocrit H at a given vessel generation n. Note that the number of bifurcating vessels in each generation increases as 2^{n-1}, which might not be apparent in Figure 5.9 since many of the data points overlap.

Our model predicts a large variability of hematocrit values across the vessels of the same generation (Figure 5.9), including at the terminal regions of the network and in the capillary beds supplied by these terminal branches. This finding is supported by the in-vivo measurements in capillary beds [92, 73, 148] that show large variations of observed hematocrit values across capillary beds, even among vessels of similar diameters. Our model accounts for this effect by allowing for the asymmetric partitioning of hematocrit at every bifurcating vessel.

A measure of the deviation a vascular network from its Murray's representation
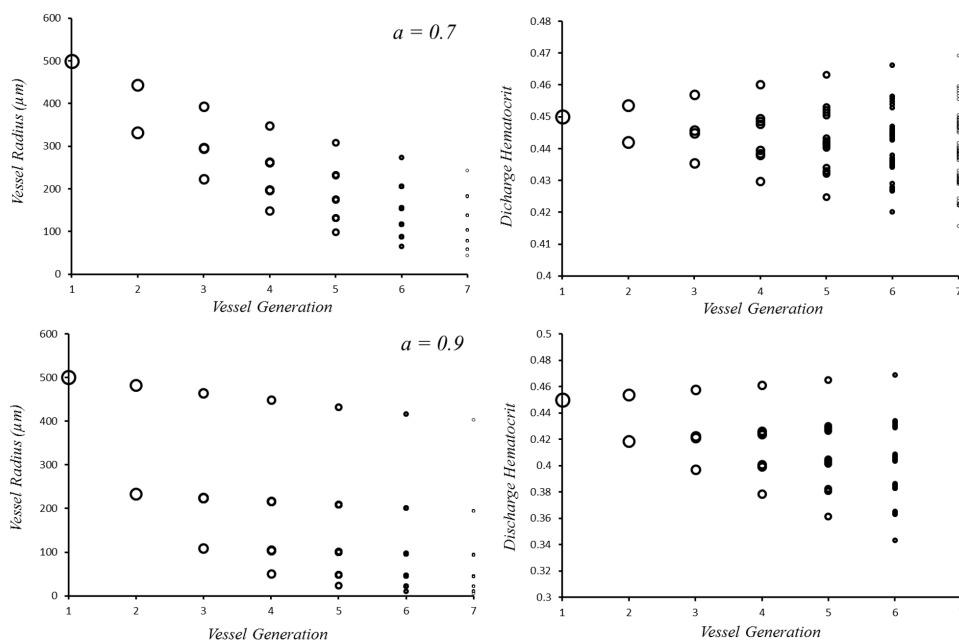
Figure 5.9: Variation of vessel radii R and discharge hematocrit H within the first $n = 7$ generations of asymmetric vascular networks with bifurcation parameters $a = 0.7$ and $a = 0.9$.

is provided by a network branching exponent ξ in

$$\sum_{i=1}^{2^n-1} R_i^{\xi} \approx \sum_{i=1}^{2^n-1} (R_{i,1}^{\xi} + R_{i,2}^{\xi}).$$ (5.24)

Murray's law states that the sum of powers of all the vessel radii in the n-th generation must equal the sum of powers of all the vessel radii in the $(n+1)$-th generation, and sets the power to $\xi = 3$. Reported values of ξ range from 2.7 to 3 [134, 40, 121, 166, 100, 93], which suggests small but meaningful deviations from Murray's law. For the networks presented in Figure 5.9, Eq. (5.24) holds across all generations with $\xi = 2.96$ for $a = 0.7$ and $\xi = 2.97$ for $a = 0.9$. These values are within 1% of the values reported in [121, 93].

5.5.3 Model validation

The vascular networks constructed with our model exhibit the following physiological characteristics observed in in-vivo studies.

a) The RBC flux fraction F_{RBC} at bifurcations varies approximately linear with the blood flow fraction F_{blood} over a broad range of hematocrits and vessel radii. This is in agreement with the data reported in [57, 47, 11, 174].

b) The asymmetry in discharge hematocrit at asymmetric bifurcations increases with the degree of asymmetry. This is in agreement with the data reported in [57, 77, 47].

c) The WSS is non-uniform in the microcirculation, significantly increasing in the terminal sections of the network. This is in agreement with the data reported in [107, 153, 86, 108, 145].

d) Pressure gradients increase sharply in the terminal sections of the network. This is in agreement with the data reported in [33, 107].

e) Bothe hematocrit partitioning at vessel bifurcations and hematocrit across the capillary bed in asymmetric networks is non-uniform. This is in agreement with the data reported in [92, 73, 148].

f) Predicted values of the branching exponent ξ fall within the range of their measured counterparts [121, 166, 100, 93].

5.5.4   Inverse modeling of vascular networks

The modeling framework described above treated the bifurcation parameter a as an input in order to construct a vascular network, e.g., to identify the ratio of the radii of daughter vessels $R_{n,1}/R_{n,2}$. A problem with such "forward modeling" is that the model parameter a, which determines the hematocrit partitioning at bifurcations, is harder to measure than the model output $R_{n,1}/R_{n,2}$, which is more readily measured in morphometric studies [40, 74, 86, 119, 121, 134]. The goal of "inverse modeling" is to infer the bifurcation parameter a from measurements of the parent vessel radius R_n, the ratio of the daughter vessel radii $R_{n,1}/R_{n,2}$ and the hematocrit H_n in the n-th parent vessel.
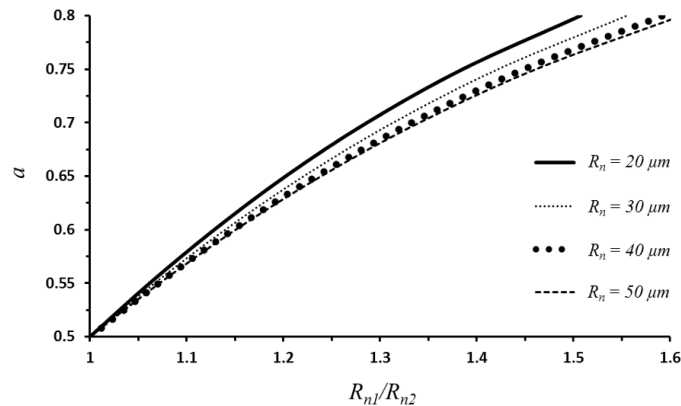
Figure 5.10: Variation of the bifurcation parameter a with the ratio of daughter vessel radii $R_{n,1}/R_{n,2}$ for several values of the parent vessel radius R_n.

This goal is facilitated by the one-to-one relationship between the bifurcation parameter a and the daughter vessel radii $R_{n,1}/R_{n,2}$, for any given value of R_n and H_n (Figure 5.10). This figure is constructed by running our forward model for multiple values of a, while keeping the values of R_n and H_n fixed. The four curves in Figure 5.10 correspond to $H_n = 0.45$ and four values of the parent vessel radius R_n. We found these curves to be essentially independent of H_n over a physiologically relevant range of its values. The dependence of a on the radii ratio $R_{n,1}/R_{n,2}$ in Figure 5.10 is fitted with a

second-degree polynomial

$$a = c_{a_2} \left(\frac{R_{n,1}}{R_{n,2}} \right)^2 + c_{a_1} \frac{R_{n,1}}{R_{n,2}} + c_{a_0}. \tag{5.25a}$$

The fitting coefficients c_{a_0}, c_{a_1} and c_{a_2} vary with the parent vessel radius R_n, such that

$$c_{a_0} = -0.58, \quad c_{a_1} = 1.43, \quad c_{a_2} = -0.36, \qquad \text{for } R_n > 50 \ \mu\text{m} \tag{5.25b}$$

and

$$c_{a_0} = -3.1 \cdot 10^{-4} R_n^2 + 0.03 R_n - 1.31, \quad c_{a_1} = 4.9 \cdot 10^{-4} R_n^2 - 0.05 R_n + 2.55,$$

$$c_{a_2} = -1.7 \cdot 10^{-4} R_n^2 + 0.02 R_n - 0.74, \qquad \text{for } R_n \le 50 \ \mu\text{m}. \tag{5.25c}$$

Figure 5.10 enables one to infer a value of the bifurcation parameter a from a measurement (or the average of multiple measurements) of the ratio of daughter vessel radii $R_{n,1}/R_{n,2}$. Then one can use our model to reconstruct the whole vascular network. Examples of such reconstructions are shown in Figure 5.11. Large degrees of asymmetry imply large spreads of discharge hematocrits and vessel radii across a given generation of vessels.

5.6   Discussion and Conclusions

We proposed a new approach for reconstruction of vascular networks. Our method follows the foundation premise of Murray's law in postulating the existence of functional optimality of such networks. The optimality criterion adopted in our approach is the physiological cost of supplying oxygen to the tissue surrounding a blood vessel. Bifurcation asymmetry is expressed in terms of the amount of oxygen consumption associated with the respective tissue volumes being supplied by each daughter vessel. Similar to [2], our approach accounts for the non-Newtonian behavior of blood by allowing the apparent blood viscosity to vary with discharge hematocrit and vessel radius in accordance with [155].

Our approach to network reconstruction offers significant advantages over Murray's law. Chief among them is its ability to capture the observed variability of WSS in the microcirculation. Our model predicts the sharp amplification of WSS in the
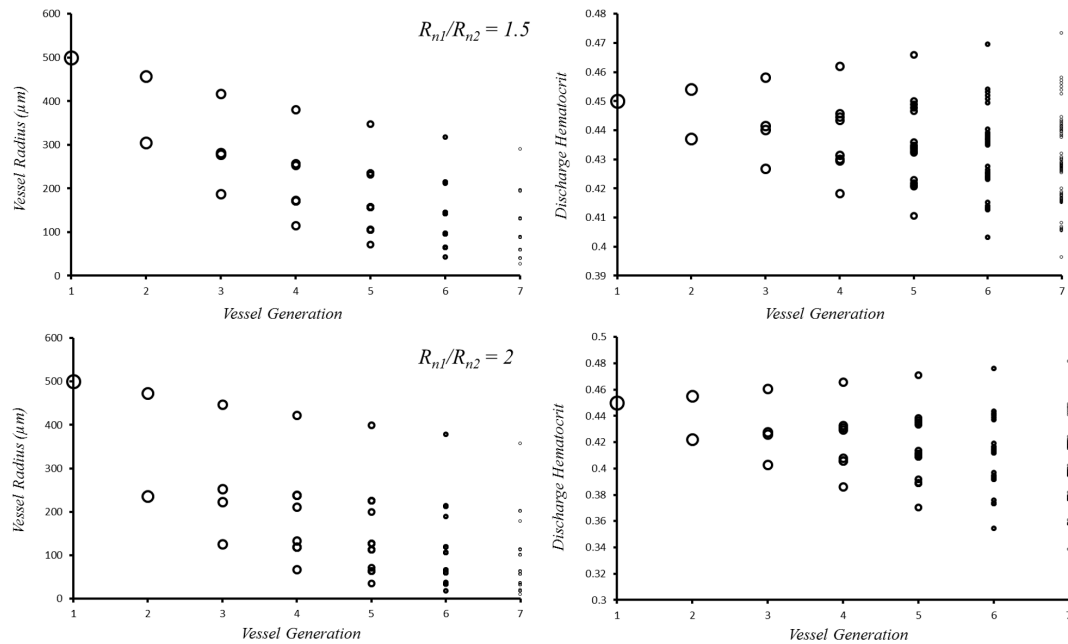
Figure 5.11: Variation of vessel radii and discharge hematocrit from one generation to the next for $R_{n1}/R_{n2} = 1.5$ (top panels) and $R_{n1}/R_{n2} = 2$ (bottom panels)

smallest vessels of a network ($R < 50\ \mu$m), which is consistent with in-vivo observations [153, 107, 86, 145]. WSS in intermediate vessels gradually increases with vessel radius, before reaching a constant value at large vessel radii ($R > 200\ \mu$m). This WSS variability is absent in networks reconstructed with Murray's law, which exhibit constant WSS throughout the vasculature.

The proposed approach captures both the asymmetric partitioning of hematocrit at vessel bifurcations and its effects on hematocrit variability in the terminal vessels of vascular networks. It provides theoretical support for the experimentally observed linear relationship between the RBC flux fraction and the blood flow fraction [57, 47, 174, 11], and for the in-vivo observations of pronounced variability of hematocrit in capillary beds [92, 73, 148].

Chapter 6

Modeling the Biochemial Reaction Cascade of Endothelial NO Production

6.1 Introduction

Endothelial cells produce Nitric Oxide (NO) on exposure to mechanical forces, such as hemodynamic shear stress and intraluminal pressure [8]. NO plays a crucial biological role in the vasculature, most importantly by stimulating relaxation of vascular smooth muscle [75] and hence the regulation of vascular resistance and blood pressure. NO also has various secondary roles in the vasculature such as elimination of free radicals [46] and prevention of plaque buildup [44]. NO production in endothelial cells occurs as a result of the oxidation of L-Arginine; a chemical reaction which results in the production of NO, catalyzed by the endothelial Nitric Oxide Synthase (eNOS) enzyme [8], [75] [158]. The mechanical stimulation of endothelial cells triggers a complex reaction cascade, involving multiple cellular mechanosensors and enzymes. The ultimate target of this complex and delicately fine tuned system is the activation of eNOS as a result of mechanical stimulation of the endothelium, thus increasing endothelial NO production.

Under basal, inactive conditions eNOS is stored in caveolae (small pouch-like invaginations along the EC cell membrane), bound to caveolin (Cav), which keeps eNOS

in an inactivated state. The eNOS enzyme is typically described in the literature as being calcium dependant [8], [16], [53], [84]; influxes of calcium ions into the cytosol activate eNOS by forming a calcium-calmodulin complex, which then binds with eNOS, liberating it from the inactive eNOS-Cav complex. The eNOS-Ca/CaM complex is stabilized by binding with Hsp90 (heat shock protein, 90kDa), which prevents eNOS from recombining with Cav and returning to its inactive state [8] [187]. Within this stable complex, eNOS is phosphorylated by various protein kinases (PKA, AKT, PKC, MAPK, PKG etc). The most prominent (and widely studied) sites for phosphorylation are the Serine-1197 and Threonine-495 amino acid residues (for human eNOS, for bovine eNOS the sites are Ser-1195 and Thr-497 respectively) [8], [16], [158], [127], [53]. Ser-1197 is primarily phosphorylated by AKT (with PKA and MAPK also contributing), while the Thr-495 residue is primarily a target for PKC (with AMPK and PKA also contributing) [16] [158] [127], [53]. The traditional view in the literature has been of a 'yin-yang' relationship between phosphorylation at Ser and Thr, with phosphorylation at Ser-1197 upregulating eNOS activity and phosphorylation at Thr-495 reducing eNOS activity. Phosphorylation at Thr-495 is believed to reduce eNOS activity by blocking the binding of eNOS with calmodulin [8], [88], [53], [127], [71], [120].

Once in a stable complex with CaM and Hsp90, eNOS then catalyzes the oxidation of L-Arginine (L-Arg) to L-Citruline (L-Cit), resulting in NO production. The NO thus produced diffuses out of the endothelial cell, into the blood stream (on the luminal side) and into the surrounding vascular smooth muscle [182]. NO in the blood stream is scavenged by RBCs, whereas NO diffusing to smooth muscle stimulates formation of cGMP (cyclic Guanosine monophosphate) and vasodilation. Within enothelial cells, the increased NO concentrations result in increased levels of cGMP formation, by combining with sGC (soluble guanylate cyclase) which then catalyzes the formation of cGMP from GTP (Guanosine tri-phosphate) [38] [142]. cGMP is observed to reduce the influx of calcium, thereby providing negative feedback to the system and limiting the rate of eNOS activation and NO production [99], [141], [37], a potentially vital limiting factor since NO is highly toxic at high concentrations.

The mechanosensitive triggers which serve to initiate this reaction cascade have been the subject of intense study in recent years [115], [28], [5], [176], [185], [36], [81].
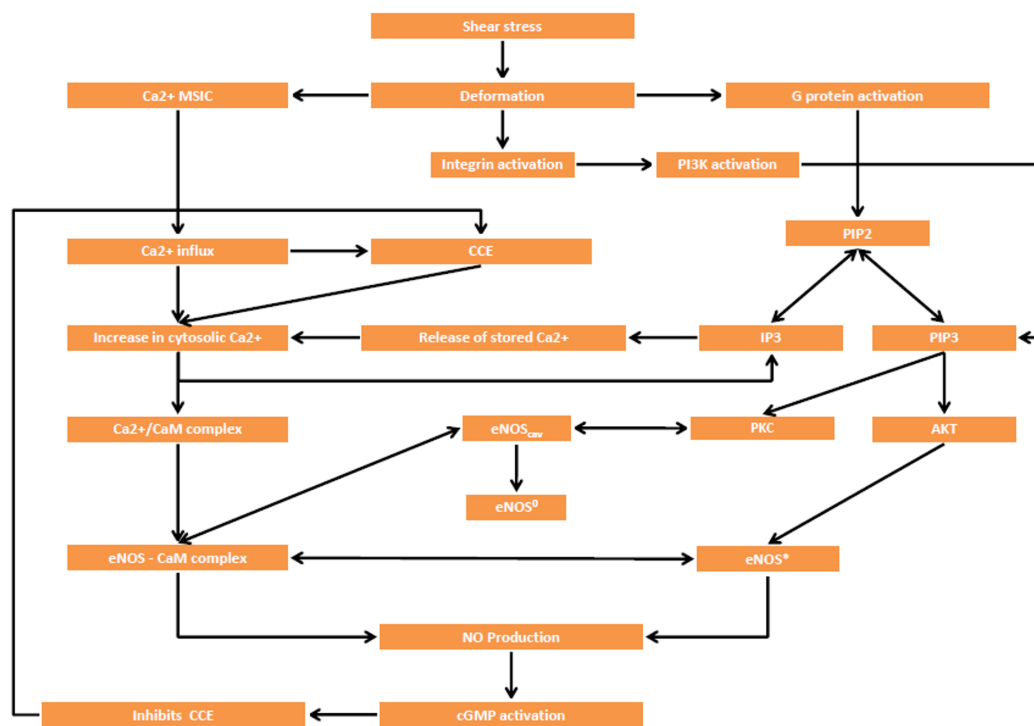
Figure 6.1: Reaction cascade for shear induced NO production

Deformation of the endothelial cell on exposure to shear stress (or other mechanical stimulation) activates eNOS (and hence NO production) first and foremost via the influx of calcium ions from extracellular fluid. This influx of calcium into the cytosol is mediated via the opening of mechano-sensing ion channels (MSICs) [115]. Calcium ions are also released from internal stores due to increased expression of IP3; this IP3 activation occurs due to increased activity of heterotrimeric G-proteins [104]. G-Proteins are activated by GPCRs (G-protein coupled receptors) which are mechanically coupled to the cell membrane and are activated following conformational changes following cell deformation [185] [28]. The increased activity of G-proteins is also coupled with the activation of protein kinases, such as AKT and PKC [127], [53], [16]. The activity of AKT and PKC is also modulated by the activation of PI3K [50], [51], [126] which is associated with a third major mechanosensor: integrins, anchoring ECs to the ECM. Stimulation of integrins results in tyrosine phosphorylation of FAKs (Focal adhesion Kinases), leading to activation of PI3K [88], [63], [126]. Hence, we have three major mechanosensors that we consider in this model: MSICs, GPCRs and integrins.

Mathematical modeling of the mechanically triggered reaction cascade in ECs is very useful for numerous reasons. First, a mathematical analysis of the existing conceptual model for NO production helps evaluate whether this model is in principle able to account for experimental data. A failure to replicate experimental observations would suggest gaps in our present understanding of how NO is produced in response to mechanical forces, as well as highlighting where such gaps may lie. Second, should our understanding of the process of mechanically stimulated endothelial NO production prove to be sound, mathematical analysis should help us develop a better understanding of the sensitivity of endothelial NO production to the various chemical species and mechanosensors present in endothelial cells. Such an understanding provides us with a guide for designing experiments that focus on the effects of inhibition of reactants and mechanosensors involved in NO production. Such experiments are especially important in fields of research such as cancer treatment [196], diabetes [42] and heart disease [44] where the regulation of endothelial NO production has significant clinical applications.

The majority of previous models of the endothelial response to mechanical stimulation have focused primarily on the influx of calcium ions into endothelial cells on

exposure to shear stress [142], [141], [37], [201], [200], [43]. The primary mechanosensors considered were mechano-sensing ion channels (MSICs), with the role of other potential mechanosensors such as integrins and GPCRs not considered. Further, the details of phosphorylation of eNOS and corresponding activation of protein kinases responsible for this phosphorylation were also largely absent in these previous models. A mathematical model that describes the biochemical reaction cascade starting with mechanosensing components and describing the coupled behavior of eNOS activation due to calcium signaling and phosphorylation by protein kinases has hence been lacking, up to this point.

In this study, we develop a mathematical model for the biochemical cascade that results in NO production in endothelial cells. The modeled cascade is triggered by mechanosensing components (MSICs, GPCRs and integrins) which stimulate calcium influx, G-protein activation and PI3K activation respectively, following the application of shear stress. The details of the mechanosensing machinery are not considered in the present study; instead calcium influx via MSICs, GPCR activation and PI3K activation are represented as functions of the applied shear stress, based on previous experimental and modeling studies. Following this initial stimulus, we then model the resulting calcium influx into the cell (both from internal storage as well as from the extracellular space), developing upon previous models in [142] [37] [104] to account for the contribution of G-protein activation as well as opening of MSICs due to shear stress. We then model the formation of calcium-CaM complexes, leading to the recruitment of eNOS into an eNOS-CaM complex.

Parallel to (and coupled with) these reactions, we also modeled the phosphorylation of AKT and PKC, which are stimulated by the activation of PI3K [171]. The phosphorylation of eNOS by these kinases was also modeled, with AKT increasing the activity of eNOS in the eNOS-CaM complex, while PKC reduced eNOS activity in our model by interfering with the formation of the active eNOS-CaM complex. The activated eNOS then produces NO, via the oxidation of L-Arg; we modeled this process using Michaelis-Menten kinetics [23]. The resulting NO thus produced leads to the production of cGMP, due to the activation of sGC by NO, leading to the conversion of GTP to cGMP. We used the analysis presented in [38], [204] to model the NO dependent cGMP production; increased cGMP was modeled as reducing calcium influx, based on the data

presented in [99], thereby providing negative feedback. The complete set of reactions was modeled as a system of coupled ODEs.

The reaction cascade described above was used to study both the steady and transient response of an endothelial cell to the step application of shear stress; allowing us to quantify how NO production is expected to vary with WSS. We compare our results with previous experimental results, to establish whether our predictions are in keeping with the reported behavior in the experimental literature. Further, we explore the effect of up or downregulating various components of the biochemical pathway, allowing is to determine the sensitivity of NO production to the up or down regulation of the individual reactants in the NO reaction pathway. We use this sensitivity analysis to further validate our model, by testing our predictions against corresponding experimental results.

6.2   Problem description:

We consider a layer of adherent endothelial cells, which are continuously supplied with the necessary metabolic substrates for maintaining NO production. Blood flows over the layer of endothelial cells (ECs), exerting shear stress τ on the surface of the cell layer. The exposure to shear stress triggers a cascade of chemical reactions resulting in endothelial NO production. Given a level of shear stress exerted on the EC layer by blood flow and under the assumption of a continuous supply of metabolic substrates, we model the entire reaction cascade that results in shear induced NO production. The reactions are assumed to occur in the cytosol, which is treated as being a well mixed continuum; hence, inhomogeneities and associated diffusive transport processes are neglected. The system is modeled as a set of deterministic ODEs.

6.3   Reaction Cascade:

GPCRs mechanically coupled to the cell membrane serve as force transducers, activating G-proteins, which in turn activate Phospholipase C (PLC), followed by Phosphatidylinositol 4,5-bisphosphate (PIP2) and Inositol triphosphate (IP3), ultimately trig-

gering the release of Calcium ions and the downstream activation of eNOS. The activation of GPCRs occurs as a result of conformational changes due to membrane deformation on exposure to external force; experimental data on GPCR and G-protein activation in endothelial cells has been quantified in numerous studies [185], [97], [79].

The rate of activation of G-proteins by GPCRs as a function of activated GPCR levels $[R^*]$ is given by [104], [162]:

$$\frac{\partial G}{\partial t} = k_a[R^*]\left([G_t] - [G]\right) - k_i\,[G] \tag{6.1}$$

The application of WSS causes conformational changes in GPCRs, resulting in the rapid activation of receptors followed by rapid deactivation (time scales on the order of 1 ns for both activation and deactivation) when mechanical stimulation is halted [28]. Due to this extremely rapid activation/deactivation, the kinetics of GPCR activation are not considered; $[R^*]$ is expressed as a function of shear stress τ alone, with the activation assumed to occur instantaneously. Based on experimental measurements for GPCR activation vs WSS [28], we fitted $[R^*]$ as:

$$[R^*] = tanh(\frac{\pi\tau}{\Lambda}) \tag{6.2}$$

where τ is in $dynes/cm^2$ and $\Lambda = 24\,dynes/cm^2$ (based on values in [28], figure 4d).

6.3.1   Calcium Signalling:

The activation of G-proteins then triggers the hydrolysis of PIP2 [104], to form IP3, which is responsible for the release of calcium from internal stores within the smooth endoplasmic reticulum (ER) [142]. The rate of IP3 production is dependent on cytosolic calcium concentrations, hence the stimulated calcium influx rapidly increases IP3 production, further increasing calcium release from internal stores in the ER further downstream. IP3 produced degrades to an intermediate phospholopid which is then converted back to PIP2, thus creating an IP3 - PIP2 cycle, which is regulated by G-protein activation and calcium concentrations. PIP2 is itself phosphorylated downstream to

produce PIP3; the concentrations of PIP2 are hence dependent on both IP3 and PIP3 production.

Balance of IP3 is given as [104], [142]:

$$r_h = \alpha \left(\frac{[Ca^{2+}]}{K_c + [Ca^{2+}]} \right) \frac{[G]}{[G_t]} \tag{6.3}$$

$$\frac{\partial [IP_3]}{\partial t} = r_h[PIP_2] - k_{deg}[IP_3] \tag{6.4}$$

PIP2 concentrations are then given as: $\frac{\partial [PIP_2]}{\partial t} = Consumption$ *due to IP3 production and replenishment + Consumption due to PIP3 production*, ie:

$$\frac{\partial [PIP_2]}{\partial t} = -(r_h + r_r)[PIP_2] - r_r[IP_3] + r_r[PIP_2]_{total} - k_{pip2}[PIP_2] + k_{-pip2}[PIP_3] \tag{6.5}$$

The first three terms on the RHS represent the rate of cycling of PIP2 to IP3, back to PIP2; the last two terms relate to the phosphorylation of PIP2 to PIP3, which subsequently participates in the activation of protein kinases downstream.

The increased IP3 concentration, as well as opening of MSICs due to WSS causes an increase in cytosolic calcium concentration. The opening of MSICs causes a sharp increase in the influx of calcium ions C_c from the extracellular fluid, while increased IP3 concentration causes stored calcium in the ER C_s to also be released into the cytosol. Further, the increase in C_c also causes in increase in capacitative calcium entry (CCE) from the extracellular fluid into the cytosol. The rate of CCE is reduced by increases in [cGMP]. The calcium balance in an endothelial cell in response to shear stress has been previously modeled in [142], [201], [37]; we utilize this previous work in our present study. The equations for concentration of cytosolic calcium C_c and stored calcium C_s are [37], [142]:

$$\frac{\partial C_c}{\partial t} = q_{rel} - q_{res} - q_{out} + q_{in} + K_{leak}C_s^2 - \frac{\partial [C_b]}{\partial t} \tag{6.6}$$

$$\frac{\partial C_s}{\partial t} = -V_r \left(q_{rel} - q_{res} - K_{leak}C_s^2 \right) \tag{6.7}$$

Here, q_{rel} represents calcium release from internal stores, q_{res} represents calcium re-sequestration into these internal stores, q_{out} is the rate of calcium efflux (via the sodium-calcium exchanger) [201] and q_{in} is the rate of calcium influx from extracellular fluid into the cell. C_{ex} is the calcium concentration in extracellular fluid and is assumed to remain constant. These calcium fluxes are described by the following equations:

$$q_{rel} = k_{rel} \left(\frac{[IP_3]}{K_2 + [IP_3]} \right)^3 C_s \tag{6.8}$$

$$q_{res} = k_{res} \left(\frac{C_c}{K_3 + C_c} \right)^2 \tag{6.9}$$

$$q_{out} = k_{out} \left(\frac{C_c}{K_5 + C_c} \right) \tag{6.10}$$

Influx of calcium ions into the cytosol q_{in} comes through capacitative calcium entry (CCE) [83] q_{CCE} as well as flux through MSIC's (q_{MSIC}) [37], [142]:

$$q_{in} = q_{CCE} + q_{MSIC} \tag{6.11}$$

MSICs trigger the initial stages of the reaction cascade by mediating the influx of calcium to the EC cytosol from the extracellular fluid (the blood stream). The rate of calcium influx via MSICs, q_{MSIC} is modeled as the product of the maximal rate of influx q_{max} and the proportion of ion channels open at a given WSS [201], [142], [37]:

$$q_{MSIC} = f_0(\tau) \, q_{max} = \frac{q_{max}}{1 + \alpha \, exp(-W(\tau))} \tag{6.12}$$

where the expression for $W(\tau)$ is given by [201], [142], [37]:

$$W(\tau) = W_0 \frac{\left(\tau + \sqrt{16\delta^2 + \tau^2} - 4\delta \right)^2}{\tau + \sqrt{16\delta^2 + \tau^2}} \tag{6.13}$$

Where the function $W(\tau)$ indicates the extent to which mechanical force applied is converted to gating energy for MSICs.

Capacitative calcium entry occurs as a result of the depletion of internal calcium stores, triggering influx of calcium from the extracellular fluid [83]. The rate of this capacitative entry is reduced by cGMP [99], [141], which thereby serves to limit the

amount of calcium entering the cytosol. Calcium flux due to CCE is given as [142], [141], [37]:

$$q_{CCE} = k_{CCE} \left(C_{s,0} - C_s\right) \left(C_{ex} - C_c\right) \psi([cGMP]) \tag{6.14}$$

$C_{s,0}$ is the stored calcium concentration (in internal stores in the ER) under basal conditions. $\psi([cGMP])$ represents the inhibition of CCE by increasing cGMP concentrations, as observed in [99]. The increased cGMP concentrations result from increased NO production, resulting in a negative feedback to the NO production cascade. ψ is expressed as:

$$\psi([cGMP]) = 1 - 0.01[cGMP] \tag{6.15}$$

By fitting with data from [99] for the inactivation of CCE as a function of cGMP concentration, expressed in μM. The relationship is linear at the concentrations (order 10 μM) of cGMP encountered in our model. At larger concentrations (order 1 mM), this relationship becomes non-linear and sigmoidal. cGMP also inhibits MSIC operation at high concentrations (1 mM and higher) [205], but at the lower concentrations typically encountered in ECs and smooth muscle [204], this effect is small. Hence, the inhibition of MSICs due to cGMP is neglected in this model.

The increased cytosolic calcium (C_c) combines with cytosolic proteins to form calcium complexes, resulting in the cytosolic proteins acting as a calcium buffer. The kinetics of Ca-Buffer formation, $[C_b]$ are given by [142], [76]:

$$\frac{\partial [C_b]}{\partial t} = -k_{off} \left([C_{btotal}] - [Ca_b]\right) + k_{on} C_c [C_b] \tag{6.16}$$

where $[C_{btotal}]$ is the total concentration of calcium binding sites in the buffered proteins.

Calcium activates eNOS by forming a complex with Calmodulin, which then recruits eNOS into an eNOS-CaM complex, with the rate of recruitment enhanced in the presence of Hsp90. Of the various Calcium-CaM complexes, only Ca3CaM and Ca4CaM appear to actively recruit eNOS, with Ca4CaM being the dominant species both in terms of cytosolic concentration [136] and affinity for eNOS [123]. Hence, we consider only the

role of Ca4CaM in the recruitment of eNOS. The concentration of free Ca4CaM in the cytosol may be expressed using a Hill function, that relates Ca4CaM concentration to cytosolic calcium concentration C_c [140], [146]. Based on data from [140] the expression for Ca4CaM concentration is modeled as:

$$\frac{\partial [Ca4CaM]}{\partial t} = K_{Ca4CaM}(\frac{C_c^{nc}}{K_{dc} + C_c^{nc}}\theta[CaM_{total}] - [Ca4CaM]) \qquad (6.17)$$

6.3.2   AKT and PKC balance equations:

The protein kinases AKT and PKC (which phopsphorylate eNOS) are themselves activated via phosphorylation mediated by PIP3 [171]. PIP3 is in turn formed by phosphorylation of PIP2, a reaction which is catalyzed by activated PI3K ($PI3K^*$) [126]. The activation of PI3K occurs as the result of integrin activation due to mechanical stimulation. This is shown graphically in figure 6.2. The total concentration of phosphorylated plus unphosphorylated AKT and PKC remains constant.

Integrins, which serve to anchor the endothelial cells in place (to the extracellular matrix or ECM) are connected to focal adhesion sites within the endothelial cell, whereby the application of mechanical force results in the tyrosine phosphorylation of Focal Adhesion Kinases (FAKs), ultimately triggering the stimulation of Phosphoinositide 3-kinase (PI3K), and further down the reaction cascade, protein kinases which phosphorylate eNOS - thereby modifying eNOS activity. This process has been studied experimentally, with the activation of intergins, FAKs and PI3K all measured as functions of mechanical stimulation [63], [88], [126] in endothelial cells in vitro.

The proportions of total activated (phosphorylated) AKT and PKC and concentrations of PIP3 are calculated as [171]:

$$\frac{\partial [PIP_3]}{\partial t} = k_{pip2}[PIP_2] - k_{-pip2}[PIP_3] \qquad (6.18)$$

$$\frac{\partial [AKT]}{\partial t} = k_{-akt}[AKT^*] - k_{akt}[AKT] \qquad (6.19)$$
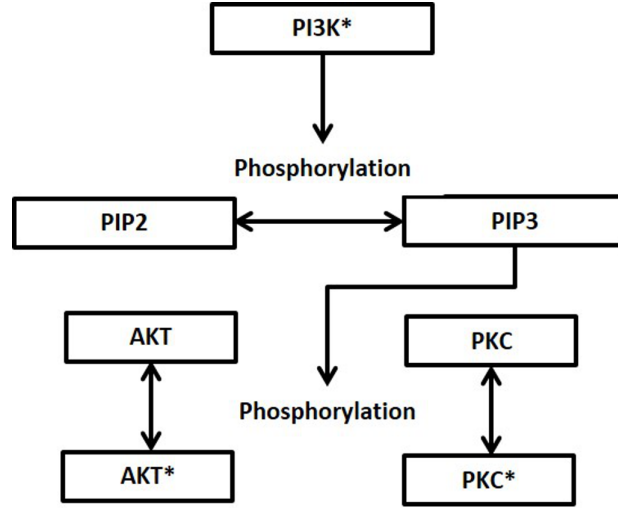
Figure 6.2: Activation of AKT and PKC

$$[AKT] + [AKT^*] = [AKT_{total}] = 1 \tag{6.20}$$

$$\frac{\partial[PKC^*]}{\partial t} = k_{pkc}[PKC] - k_{-pkc}[PKC^*] \tag{6.21}$$

$$[PKC] + [PKC^*] = [PKC_{total}] = 1 \tag{6.22}$$

On exposure to shear stress, PI3K is phosphorylated extremely rapidly (reaching maximal activation on the order of 10 seconds, [105], [63]), due to the activation of the FAK/Src complex through [65] integrins which serve as force transducers that mediate the mechanical signal. Due to the rapidity of this process relative to the other chemical reactions in our model (which generally occur at time scales of order 1-10 minutes), we neglect the time lag between application of mechanical force and PI3K activation; application of force thus results in immediate activation of PI3K in our model. The active PI3K species, $PI3K^*$ then gradually dissociates over time, back to basal levels of activity. The activation of PI3K above basal levels $[PI3K^*]$ was therefore modeled as:

$$\frac{[PI3K^*]}{[PI3K^*]_{basal}} = 1 + a_{pi3k}e^{-\eta t}tanh(\frac{\pi \tau}{\delta}) \tag{6.23}$$

Where the constants a_{pi3k} δ and η were fitted to experimental data in [63], [88]. The magnitude of PI3K activation depends on the magnitude of integrin activation, which in turn is dependent on the magnitude of τ. We hence assumed a sigmoid relationship between τ and PI3K activation and examined how variation of the parameter δ (which governs the shear stress τ at which maximal activation occurs) impacts our model predictions.

Data for transient PI3K activation due to mechanical stimulation in [63] suggests fairly short time scales (of order 5 minutes) for the decay of active PI3K back to basal levels, while the results presented in [88] cited large time scales (of order 30 minutes). We therefore considered a range of different alternatives for η in following sections; large values of η corresponding to rapid decay timescales, smaller values that correspond to larger timescales and $\eta = 0$, i.e. no decay.

Increased PI3K activation increases the rate of PIP2 phosphorylation to PIP3 [171]:

$$k_{pip2} = k_{1p}\frac{[PI3K]^*}{[PI3K^*]_{max}} + k_{2p} = \frac{k_{1p}}{(1 + a_{pi3k})} + k_{2p} \tag{6.24}$$

The rate of PKC and AKT phosphorylation increases with increasing concentrations of PIP3 as [171]:

$$k_{akt} = 0.1k_{-akt}([PIP_3] - 0.31)/(3.10 - 0.31)min^{-1} \tag{6.25}$$

$$k_{pkc} = 0.1k_{-pkc}([PIP_3] - 0.31)/(3.10 - 0.31)min^{-1} \tag{6.26}$$

where k_{-akt}, k_{1p}, k_{2p}, and k_{-pkc} are all constants [171].

Hence, the activation of PI3K by application of WSS causes an increase in AKT and PKC activity via phosphorylation. This increased PI3K activity is somewhat offset by the increased hydrolysis of PIP2 to IP3 (due to the activation of GPCRs), reducing the amount of PIP2 available for phosphorylation to PIP3, which is responsible for the activation of AKT and PKC. Hence, G-proteins stimulate eNOS activation by triggering the release of calcium into the cytosol and by reducing the available active PKC (which reduces eNOS activity), but this is somewhat offset by decreased levels of active AKT.

6.3.3 eNOS complex formation and phosphorylation:

The Ca4CaM complex then forms a complex with eNOS, removing eNOS from its bound, inactive state with Caveolin (Cav) [8]. The presence of Hsp90 helps greatly increase the rate of eNOS - CaM binding ([187]); the eNOS-CaM complex is then a target for eNOS phosphorylation at Ser1197, catalyzed by AKT [16], [127], [8], [53], [187]. While still bound to Cav (and therefore prior to the formation of the complex with CaM), eNOS is also a target for phosphorylation at Thr-495, which prevents eNOS binding with CaM. eNOS thus phosphorylated by PKC remains inactive, thereby accounting for the inhibitory effect of PKC. Figure 6.3 shows a graphical representation of this series of reactions.
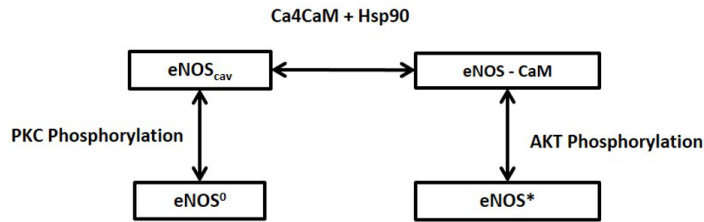
Figure 6.3: Reactions involving eNOS

eNOS phosphorylation by PKC, is assumed to follow first order kinetics, with the forward rate constant estimated from data in [22]. The dephosphorylation is mediated by various phosphatases, such as PP2A [8], [64]. At present, little information is available on the activation of phosphatases such as PP2A and calcineurin on application of shear stress. As a result, the rate of dephosphorylation was assumed constant.

$$\frac{\partial\left[eNOS^0_{cav}\right]}{\partial t} = k_{thr}[eNOS_{cav}]\frac{[PKC^*]}{[PKC^*]_{max}} - k_{-thr}[eNOS^0_{cav}] \qquad (6.27)$$

The rate of formation of the eNOS-CaM complex was modeled using Michelis-Menten kinetics; rate constants were obtained from data presented in [125], [123], [84]. The formation of eNOS - CaM is mediated by Hsp90 [8], [187]; we assume that since Hsp90 is present in large excesses over other reactants (eNOS and CaM), the rate of eNOS - CaM formation is insensitive to fluctuations in Hsp90 activation and is hence maximized with regard to the stimulatory effect of Hsp90. The resulting complex is

further stabilized by phosphorylation due to AKT; the resulting complex (denoted as $eNOS^*_{cam}$) is not only stable, but is also significantly more active in stimulating NO production due to the catalysis of the L-Arg oxidation reaction [16], [127], [8], [53], [187]. The activation of eNOS in its basal, inactive state to its fully active, Ser-1197 phophorylated state is therefore modeled as a 3 step process;

Step 1: The formation of the eNOS-CaM complex, mediated by Hsp90

Step 2: The formation of the AKT phosphorylated eNOS-CaM complex

Inhibitory Step: eNOS phosphorylation by PKC at thr-495, blocking CaM binding and rendering eNOS inactive and preventing steps 1 and 2 above.

The rate of eNOS binding to CaM is expressed as:

$$\frac{\partial \left[eNOS_{cam}\right]}{\partial t} = \frac{K_{cam}[Ca4CaM]}{K_{0.5cam} + [Ca4CaM]}[eNOS_{cav}] - K_{-cam}[eNOS_{cam}] - \frac{\partial}{\partial t}\left([eNOS^*_{cam}]\right)$$
(6.28)

The eNOS-CaM complex thus formed is then phosphotylated by AKT; we modeled this reaction as following first order kinetics:

$$\frac{\partial[eNOS^*_{cam}]}{\partial t} = k_{eakt}[eNOS_{cam}] - k_{-eakt}[eNOS^*_{cam}]$$
(6.29)

with

$$k_{eakt} = k_{maxakt}\frac{[AKT^*]}{[AKT^*]_{max}}$$
(6.30)

Rate constants were estimated using data presented in [187] (refer appendix E).

The total amount of eNOS in different complexes is conserved:

$$[eNOS_{cav}] + [eNOS^0_{cav}] + [eNOS_{cam}] + [eNOS^*_{cam}] = [eNOS_{total}]$$
(6.31)

Where $eNOS_{cav}$ is eNOS bound to caveolin; $eNOS^0_{cav}$ is eNOS bound to caveolin, phosphorylated at thr495 (and hence rendered inactive); $eNOS_{cam}$ is eNOS bound to calmodulin and $eNOS^*_{cam}$ is the eNOS-CaM complex, phosphorylated at Ser1197 by AKT.

NO concentration equations:

eNOS in complex with CaM now catalyzes the oxidation of L-Arg, resulting in the production of NO. Within this complex, eNOS phosphorylated at Ser1197 is approximately 9 times as active [187] as eNOS in the unphosphorylated CaM bound state. The production of NO is modeled using Michaelis-Menten kinetics [23], with the supply of O2 assumed constant. The NO thus produced is then consumed by two separate sinks; NO combines with sGC within the enodthelial cell to produce sGC-NO, which cataylzes the production of cGMP from GTP [38], [204]. In addition, NO is also metabolized rapidly by RBCs immediately adjacent to the ECs [182].

The equation for NO concentration is given by:

$$\frac{\partial [NO]}{\partial t} = Q_{NO} - Q_{sgc} - \lambda_{NO}[NO] \tag{6.32}$$

Where Q_{NO} is the rate of production of NO, Q_{sgc} is the rate of NO scavenged by SGC and λ_{NO} is the rate at which NO is metabolized. The production of NO, as a result of oxidation of L-Arg (Q_{NO}), is given by:

$$Q_{NO} = R_{NO}\frac{[O_2]}{K_{mNO} + [O_2]} \tag{6.33}$$

The maximal rate of NO production (R_{NO}) depends on the concentration of both phosphorylated and unphosphorylated eNOS - CaM:

$$R_{NO} = K_{NOe}\left\{[eNOS_c] + \Phi[eNOS_c]^*\right\} \tag{6.34}$$

where Φ indicates the extent to which AKT phosphorylation increases eNOS activity, in the presence of Hsp90. Assuming a constant supply of L-arg, K_{NOe} remains constant.

The consumption of NO by sGC is given by [38]:

$$Q_{sgc} = R_{NOmax}[SGC_0]\left([NO] + B_{NO}[NO]\right)\left(A_0 + A_1[NO] + [NO]^2\right)^{-1} \tag{6.35}$$

Where B_{NO}, A_0, A_1 and R_{NOmax} are constants.

The NO consumed by SGC, leads to an activation of SGC, thereby stimulating the conversion of GTP to cGMP. The rate of cGMP production can then be expressed as a function of NO concentration as [38]:

$$\frac{\partial [cGMP]}{\partial t} = R_{cGMPmax}[SGC_0]\frac{\gamma_1 + \gamma_2[NO] + [NO]^2}{A_0 + A_1[NO] + [NO]^2} - \frac{V_{dg}[cGMP]^2}{K_{mdg} + [cGMP]} \quad (6.36)$$

This increase in cGMP concentration then serves as a negative feedback, by reducing CCE into the cell (equation 6.14).

6.4   Initial Conditions

The basal, resting condition for the model endothelial cells in this study is defined as the steady-state concentrations of all reactants at zero shear stress. The initial concentrations used were as follows:

[IP3]: 0 nM (due to zero activation of the GPCR-PIP2-IP3 cycle in the absence of mechanical stimulus) [142], [201]

[PIP2]: Calculated as 9.87 μM

C_c: 0.1 μM [142], [201]

C_s: 2830 μM [142], [201]. At zero IP3 concentrations, the ER maintains a large reserve of stored calcium. At steady-state, with no shear stress applied, C_s must of course remain constant and equal to the initial value. Further, following small perturbations of the system from the initial state, the stored calcium concentrations must return to their basal values in a finite amount of time for the initial condition specified to be viable. This however, only occurs if the leak current $K_{leak}C_s^2$ in equation 6.6 is included in the expressions for calcium balance within the cell. Several studies that built on the initial work of [142], [201] neglected this leak current [141], [37], [43] in their expressions for calcium balance. This results in an unstable initial condition that the system never returns to, even after the removal of stimulus. Hence, we argue that the leak current for stored calcium must be present in the equations for calcium concentration.

[$Ca4CaM$]: Calculated as 0.0198 μM at the of initial cytosolic calcium concentration, $C_c = 0.1\mu M$.

$[eNOS_{cav}]$: Calculated as 0.7074 μM

[PIP3]: Calculated as 0.13 μM

AKT^*: Calculated as 0.03375 or 3.375 % of total AKT

PKC^*: Calculated as 0.03375 or 3.375 % of total PKC

[eNOS - CaM]: Calculated as 0.0485 μM

$[eNOS^*]$: Calculated as 0.0294 μM

[cGMP]: Calculated as 1.254 μM

[NO]: Calculated as 0.0086 μM

$[eNOS_0]$: Calculated as 0.21 μM

These calculated initial conditions imply that over 90 % of eNOS is initially bound to caveolin (with 21 % phosphorylated at Thr - 495 by PKC), consistent with the proportion of inactive eNOS reported in [84]. Further, even at basal conditions, there is a finite and detectable degree of NO production and AKT phosphorylated eNOS. This is consistent with the conclusions in [135] where even at basal conditions and no shear stress, a measurable degree of eNOS activity is maintained.

6.5 Results

We focus our attention on step increases of shear stress from a basal condition corresponding to $\tau = 0$ to various steady, non-zero values of τ; upon excitation from these basal conditions we explore the behavior of our modeled reaction cascade. Figure 6.4 shows our calculated variation of NO concentrations with time, for a shear stress $= 12$ $dynes/cm^2$, for different values of the parameters η and δ. Smaller values of η correspond to a sigmoid type of behavior, while larger values result in a peak in NO concentrations, followed by a sharp decrease as PI3K activity gradually decays back to basal levels. Experimental measurements of NO concentrations are more in keeping with the sigmoid behavior [96], [6]; hence, for all further results, we use $\eta = 0.003$, which is in line with the time scales for decay of PI3K activity observed in [63]. For this value of η, our model is relatively insensitive to the value of δ, as shown in figure 6.4 b.

We use a value of $\delta = 24 dynes/cm^2$ (analogous with equation 6.2), however any value in this vicinity will yield similar results. This implies that when examining

the evolution of NO concentrations over large time periods following exposure to a step increase in shear stress, the enhanced activation of AKT and PKC is likely not important, due to the rapid return of PI3K to basal levels of excitation. AKT and PKC do still play a crucial role in eNOS regulation as discussed in the results below.
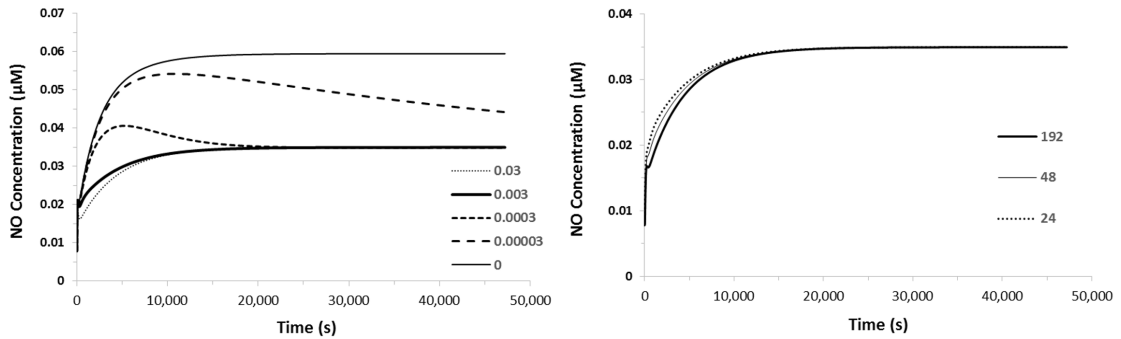
Figure 6.4: Variation of NO concentrations over time at 12 $dynes/cm^2$ for a) $\delta = 24 dynes/cm^2$ and different values of η and b) $\eta = 0.003s^{-1}$ and different values of δ

Figure 6.5 shows the transient variation of cytosolic calcium C_c, Stored Calcium C_s, Calcium calmodulin complex Ca4CaM and the eNOS - CaM complex at different levels of shear. The endothelium is treated as initially being at equilibrium at zero shear stress and is then exposed to a steady, constant shear stress. This step increase in τ results in rapid discharging of internal calcium stores within the cell as calcium rapidly enters the cytosolic volume. This results in a rapid spike in calcium levels, followed by a more gradual decline to a steady state value of C_c which is none the less greater than in the absence of any shear stress at all. This behavior has been reported in numerous previous studies [201], [37], [142], [70], [5]. The steady state calcium concentration increases with τ, due to the role of the MSICs and G-proteins.

The spike in calcium concentrations causes a corresponding increase in Ca4CaM, leading to the formation of eNOS - CaM. This results in the calcium dependent part of the eNOS activation cascade; the spike in calcium concentrations causes a spike in eNOS bound to CaM, which then undergoes phosphorylation by AKT further downstream, maximizing eNOS activity. The transients for this initial stage of the reaction cascade occur very rapidly (on the order of 100 s); the subsequent kinase dependent portion of

the eNOS activation cascade proceeds at a more gradual pace.
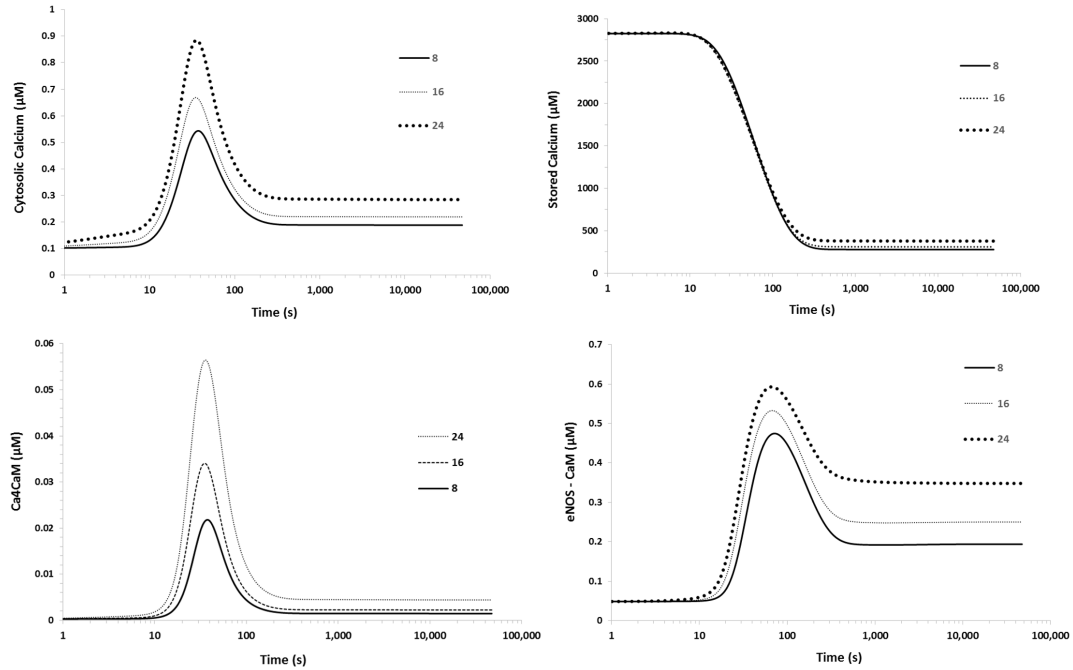
Figure 6.5: Variation of Stored Calcium C_s, Cytosolic Calcium C_c, Ca4CaM and eNOS - CaM over time at 3 different levels of shear stress: 8, 16 and 24 $dynes/cm^2$

Figure 6.6 shows the ensuing AKT phosphorylation of eNOS (forming $eNOS^*$), once eNOS has formed a complex with CaM. The increased concentrations of $eNOS^*$ form gradually, over longer time scales than the initial calcium transients. eNOS bound to caveolin (and hence inactivated) rapidly decreases following the initial calcium influx, before reaching a steady state. The extent of depletion of eNOS - Cav increases with τ, as do the increased concentrations of $eNOS^*$. The resulting NO concentrations due to this shear induced NO production display a bimodal nature over time; an initial peak that corresponds to activation by calcium, followed by a second, prolonged peak due to the role of protein kinases in eNOS activation. Hence, we get a calcium dependent and then a calcium independent phase of eNOS activation. This is in agreement with the current literature [8], [127], [16] which suggests that the activation of the eNOS enzyme has a dual nature: partly calcium dependent and partly AKT dependent. Also shown in figure 6.6, cGMP concentrations increase with NO concentrations; thereby facilitating
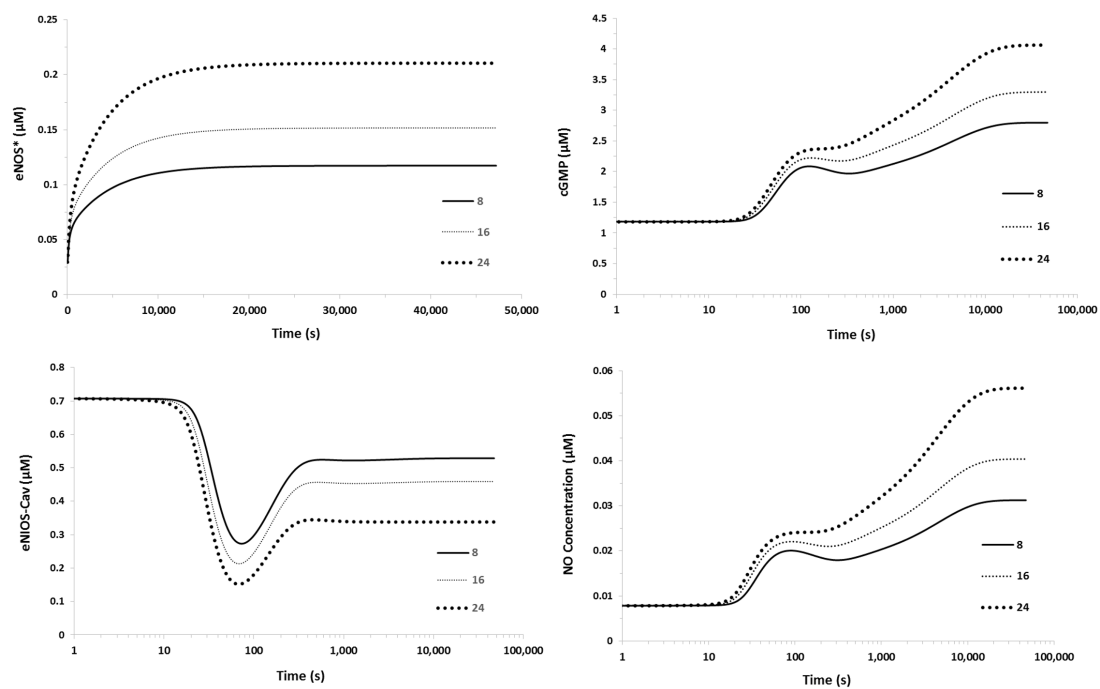
Figure 6.6: Variation of AKT Phosphorylated eNOS [$eNOS^*$], Caveolin Bound eNOS [$eNOS_{cav}$] and NO and cGMP concentrations over time at 3 different levels of shear stress: 8, 16 and 24 $dynes/cm^2$

the vasodilatory role of NO in the physiology.

To compare the different time scales of the various components of the eNOS activation process, figure 6.7 shows the transient variation in C_c, [Ca4CaM], $[eNOS_{CaM}]$, $[eNOS_{Cav}]$, $[eNOS^*]$ and [NO] for $\tau = 12dynes/cm^2$. The calcium dependent and kinase dependent portions of the eNOS activation cycle can be readily seen, with the calcium dependent activation occurring very rapidly.
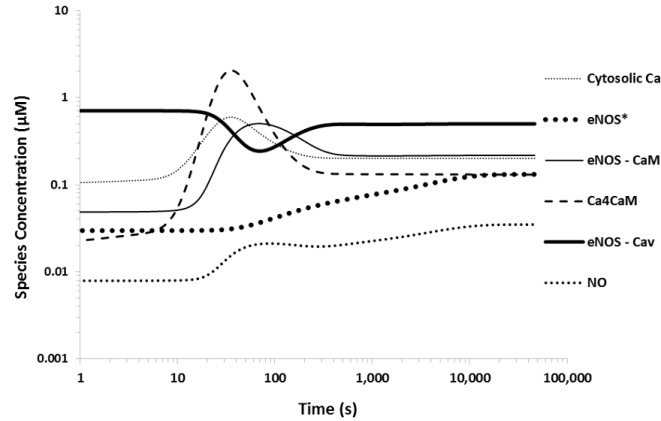
Figure 6.7: Variation of C_c, [Ca4CaM], $[eNOS_{CaM}]$, $[eNOS_{Cav}]$, $[eNOS^*]$ and [NO] over time, for $\tau = 12dynes/cm^2$

Comparison with Experiment

In order to verify whether our model predicts realistic values of NO production as well as a realistic transient behavior, we compared our model predictions with a number of data points from the experimental literature. Figure 6.8 shows the variation of the rate of NO production at steady state vs shear stress τ in our model and a number of experimental data points. Our predicted variation reproduces the general trend represented in the data; while considerable scatter exists in the available data, our model appears to make realistic predictions for NO production rates at steady state that are at least broadly speaking, in agreement with the available experimental data.

Figure 6.9 shows the transient behavior of our predicted NO production rate at shear stress $\tau = 1.8dynes/cm^2$ vs experimental measurements reported in [96]. NO production reaches a steady state in around five hours, with the bulk of the transient increase occurring within one hour (an observation also in agreement with data in [98]).
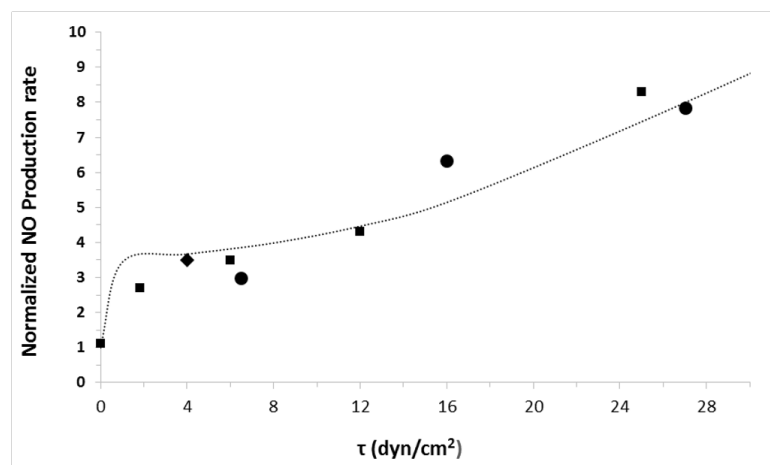
Figure 6.8: Variation of the normalized steady state NO production rate for different values of τ (in $dynes/cm^2$). The solid line is our model prediction. Solid squares: [96]; Solid circles: [122]; Solid diamond: [89]

Figure 6.9: Variation of the NO production rate (normalized with respect to the steady state value) with time for $\tau = 1.8 dynes/cm^2$. The line is our model prediction. Solid squares: [96]

Figure 6.10 shows our predictions for the rise above basal levels in AKT Phosphorylated eNOS ($eNOS^*$) and cGMP 1 hour after the initiation of shear stress. Also shown are corresponding experimental measurements from data published in [51]. Our predictions are in reasonably close agreement (within 10 %) with the measured increase of both $eNOS^*$ and [cGMP]. Hence, our model is able to account for the role eNOS plays in elevating cGMP levels, which is the primary downstream role of NO and results in the dilation of vascular smooth muscle.
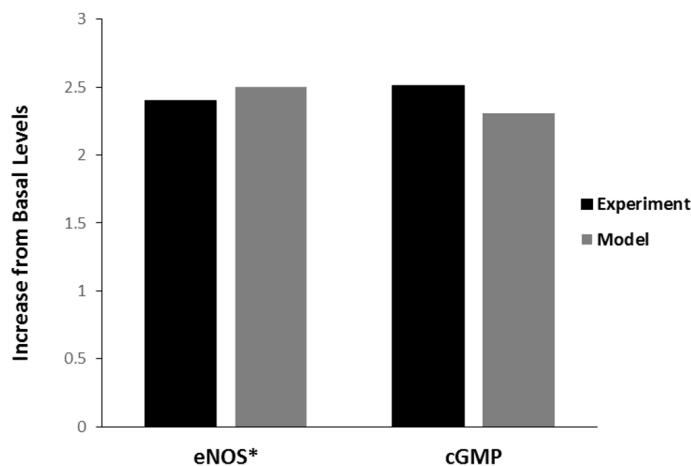
Figure 6.10: Model vs Experimental increase from baseline for AKT phosphorylated eNOS (at $\tau = 12 dynes/cm^2$) and cGMP concentration (at $\tau = 15 dynes/cm^2$) 1 hour after initiation of shear stress. Experimental data is from [51]

Figure 6.11 shows our predicted values for the steady state NO concentration at 3 different levels of τ vs the measurements for the corresponding shear stress reported in [118]. Our predicted values are within 5 % of the experimental data for all 3 cases. Further, over the narrow interval of τ considered, the variation of [NO] with τ will be close to linear; this implies that while the dependence of NO on τ is non-linear in general, for small fluctuations in shear stress, the assumption of a linear relationship is well justified as was done in [181]. Further, figure 6.12 also shows that our predictions for the change of NO from baseline are within 10 % of data from [6].

We also tested the impact of inhibition of protein kinases on NO production, as a means of model validation. Typically, the role of protein kinases on eNOS activation
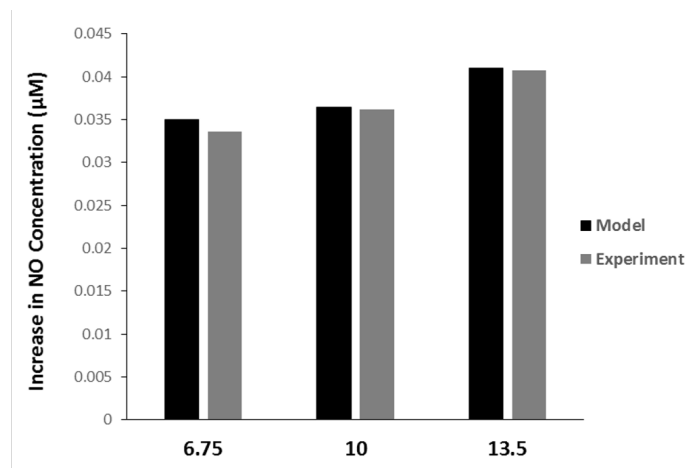
Figure 6.11: Model vs Experimental NO concentration at different shear stress levels (in $dynes/cm^2$). Experimental data is from [118]
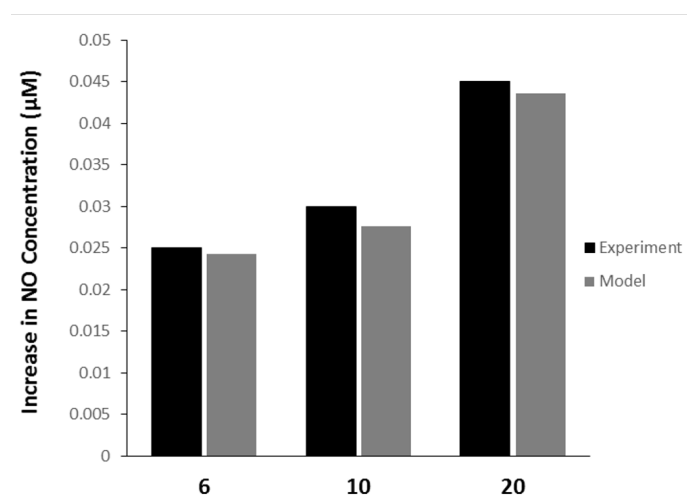
Figure 6.12: Model vs Experimental increase in NO concentration from basal levels at different shear stress levels (in $dynes/cm^2$). Experimental data is from [6]

is studied by inhibiting either the kinases individually, [120], [71] or inhibition of PI3K, which results in the subsequent inhibition of both AKT and PKC [50], [51]. We therefore modeled the impact of both PI3K inhibition and PKC inhibition on NO production rates and concentration. Figure 6.13 shows the impact of the complete inhibition of PI3K or PKC on our predictions for steady state NO production and concentration at $\tau = 12 dynes/cm^2$. Inhibition of PI3K results in a significant (73 %) reduction in NO production, while the inhibition of PKC alone results in a smaller, but still significant (18 %) *increase* in NO production. The predicted magnitude of reduction in eNOS activity and NO production with PI3K inhibition is in the vicinity of data presented in [60] (73 % predicted vs 68 % reported). This is in keeping with the general trend in the literature where PI3K inhibition results in decreased eNOS activity [51], [60] while PKC inhibition elevates eNOS activity [71]. Precise quantification of the extent of inhibition of kinases vs NO production over a range of shear stresses is unavailable in the literature, however the empirical behavior observed in the literature is none the less also found in our model.
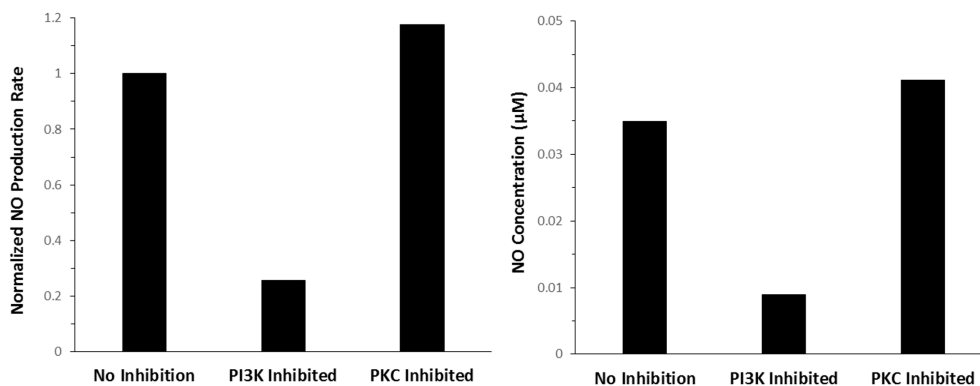
Figure 6.13: Impact of inhibition of protein kinases on NO production at shear stress $\tau = 12 dynes/cm^2$

The inhibition of PI3K results in the inhibition of both PKC (which reduces eNOS activity) and AKT (which increases eNOS activity), however the net effect of PI3K inhibition is the drastic reduction of eNOS activity. This implies that AKT activation of eNOS is significantly more important than inactivation by PKC phosphorylation; this reinforces the paradigm [8] that AKT is by far the most important protein kinase that

interacts with eNOS.

Transient behavior following the removal of shear stress:

We next examined the behavior of the system when shear stress is removed. Figure 6.14 shows the resulting transient variation of species concentrations from steady state at shear stress $\tau = 12 dynes/cm^2$ once the shear stress is removed. The resulting return to basal conditions resembles the activation of the reaction cascade on application of shear stress; the calcium transients lead the protein kinase dependent transients, with NO returning to basal concentrations and production levels after approximately 5 hours. The return of stored calcium concentrations in the ER and calcium concentrations to basal levels occurs in around 5 minutes. These time scales for return of reactants to basal concentrations is in broad agreement with the time scales oberved in experiments measuring calcium transients [5], [70] and NO production [118].
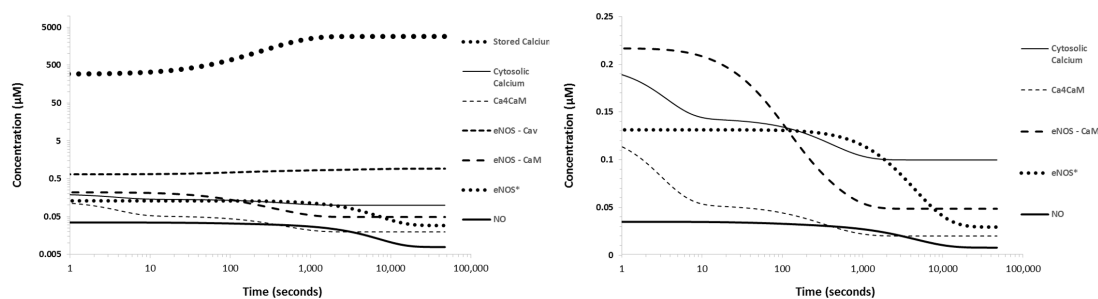
Figure 6.14: Transient behavior of reactants in the eNOS reaction cascade following the removal of shear stress $\tau = 12 dynes/cm^2$ once the system reached steady state at $\tau = 12 dynes/cm^2$.

Impact of feedback due to cGMP:

As given by equation 6.14, capacitative calcium entry (CCE) is inhibited by increased concentrations of cGMP, based on experimental data presented in [99]. At large (mM) concentrations of cGMP, CCE is completely inhibited, resulting in cytosolic calcium being strongly restricted by cGMP. The concentrations (of order 1 - 10 μM) of cGMP found in our model correspond to a much smaller degree of calcium inhibition. We hence examined whether the feedback role of cGMP was significant in our model. Figure 6.15 shows the difference in NO concentrations and eNOS - CaM concentrations

at two different levels of shear stress, with and without feedback. The results suggest that at the low concentrations of cGMP likely to be encountered in ECs, the feedback role of cGMP is fairly minor. Hence, the NO production rate may be treated as being essentially independent of cGMP concentrations and the negative feedback loop may be neglected.
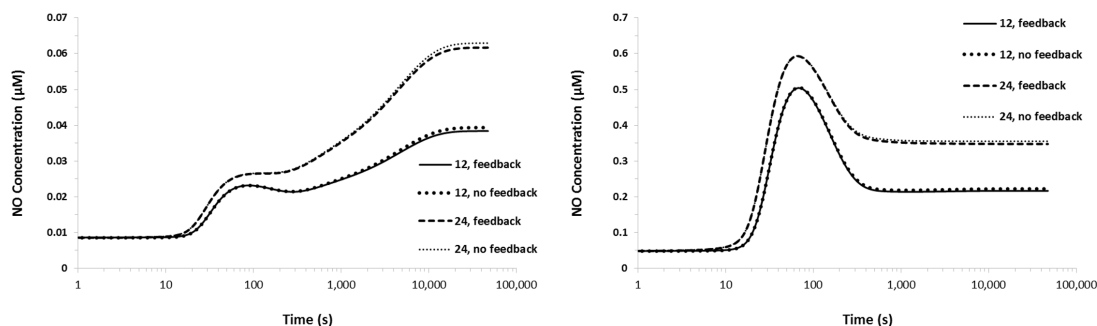
Figure 6.15: Transient variation of [NO] and [eNOS - CaM] with and without feedback at $\tau = 12 dynes/cm^2$ and $\tau = 24 dynes/cm^2$.

6.6 Discussion

In this study we constructed a biochemical model of the reaction cascade for the activation of eNOS in endothelial cells, when stimulated by shear stress. The three key mechanotransducers identified in ECs, namely MSICs, integrins and GPCRs are all included in our model. The reaction cascade can be thought of as consisting of two parts: a) the rapid activation of calcium which results in the formation of calmodulin complexes, followed by the recruitment of eNOS from caveolae and b) the phosphoryaltion of eNOS by PKC and AKT (which are both activated by PI3K), resulting in further activation of eNOS. The two parts of the constructed model are coupled, resulting in a highly non-linear transient behavior of NO production, following the application of shear stress. Our model also includes a negative feedback loop due to the inhibition of calcium influx into the cell by cGMP; increased NO levels cause a rise in cGMP levels, so cGMP inhibition of calcium influx serves to limit the extent of NO production in principle.

We applied this model reaction cascade to study the behavior of NO production

following exposure of ECs to a step increase of shear stress, with the shear stress being maintained at a steady value. At basal conditions, IP3 concentrations are effectively zero, resulting in stored calcium in the ER being maintained at maximal levels. Further, even at basal incativated levels (with no shear stress) there is a finite, non-zero level of NO production and finite, non-zero levels of AKT and PKC phosphorylated eNOS, in empirical agreement with observations [135].

Our simulations indicate the that the transient behavior of eNOS activation and NO production is highly non-linear, with a bi-phasic character; a rapid initial activation due to the very rapid influx of calcium into the cytosol (occurring within 5 minutes) followed by a sustained period of activation due to protein kinases which are in turn activated by PI3K. Hence, eNOS is calcium dependent in the initial stages of the reaction cascade but becomes independent of calcium as activation continues in the sense that even after cytosolic calcium reaches steady state, eNOS activity continues to increase. The resulting Ca dependent and kinase dependent phases of eNOS activation in our model agree with the existing paradigm in the literature for the sequence of steps by which eNOS is activated [8], [16], [127]. When studying the evolution of NO production over large time periods, the enhanced activation of PI3K and subsequently AKT and PKC due to shear stress does not appear to be a major factor in eNOS activation. This is due to the apparent rapid decay of PI3K activity back to basal levels. More experimental data to clarify the behavior of PI3K following exposure to shear would be useful for fine tuning our model.

We validated our model by comparing our model predictions with a number of experimental data points reported in the literature, as well as evaluating the broad, empirical behavior of our model and verifying whether our model mimics the generally observed behavior of eNOS activation. Our predictions for the variation of NO concentrations and NO production with shear stress were compared with data, as shown in figures 6.8, 6.11 and 6.12. We suggest that the resulting agreement between model predictions and experimental data is reasonably good, especially considering the significant amount of scatter in the available experimental data reported in the published literature. Further, our predictions for the transient evolution of NO concentration following exposure to shear stress also appears to be in general agreement with reported behavior,

as shown in figure 6.9.

Additionally, as shown in figure 6.10 our predictions for both the increased levels of Akt phosphorylated eNOS and cGMP concentrations agree fairly well with reported measurements. In addition, the inhibition of protein kinases results in behavior that is in empirical agreement with previous studies. The inhibition of PI3K, which results in downregulation of both AKT and PKC results in a drastic reduction (over 70 %) in eNOS activity and NO production, behavior reported in [60], [51]. This suggests that the stimulatory effect of Akt phosphorylation is significantly more important than the inhibitory role of PKC, supporting the perspective that Akt is by far the most important protein kinase in eNOS activation. This is further demonstrated by the fact that inhibiting PKC alone results in a small but significant (18 %) increase in NO production; PKC has a smaller net effect on eNOS activation than AKT. While precise numerical data quantifying the extent of kinase inhibition vs eNOS activity at different levels of shear stress is currently unavailable in published experimental studies, our model does agree with the following empirical statement about eNOS interactions with PKC and AKT: AKT strongly upregulates eNOS activity, while PKC downregulates eNOS to a lesser extent.

To sum up, our modeled reaction cascade demonstrates the following general behavior for the activation of eNOS that is consistent with empirical conclusions reported in the experimental literature:

1) The activation of eNOS has a bi-phasic nature: first, a rapid transient process that depends on increasing levels of cytosolic calcium; second, a slower protein kinase dependent activation phase that continues even after calcium levels reach steady state [8], [16], [127]

2) Inactivation of AKT drastically reduces eNOS activity; inhibition of PKC has a smaller stimulatory effect on eNOS activation

3) Increasing shear stress increases NO concentrations and cGMP levels; over a broad range of shear stresses this behavior is highly non-linear, but for smaller variations (less than 10 $dynes/cm^2$) at physiologically relevant ranges of shear stress, a linear behavior may be used for [NO] vs shear stress [118], [122], [181].

4) The general variation of NO production vs shear stress at steady state, as

well as transient evolution of NO production appear in general agreement with reported values in the literature. Refer figures 6.8, 6.11, 6.12 and 6.9.

5) The predicted increases in NO result in significant increases in cGMP concentrations, hence we are able to account for the role of shear stress as a stimulator of vasodilation due to NO, via shear induced NO production which in turn results in significant elevations in cGMP levels, ultimately leading to vasodilation. Figure 6.10 shows that the increase in cGMP predicted in our model is consistent with experimental data [51].

6) The removal of shear stress results in a return to basal levels for all reactants, with the calcium transients occurring rapidly, while the kinase dependent transients follow more gradually. The time scales over which the system returns to basal levels of NO concentration are in general agreement with reported behavior in [118].

Due to these facts, we suggest that our model of the eNOS activation reaction cascade provides realistic predictions of shear induced NO concentrations. The fact that such a model could be constructed and used to make realistic predictions (while using existing experimental data for rate constants etc.) indicates that the existing conceptual framework for eNOS activation is at least largely correct.

Model Limitations and future work:

1) The present study does not contain a mechanical model for ECs. Instead, shear stress τ is simply an input that triggers the reaction cascade resulting in eNOS activation. The lack of a mechanical model means we are unable to account for factors such as the role of viscoelasticity in determining the transient behavior of the system. Hence, future extensions of this model will focus on the incorporation of a mechanical model of ECs that can be combined with the biochemical model presented here. Due to this lack of a viscoelastic component, we avoided examining response to oscillatory shear stress in the present model. Previous studies have shown that viscoelastic properties of the cytoskeleton have a profound effect on the mechanical behavior of the cell when exposed to oscillatory or pulsatile shear. Hence, these pulsatile and oscillatory effects will be considered in future models, along with the implementation of a mechanical model of an EC monolayer.

2) Localized effects are ignored. We assume that reactions occur in a well mixed cytosolic medium, ignoring the effects of inhomogeneities and diffusion. However, the approach used here is typical of modeling studies of EC's [142], [141], [37], [201], [200], [43]. The assumption of a well mixed medium is justifiable if we consider that diffusion time scales for proteins within the cytosol in a cell are usually fractions of a second [112], whereas the even the rapid calcium transients in our model occur at time scales of order 100 seconds. Hence, diffusion is expected to occur much more rapidly than the reactions in our model, justifying the assumption of a well mixed medium.

The assumption of a well mixed, homogeneous medium can also be problematic in the event that concentrations of reactants are exceedingly small [35], resulting in only a small number of molecules (order 100 or less withing the cell), thereby necessitating a stochastic approach. However, except at initiation of shear stress, most reactants in our model are at around order 10 nM to order 10 μM, corresponding to roughly 10^4 to 10^7 molecules per cell, a large enough number to justify the use of a deterministic, continuous system. The use of a stochastic approach during the initial moments of application of shear stress is an area that merits further investigation, however.

3) Role of other protein kinases was not considered. While AKT and PKC are generally regarded as the most important kinases that phosphorylate eNOS, other kinases such as PKA and MAPK also interact with eNOS. The precise role these kinases play in activating eNOS is still unclear, hence we restricted our study to the two most important and extensively studied protein kinases in the eNOS activation cascade. Future extensions of this model may be made to account for the role of PKA for instance (particularly upregulation of eNOS due to phosphorylation at Ser-633), as more information of the extent to which PKA impacts eNOS activity becomes available.

4) The role of protein phosphatases such as PP2A and calcineurin was not accounted for. We assumed a constant rate of dephosphorylation of eNOS with respect to both AKT and PKC; there is as yet relatively little information about how shear stress modulates phosphatase activity; changing levels of PP2A and calcineurin would be expected to alter the rates of dephosphorylation of eNOS.

5) The model reaction cascade presented in this study can be further extended to account for the role of vasoactive molecules such as bradykinin and insulin. The same

exact framework presented in this study may be used, with added differential equations incorporated to represent the activation of receptors by these signaling molecules.

Need for future experiments:

While we conclude that the broad conceptual framework of how eNOS is activated by shear stress is largely complete, various elements of this framework are still not wholly understood. Areas where more experimental data is needed include:

1) The extent to which inhibition of AKT and PKC impacts NO production and eNOS activation at different levels of shear stress

2) The role of Ca3CaM vs Ca4CaM in the recruitment of eNOS into an eNOS - CaM complex. In this study, we assumed that Ca4CaM plays the primary role in recruitment of eNOS into eNOS - CaM complexes, however more experimental data is needed to clarify this issue.

3) The extent to which PI3K and FAK are activated by mechanical stimulation, both for transient behavior and at steady state. There is at present a paucity of data on this topic, particularly with regards to the transient behavior of PI3K activation.

4) The inhibitory effect of cGMP on calcium influx. At present, we are aware of only one study [99] that records the variation of CCE rates over a broad range of cGMP concentrations. The data presented suggests that negative feedback provided by cGMP is likely not important at normal physiological conditions in ECs. The lack of such feedback greatly simplifies the task of modeling NO transport and coupling this model to upscaled transport models in order to simulate vascular mechanics [181].

5) The impact of varying cytosolic ATP concentrations on the rates of phosphorylation of eNOS by AKT and PKC. This is especially a concern since shear stress is known to increase endothelial ATP levels [80]; however, very little data is available on the relationship between shear induced ATP production and eNOS activation.

6) The role and kinetics of various protein phosphatases in the dephosphorylation of eNOS. Very little information is available at present about the extent to which shear stress impacts activity of phosphatases, especially PP2A and calcineurin.

6.7   Conclusions

We developed a model for eNOS activation by shear stress, building on previous models for the variation of calcium concentrations with shear stress in ECs [201], [142]. The resulting reaction cascade accounts for the calcium dependent and protein kinase dependent phases of eNOS activation, a significant advancement over these previous models. Our predictions for NO production vs shear stress are in broad agreement with a number of experimental data points and empirically measured behavior; this provides support to the idea that our present understanding of eNOS activation by shear stress is adequate for the purpose of modeling eNOS activation, despite the fact that certain gray areas exist where more experimental data is needed. The model cascade thus constructed may also be further extended to account for the role of signaling molecules such as insulin and Bradykinin in eNOS activation.

Table 6.1: List of acronyms used

Symbol/Acronym	Species
EC	Endothelial Cell
ECM	Extracellular Matrix
ER	Endoplasmic Reticulum
$L - Arg$	L-Arginine
$L - Cit$	L-Citruline
FAK	Focal Adhesion Kinase
$GPCR$	G-protein coupled receptor
$MSIC$	Mechano-sensing Ion Channel
G	Active G-proteins
$[G_t]$	Total concentration of G-proteins
IP_3	Inositol triphosphate
PIP_2	Phosphatidylinositol 4,5-bisphosphate
PIP_3	Phosphatidylinositol (3,4,5)-triphosphate
C_c	Cytosolic Calcium concentration
C_s	Stored Calcium concentration
C_{ex}	External Calcium concentration
CaM	Calmodulin concentration
$Ca3CaM$	Calcium-Calmodulin complex with 3 calcium ions bound to CaM
$Ca4CaM$	Calcium-Calmodulin complex with 4 calcium ions bound to CaM
$PI3K$	Phosphoinositide 3-kinase
AKT	Protein Kinase B
PKC	Protein Kinase C
$eNOS$	Endothelial Nitric Oxide Synthase
$eNOS_{cav}$	eNOS bound to caveolin
$eNOS_{cam}$	eNOS bound to calmodulin, Ca4CaM complex
$Hsp90$	Heat Shock Protein, 90 kDa
$eNOS^*$	eNOS - CaM complex phosphorylated at Ser-1197
$eNOS_0$	eNOS bound to caveolin, phosphorylated at Thr-495, blocking CaM binding
NO	Nitric Oxide
O_2	Oxygen
RBC	Red Blood Cell
sGC	Soluble Guanylate Cyclase
GTP	Guanosine Triphosphate
$cGMP$	Cyclic Guanosine Monophosphate

Chapter 7

Conclusions

The conclusions reached in this dissertation in each chapter are as follows:

7.1 Modeling autoregulatory response of an arteriole

We developed a coupled model of solid and fluid mechanics in an arteriole and demonstrated how such a model may be coupled to our previously developed model of NO transport [182]. The resulting model was able to capture the autoregulatory response of an arteriole to small variations in pressure, indicating that a simple, 3 parameter model for the solid mechanics of an arteriole is adequate for modeling vascular responses to small but physiologically significant changes in blood flow and blood pressure. The resulting model is very inexpensive computationally and should in principle be easily extend-able to modeling entire networks of vessels at very low cost.

We applied this model to the analysis of vascular response to small changes in hematocrit, by considering intralimunal pressure to vary with hematocrit, based on data presented on [116]; for this given paradoxical data we examined whether it was possible to reproduce the observed variations in flow rate (and hence cardiac output). We demonstrated that the anomalous behavior following acute changes in hematocrit reported in [116, 117, 195] is physiologically reasonable and likely occurs due to an off-setting/impeding of autoregulatory response of blood vessels. Such an offsetting of autoregulatory response to acute hematocrit variations has also previously been suggested

previously in [132].

7.2   Analysis of PEG-Albumin plasma expansion

Using a non-Newtonian model for blood flow through an arteriole, we provided an explanation for the apparently paradoxical efficacy of PEG-Albumin as a plasma expander. The administration of PEG-Alb following hemorrhagic shock was found to be as efficacious as high viscosity plasma expanders, such as Dextran 500 kDa, despite the fact that blood mixed with PEG-Alb appears to demonstrate low viscosity.

This apparent paradox was resolved by accounting for the fact that PEG-Alb demonstrates extremely strong shear thinning behavior at low shear rates. As a result, while the viscosity of PEG-Alb mixed blood appears to be drastically lower than Dextran-500 blood at large shear rates, the viscosity of PEG-Alb is greatly elevated in resistance vessels in the microcirculation. This is due to the fact that shear rates in these vessels are low enough for these shear thinning effects to become prominent. The incorporation of a non-Newtonian flow model was central to understanding this phenomenon, as this model allowed us to accurately estimate wall shear rates and shear stresses, given data on vessel centerline velocity. Hence, we demonstrated that PEG-Alb acts similar to a high viscosity plasma expander despite its low viscosity at high shear.

7.3   Development of non-Newtonian blood flow models in arterioles and derivation of Wall shear stress correction factors

We developed a flow model of blood in arterioles, based on the assumption that blood flow in arterioles consists of two distinct, homogeneous fluid layers: a Newtonian cell free layer and a non-Newtonian RBC rich core layer. The resulting flow model allowed us to make predictions for CFL thickness, tube hematocrit , velocity profiles and core hematocrit that were consistent with previously published results, yielding a flow model that provides a realistic picture of blood flow in arterioles. Our analysis yields a CFL thickness that depends on hematocrit, but is independent of vessel radius.

We then used our model to develop a correction factor for the estimation of WSS, when using the vessel radius, centerline velocity and discharge hematocrit as measured inputs. The resulting algebraic correction factor is a function of vessel radius and discharge hematocrit and may be multiplied by the estimate for WSS obtained from the Hagen-Poiseuille law to obtain a corrected, accurate estimate for WSS. In this manner, errors arising from neglecting the non-homogeneous and non-Newtonian nature of blood when estimating WSS can be readily eliminated.

7.4   Optimal branching in vascular networks

We demonstrated a method for the modeling of asymmetric vascular networks, by incorporating modifications to Murray's law, along with a model for the distribution of hematocrit at a vascular bifurcation, based on an optimization analysis. Our predictions for RBC flux fraction vs flow fraction at bifurcations suggest a linear relationship between these quantities. The modeled networks thus developed demonstrate a number of characteristics observed in vascular networks in-vivo, indicating that our model provides the first means for successfully accounting for both asymmetries at bifurcations and deviations from Murray's law when constructing model networks.

7.5   Modeling the biochemical cascade of shear induced endothelial NO production

Our model for the network of biochemical reactions that result in the production of NO following application of shear stress indicate that despite the existence of certain gray areas in our understanding of the biochemistry involved, our understanding of at least the major steps in the activation of eNOS is fairly complete.

We used a number of empirical and quantitative observations reported in the literature to validate our model; we suggest that both the transient and steady variation of NO production predicted in our model are in reasonably good agreement with published experimental data. To our knowledge, our model is the first study that successfully describes both the calcium dependent and protien kinase dependent phases of

eNOS activation, while also accounting for the existence of negative feedback.

Our analysis shows that the negative feedback provided by cGMP is relatively unimportant and can in fact be neglected. The consequence of this weak feedback is that simulations of NO transport that assume NO production is independent of NO concentration [182, 30, 102] are justified in this assumption. Further, for small but physiologically significant variations of shear stress, the relationship between NO production and shear stress may be assumed linear, as was done in [181].

7.6 Future Work

The various components of this dissertation contribute to increasing our understanding of the overall behavior of the microcirculation and greatly extend our ability to model a range of phenomena across microvascular networks. Our analysis cover a range of scales of organization across a network, highlighting the rich, multiscale properties of the network, as well as the need for developing models of processes at small scales (at the cellular level, or for an individual vessel) that can then be upscaled and applied to model entire networks.

The future direction of our work will focus on problems at each of these scales of organization, as well as the means of integrating these into a grand scheme, capable of comprehensively describing the behavior of an entire network, both for steady state and transient processes.

At the cellular scale, we will look to extend our model of NO production in Endothelial cells, to account for mechanical deformation of endothelial cells, following exposure to shear stress. Also, we will attempt to couple our model with an analysis of the reaction cascade in smooth muscle that leads to the relaxing of smooth muscle. In addition, our model can also be extended to account for signalling by insulin, bradykinin, VEGF etc in the activation of eNOS.

At the scale of individual vessels, we will couple our biochemical model introduced in chapter 7 with our model of NO transport in chapter 2 and our model of vessel mechanics in chapter 3, to arrive at a comprehensive model of vessel mechanics and autoregulation that is also capable of capturing transient behavior of these vessels.

Finally, at the scale of an entire vascular network, we will seek to explore techniques for upscaling our cellular and single vessel models, so as to capture in detail, the steady and transient behavior of vascular networks. Further, we will also look to generalize our optimized network model, to account for lower probability non-optimal configurations as well.

Appendix A

Parameters for NO Transport Modeling

A.1 Characterization of Plasma Layer Thickness as a Function of Systemic Hematocrit

The plasma layer thickness was measured in the rat cremaster muscle preparation [203] according to the technique of Kim et al. [90]. Hct was varied using either plasma or packed RBCs, from blood donors, for isovolemic hemodilution or hemoconcentration, respectively. Figure A.1 shows the data used in our simulation.

Table A.1: Model Parameters used for NO transport

Parameter	Symbol	Value	Reference
Solubility of O2	α	1.34 $mM/torr$	[102, 30]
Diffusivity of O2 in fluid layers	D_{O2}	2800 $\mu m^2/s$	[103]
Diffusivity of NO in fluid layers	D_{NO}	3300 $\mu m^2/s$	[103]
Diffusivity of O2 in solid layers	D_{O2}	1400 $\mu m^2/s$	[58, 113]
Diffusivity of NO in solid layers	D_{NO}	1650 $\mu m^2/s$	[58, 113]
Maximum O2 consumption rate in tissue	R_{O2max}	$20\mu M/s$	[30, 66]
Maximum NO production rate in endothelium	R_{NOmax}	150 $\mu M/s$	[29]
Scavenging rate constant of NO in blood	λ_b	382.5 s^{-1}	[23, 193]
Michaelis-Menten constant for endothelial NO production	K_M	4.7 $torr^{-1}$	[23]
Glycocalyx thickness	$r_g - R$	0.25 - 1 μm	[197]
Unstressed Endothelial thickness	$r_e - r_g$	1 μm	[30]
Unstressed Vascular Wall and Smooth Muscle thickness	$r_m - r_e$	80 μm	[30]
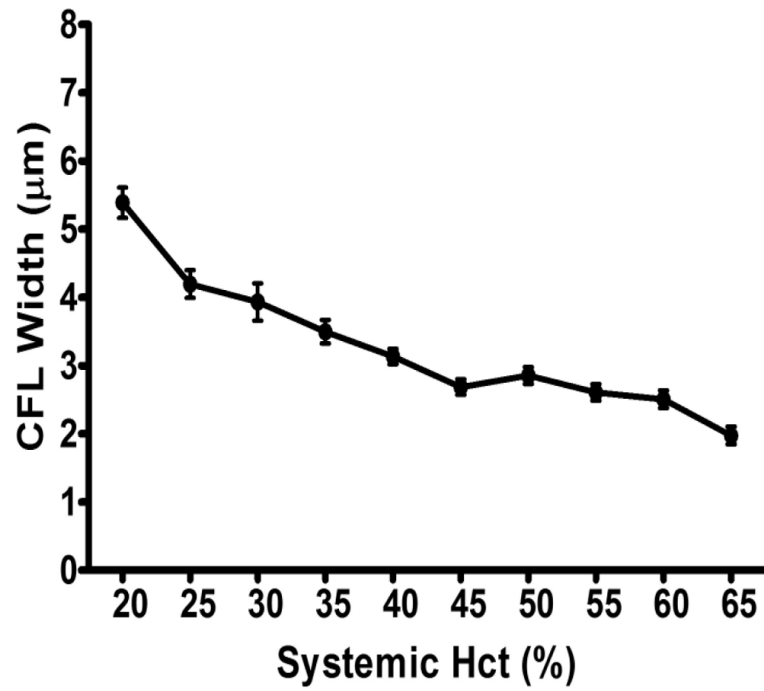
Figure A.1: Plasma layer (cell-free layer or CFL) width as a function of systemic Hct in rat cremaster muscles arterioles of 20 - 30 μm diameter.

Appendix B

Using Alternative Rheological Models for Blood in Modeling Autoregulation

Our treatment of blood as a Newtonian fluid is an approximation, as blood is typically modeled as a non-Newtonian fluid [180] that exhibits shear-thinning behavior. Modeling blood as a non-Newtonian fluid typically involves expressing blood viscosity as a function of Hct as well as shear rate. An example of the rheological models used to describing blood as a non-Newtonian fluid is the Quemada model, which was used to explore the behavior of plasma expanders [180]. Using the Quemada model instead of the Newtonian model to describe the rheology of the RBC-rich core in an arteriole, we followed the procedure outlined in [180] to calculate velocity profiles in the arteriole and to examine how flow rate varies with hematocrit. This enabled us to verify that our results are not simply the consequence of an incomplete rheological model for blood. We found that our results are relatively insensitive to the rheological model chosen and that our results (and conclusions) should hold even when blood is treated as a shear-thinning, non-Newtonian fluid. To illustrate this, Figure 11 shows the predicted variation of flow rate with systemic hematocrit, using both the Newtonian and Quemada rheological models. The difference in predicted values between the two models is small and the

same general relationship between flow rate and systemic hematocrit is preserved.
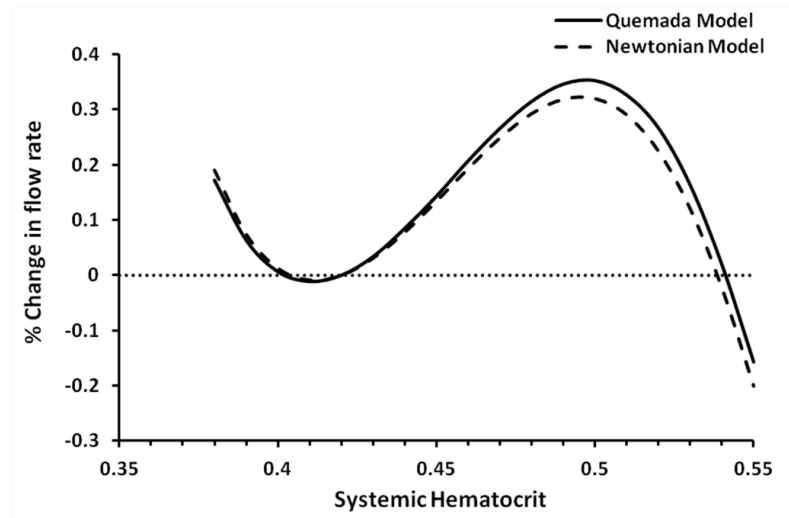
Figure B.1: Variation of flow rate with systemic hematocrit using both the Newtonian model for blood viscosity (eq. 2 in [182]) and the Quemada shear thinning model [157] for $C = 32$ in eqs. 2.12 and 2.13.

Appendix C

Two-layer Newtonian model for flow velocity

According to the two-phase Newtonian model of blood flow [172, 182] the velocity distribution in a microvessel of radius R is given by

$$v_z(\xi) = \frac{JR^2}{4\mu_p} \begin{cases} 1 - \lambda^2 + \frac{\mu_p}{\mu_c}(\lambda^2 - \xi^2) & \text{for } 0 \le \xi \le \lambda \\ 1 - \xi^2 & \text{for } \lambda < \xi \le 1 \end{cases}. \tag{C.1}$$

where μ_c is the viscosity of the RBC-rich core, $\xi = r/R$ and $\lambda = 1 - \delta/R$. When expressed in μm, the CFL width δ is given by [182]

$$\delta = -7.55H_d + 6.91. \tag{C.2}$$

For human blood, μ_c is calculated as [172]

$$\frac{\mu_c(H_c)}{\mu_p} = 1 + 2.2 \frac{(1 - H_c)^{-0.8} - 1}{(1 - 0.45)^{-0.8} - 1}. \tag{C.3}$$

Finally, the core hematocrit H_c is related to the discharge hematocrit H_d by [182, 172]

$$H_c \int_0^{R-\delta} v_z(r) r \mathrm{d}r = H_d \int_0^R v_z(r) r \mathrm{d}r. \tag{C.4}$$

The resulting set of equations is solved by following the procedure described in [182].

Appendix D

Length-Radius ratios for Vascular Networks

The premise of Murray's law is that a blood vessel's volume is determined by a compromise between minimizing the vessel's resistance to blood flow and minimizing the total volume of blood needed to serve the body's metabolic needs [173, 13, 202]. The latter condition is equivalent to positing that a blood vessel supplying a given oxygen flux $Q_{O_2} = QH$ (i.e., blood flow rate Q at a constant hematocrit H) to the surrounding tissue has an optimal volume at which this compromise between minimizing resistance to flow and minimizing vessel volume is met. This implies an "optimal" vessel volume (and since the vessel is filled with blood, an optimal volume of blood) for a given tissue volume. (The existence of an optimal blood volume has been suggested in [183, 17].) In other words, the volume of the tissue oxygenated by a vessel is related to both the vessel volume $\pi R^2 L$ and the oxygen flux QH supplied by the vessel. We assume the linear relationships, $V \propto \pi R^2 L$ and $V \propto QH$, which gives

$$\pi R^2 L \propto QH. \tag{D.1}$$

Substituting the flow rate Q predicted by the modified Murray's law in Eq. (5.7), we obtain $R^2 L \propto R^3 H / \Lambda$. This is equivalent to $L\Lambda/(HR) = \kappa$ where κ is a constant of proportionality, which leads to Eq. (5.18).

As an aside, we note that $V \propto \pi R^2 L$ implies that the ratio of the vessel volume

and the volume of the surrounding tissue it oxygenates are constant throughout a vascular network. Since the oxygen flux $Q_{O_2} = QH$ is conserved from one vessel generation to the next (due to conservation of mass), the assumption that $V \propto \pi R^2 L \propto QH$ for each generation of vessels implies that the vascular network is volume preserving (i.e. each successive generation of blood vessels has the same total volume as the preceding generation). This implies that any given tissue volume at any length scale (larger than the length of a capillary) will have a fixed volume fraction that is occupied by blood vessels. The assumption of a volume preserving network has previosuly been used in studies on scaling in biological systems [198].

Appendix E

Parameter Estimation for eNOS activation reaction cascade

GPCR activation and IP3 production: The variation of GPCR activation vs shear stress was calculated based on measurements reported in [28] for GPCR activity vs shear stress. At zero shear stress, there is no IP3 production [142], [200] (and hence no GPCR activity); GPCR activity reaches a maximal value at 24 $dynes/cm^2$ [28], at which we model GPCR activity that stimulates IP3 production to reach 100 % (i.e. maximal levels), which corresponds to a maximal level of IP3 production = 0.00546 $\mu M/s$ [142].

CCE Inhibition: The data presented in [99] suggests small, but measureable decreases in CCE with increases in intracellular cGMP concentrations, for the low (μM) concentrations of cGMP typically observed in ECs [204]. At higher cGMP concentrations, cGMP almost completely inhibits CCE, however we restrict our analysis to the range of cGMP concentrations allow for small degrees of CCE inhibition by cGMP, with the rate of inhibition increasing linearly with cGMP concentration. From the data in [99] for CCE inhibition by cGMP, we estimated $\psi([cGMP]) = 1 - 0.01[cGMP]$.

PI3K activation: On exposure to mechanical deformation/shear stress, PI3K activity reaches a maximum of around 3.5 times basal levels [63], [88], giving us $a_{pi3k} = 2.5$ in equation 6.23. We then explored a range of values for the time constant η, ranging from 0.03 s^{-1} (corresponding to a very rapid decay of PI3K activity, as seen in [63]) to 0 (no decay). We also explored a range of values of the parameter δ, which corresponds

to the shear stress at which maximal activation of PI3K occurs. As discussed in our simulation results, our model is relatively insensitive to δ; a value of $\delta = 24 dynes/cm^2$ was used, analogous to equation 6.2 for G-protein activation.

Ca4CaM binding: The rate of formation of Ca4CaM was assumed equal to the rate of calcium buffering by cytosolic proteins suggested in [76], yielding $K_{Ca4CaM} = 5s^{-1}$. The maximum concentration of Ca4CaM at saturation levels of calcium is taken as 4.5 $nM/\mu M$ of total available CaM, based on data from [140], giving a value of $\theta = 0.0045$ in equation 6.17. The cooperativity coefficient nc was taken equal to 2.7 as per [140].

eNOS-CaM binding: The rate of dissociation of eNOS-CaM was taken $= 0.01$ s^{-1}, based on values reported in [123]. The maximum rate at which eNOS binds to CaM in the presence of caveolin was estimated by assuming that at basal conditions, 90 % of eNOS is in an inactive, non-CaM bound state. This provided us with a value of $K_{cam} = 2.5\ s^{-1}$. Further, $K_{0.5cam}$ was estimated to be equal to 3 μM, based on data from [125] when Cav concentrations are significantly in excess to Ca-CaM (and hence Ca4CaM) concentrations

eNOS-kinase kinetics: The rate of phosphorylation of eNOS by PKC was estimated from data reported in [22], under the assumption of first order kinetics. This gave us values for $k_{thr} = 0.002\ s^{-1}$ and $k_{-thr} = k_{thr}/9$ for a reported equilibrium constant of 9 for the eNOS - PKC phosphorylation reaction. Similarly, the kinetics of eNOS binding with AKT (in the presence or absence of Hsp90) were evaluated based on data in [187], giving $k_{eakt} = 0.004\ s^{-1}$ and $k_{-eakt} = k_{-eakt}/18$ for an estimated equilibrium constant of 18 for the eNOS - AKT phosphorylation reaction.

NO production: Under the assumption of a constant supply of L-Arg and Oxygen, the rate of NO production depends solely on eNOS activity in the expression for R_{NO}, as given by equations 6.33 and 6.34. Hence, $K_{NOe}\frac{[O_2]}{K_{mNO}+[O_2]}$ in these equations was assumed constant. The value of this derived parameter was taken equal to $10.5s^{-1}$, which yields a basal rate of NO production $= 3.3\ \mu M/s$ per μM of eNOS, a value consistent with a range of basal NO production rates specified in [29]. The rate of NO metabolism, λ_{NO} was taken equal to 382 s^{-1}, the rate at which RBCs immediately adjacent to the ECs scavenge NO [182].

All other model parameters were taken directly from previous studies, as listed below:

Table E.1: Total reactant concentrations

Parameter	Value	Reference
$[CAM_{total}]$	30 μM	[76]
C_{ex}	1500 μM	[142]
$[G_t]$	10^5 molecules/cell	[162], [104]
$PIP2_{total}$	10 μM	[61]
$eNOS_{total}$	1 μM	[37]

Table E.2: Rate constants and Model Parameters

Parameter	Value	Reference
k_a	$2 \times 10^{-7} s^{-1}$	[162], [1]
k_i	$2 \times 10^{-1} s^{-1}$	[162], [1]
k_{deg}	$1.25 s^{-1}$	[142]
α	$0.000546 s^{-1}$	[142]
Λ	$24\ dynes/cm^2$	refer text above
k_c	$0.0 \mu M$	[142]
r_r	$0.1 s^{-1}$	[104]
k_{pip2}	$0.0493 s^{-1}$	[171]
k_{-pip2}	$0.046 s^{-1}$	[171]
V_r	3.5	[37]
k_{rel}	$6.64\ s^{-1}$	[37]
k_{res}	$5\ \mu M s^{-1}$	[37]
k_{out}	$24.7\ \mu M s^{-1}$	[37]
k_{CCE}	5.7×10^{-6}	[37]
$-k_{off}$	$5\ s^{-1}$	[76]
k_{on}	$5\ \mu M^{-1} s^{-1}$	[76]
K_{leak}	$10^{-7}\ \mu M^{-1} s^{-1}$	[142]
a_{pi3k}	2.5	refer text above
η	$0.003\ s^{-1}$	refer text above
δ	$24\ dynes/cm^2$	refer text above
k_{1p}	$1.26\ min^{-1}$	[171]
k_{2p}	$0.13\ min^{-1}$	[171]
k_{-akt}	$0.11 s^{-1}$	[171]
k_{-pkc}	$0.11 s^{-1}$	[171]
k_{thr}	$0.12\ min^{-1}$	[22]
k_{-thr}	$0.0133\ min^{-1}$	[22]
K_{Ca4CaM}	$5\ s^{-1}$	[76]
nc	2.7	refer text above
K_{dc}	$1\ \mu M$	[140]
K_{cam0}	$2.5\ s^{-1}$	refer text above
$K_{0.5cam}$	$10\ \mu M$	[125]
K_{-cam}	$0.01\ s^{-1}$	[123]
k_{eakt}	$0.004\ s^{-1}$	refer text above
k_{-eakt}	$0.004/18\ s^{-1}$	refer text above
λ_{NO}	$382\ s^{-1}$	[182]
K_{NOe}		refer text above
Φ	9	[187]
B_{NO}	15.15 nM	[38]
A_0	$1200.16\ nM^2$	[38]
A_1	$20.34\ nM$	[38]
γ_1	$4.8\ nM^2$	[38]
γ_2	$35.33\ nM$	[38]
V_{dg}	$0.0695\ s^{-1}$	[204]
K_{mdg}	$2\ \mu M$	[204]
$R_{cGMPmax} \times [SGC_0]$	$1.26\ \mu M s^{-1}$	[204]

Bibliography

[1] J.A. Adams, G.M. Omann, and J.J. Linderman. A mathematical model for ligand/receptor/g-protein dynamics and actin polymerization in human neutrophils. *J Theor Biol.*, 193(4), 1998.

[2] T. Alarcon, H. M. Byrne, and P. K. Maini. A design principle for vascular beds: the effects of complex blood rheology. *Microvasc. Res.*, 69(3):156–172, 2005.

[3] M.T. Allen and S.M. Patterson. Hemoconcentration and stress: a review of physiological mechanisms and relevance for cardiovascular disease risk. *Biol Psych.*, 41(1), 1995.

[4] C. Alonso, A. R. Pries, O. Kiesslich, D. Lerche, and P. Gaehtgens. Transient rheological behavior of blood in low-shear tube flow: velocity profiles and effective viscosity. *Am. J. Physiol.*, 268:H25–32, 1995.

[5] J. Andoi and K. Yamamoto. Vascular mechanobiology: endothelial cell responses to fluid shear stress. *Circ J.*, 73(11):1983, 2009.

[6] A.M. Andrews, D. Jaron, D.G. Buerk, and Barbee KA Kirby PL. Direct, real-time measurement of shear stress induced nitric oxide produced from endothelial cells in vitro. *Nitric Oxide*, 23(4), 2010.

[7] I. Azarov, K.T. Huang, S. Basu, M.T. Gladwin, N. Hogg, and D.B. Kim-Shapiro. Nitric oxide scavenging by red blood cells as a function of hematocrit and oxygenation. *J Biol Chem.*, 280(47), 2005.

[8] J.L. Balligand, O. Feron, and C. Dessy. enos activation by physical forces: From short-term regulation of contraction to chronic remodeling of cardiovascular tissues. *Physiol. Rev.*, 89.

[9] K.A. Barbee, P.F. Davies, and R. Lal. Shear stress-induced reorganization of the surface topography of living endothelial cells imaged by atomic force microscopy. *Circulation Research*, 74(1), 1994.

[10] J. O. Barber, J. P. Alberding, J. M. Restrepo, and T. W. Secomb. Simulated two-dimensional red blood cell motion, deformation, and partitioning in microvessel bifurcations. *Ann. Biomed. Eng.*, 36(10):1690–1698, 2008.

[11] J. O. Barber, J. M. Restrepo, and T. W. Secomb. Simulated red blood cell motion in microvessel bifurcations: Effects of cell-cell interactions on cell partitioning. *Cardiovasc. Eng. Tech.*, 2(4):349–360, 2011.

[12] O. K. Baskurt, M. R. Hardeman, M. W. Rampling, and H. J. Meiselman. *Handbook of Hemorheology and Hemodynamics*, volume 69 of *Biomedical and Health Research*. IOS Press, 2005.

[13] A. Bejan, L. A. O. Rocha, and S. Lorente. Thermodynamic optimization of geometry: T-and Y-shaped constructs of fluid streams. *Int. J. Therm. Sci.*, 39(9):949–960, 2000.

[14] D.H. Bergel. The dynamic elastic properties of the arterial wall. *J Physiol.*, 156(3), 1961.

[15] D.H. Bergel. The static elastic properties of the arterial wall. *J. Physiol.*, 156(3), 1961.

[16] B.C. Berk, M.A. Corson, T.E. Peterson, and H. Tseng. Role of integrins in endothelial mechanosensing of shear stress. *Circ Res.*, 91(9), 2002.

[17] G.F. Birchard. Optimal hematocrit: theory, regulation and implications. *Am Zool.*, 37(1), 1997.

[18] J. J. Bishop, P. R. Nance, A. S. Popel, M. Intaglietta, and P. C. Johnson. Effect of erythrocyte aggregation on velocity profiles in venules. *Am. J. Physiol. Heart Circ. Physiol.*, 280(1):H222–236, 2001.

[19] H.G. Bohlen and G.P. Nase. Dependence of intestinal arteriolar regulation on flow-mediated nitric oxide formation. *Am J Physiol.*, 279(5), 2000.

[20] Per Borgström, PER-OLOF GRÄNDE, and Stefan Mellander. A mathematical description of the myogenic response in the microcirculation. *Acta physiologica Scandinavica*, 116(4), 1982.

[21] Tom Branigan, Diogo Bolster, Beatriz Y Salazar Vázquez, Marcos Intaglietta, and Daniel M Tartakovsky. Mean arterial pressure nonlinearity in an elastic circulatory system subjected to different hematocrits. *Biomech Model Mechanobiolog.*, 10(4), 2011.

[22] D.S. Bredt, C.D. Ferris, and S.H. Snyder. Nitric oxide synthase regulatory sites. phosphorylation by cyclic amp-dependent protein kinase, protein kinase c, and calcium/calmodulin protein kinase; identification of flavin and calmodulin binding sites. *J Biol Chem.*, 267(16):10976–10981, 1992.

[23] D.G. Buerk. Can we model nitric oxide biotransport? a survey of mathematical models for a simple diatomic molecule with surprisingly complex biological activities. *Annu Rev Biomed Eng.*, 3(1), 2001.

[24] P. Cabrales and M. Intaglietta. Blood substitutes: evolution from noncarrying to oxygen- and gas-carrying fluids. *ASAIO J.*, 59(4):337–354, 2013.

[25] P. Cabrales, A. G. Tsai, and M. Intaglietta. Alginate plasma expander maintains perfusion and plasma viscosity during extreme hemodilution. *Am. J. Physiol. Heart Circ. Physiol.*, 288(4):H1708–1716, 2005.

[26] P. Cabrales, A.G. Tsai, and M. Intaglietta. Alginate plasma expander maintains perfusion and plasma viscosity during extreme hemodilution. *Am J Physiol.*, 288(4), 2005.

[27] P. Cabrales, A.G. Tsai, R.M. Winslow, and M. Intaglietta. Extreme hemodilution with peg-hemoglobin vs. peg-albumin. *Am J Physiol.*, 289(6), 2005.

[28] M. Chachisvilis, Y. Zhang, and J. A. Frangos. G protein-coupled receptors sense fluid shear stress in endothelial cells. *PNAS*, 103(42), 2006.

[29] K. Chen and A.S. Popel. Theoretical analysis of biochemical pathways of nitric oxide release from vascular endothelial cells. *Free Radic Biol Med.*, 41(4):668–680, 2006.

[30] X. Chen, D. Jaron, K.A. Barbee, and D.G. Buerk. The influence of radial rbc distribution, blood velocity profiles, and glycocalyx on coupled no/o2 transport. *J App Physiol.*, 100(2), 2006.

[31] C. P. Cheng, R. J. Herfkens, and C. A. Taylor. Abdominal aortic hemodynamic conditions in healthy subjects aged 50-70 at rest and during lower limb exercise: in vivo quantification using MRI. *Atherosclerosis*, 168(2):323–331, 2003.

[32] S. Chien, S. Usami, H. M. Taylor, J. L. Lundberg, and M. I. Gregersen. Effects of hematocrit and plasma proteins on human blood rheology at low shear rates. *J. Appl. Physiol.*, 21:81–87, 1966.

[33] W. M. Chilian, S. M. Layne, E. C. Klausner, C. L. Eastham, and M. L. Marcus. Redistribution of coronary microvascular resistance produced by dipyridamole. *Am. J. Physiol. Heart Circ. Physiol.*, 256(2):H383–H390, 1989.

[34] W.M. Chilian, S. Layne, E.C. Klausner, C.L. Eastham, and M.L.Marcus. Redistribution of coronary microvascular resistance produced by dipyridamole. *Am J Physiol.*, 256(2), 1989.

[35] T. Choi, M.R. Maurya, D.M. Tartakovsky, and S. Subramaniam. Stochastic hybrid modeling of intracellular calcium dynamics. *J Chem Phys*, 133(16), 2010.

[36] C. B. Clark, N. L. McKnight, and J. A. Frangos. Strain and strain rate activation of g proteins in human endothelial cells. *Biochem Biophys Res Commun.*, 299.

[37] A. Comerford, M.J. Plank, and T. David. Endothelial nitric oxide synthase and calcium production in arterial geometries: an integrated fluid mechanics/cell model. *J Biomech Eng.*, 130(1):011010, 2008.

[38] P. Condorelli and S. C. George. In vivo control of soluble guanylate cyclase activation by nitric oxide: A kinetic analysis. *Biophys. J.*, 80.

[39] A. Cornelissen, J. Dankelman, E. VanBavel, and J.A.E. Spaan. Balance between myogenic, flow-dependent, and metabolic flow control in coronary arterial tree: a model study. *Am J Physiol.*, 282(6), 2002.

[40] W. Cousins and P. A. Gremaud. Boundary conditions for hemodynamics: The structured tree revisited. *J. Comput. Phys.*, 231(18):6086–6096, 2012.

[41] W. Cousins, P. A. Gremaud, and D. M. Tartakovsky. A new physiological boundary condition for hemodynamics. *SIAM J. Appl. Math.*, 73(3):1203–1223, 2013.

[42] M.A. Creager, T.F. Luscher, F. Cosentino, and J.A. Beckman. Diabetes and vascular disease pathophysiology, clinical consequences, and medical therapy: Part i. *Circulation*, 108(12), 2003.

[43] T. David, S. Alzaidi, and H. Farr. Coupled autoregulation models in the cerebrovasculature. *J Eng Math.*, 64(4):403–415, 2009.

[44] P.F. Davies. Hemodynamic shear stress and the endothelium in cardiovascular pathophysiology. *Nat Clin Pract Cardiovasc Med.*, 6(1):16–26, 2008.

[45] M.J. Davis and M.A. Hill. Signaling mechanisms underlying the vascular myogenic response. *Physiol Rev.*, 79(2), 1999.

[46] D.A.Wink, K.M. Miranda, M.G. Espey, R.M. Pluta, S.J. Hewett, C. Colton, M. Vitek, M. Feelisch, and M.B. Grisham. Mechanisms of the antioxidant effects of nitric oxide. *Antioxid Redox Signal.*, 3(2):203–213, 2001.

[47] J. W. Dellimore, M. J. Dunlop, and P. B. Canham. Ratio of cells and plasma in blood flowing past branches in small plastic channels. *Am. J. Physiol. Heart Circ. Physiol.*, 244(5):H635–H643, 1983.

[48] R.B. Devereux, D.B. Case, M.H. Alderman, T.G. Pickering, S. Chien, and J.H. Laragh. Possible role of increased blood viscosity in the hemodynamics of systemic hypertension. *Am J Cardiol.*, 85(10), 2000.

[49] D.L. Diesen, D.T. Hess, and J.S. Stamler. Hypoxic vasodilation by red blood cells evidence for an s-nitrosothiol–based signal. *Circ Res.*, 103(5), 2008.

[50] S. Dimmeler, B. Assmus, C. Hermann, J. Haendeler, and A. M. Zeiher. Involvement in suppression of apoptosis: Fluid shear stress stimulates phosphorylation of akt in human endothelial cells. *Circ Res.*, 83.

[51] S. Dimmeler, I. Fleming, B. Fisslthaler, C. Hermann, R. Bussei, and A.M. Zeiher. Activation of nitric oxide synthase in endothelial cells by akt-dependent phosphorylation. *Nature*, 399(6736):601–605, 1999.

[52] P.B. Dobrin. Mechanical properties of arterises. *Physiol Rev.*, 58(2), 1978.

[53] D.M. Dudzinski, J. Igarashi, D. Greif, and T. Michel. The regulation and pharmacology of endothelial nitric oxide synthase. *Annu. Rev. Pharmacol. Toxicol.*, 46:235–276, 2006.

[54] R. Fahraeus. The suspension stability of blood. *Physiol. Rev.*, 9:562–568, 1929.

[55] J.C. Falcone, M.J. Davis, and G.A. Meininger. Endothelial independence of myogenic response in isolated skeletal muscle arterioles. *Am J Physiol.*, 260(1), 1991.

[56] D. A. Fedosov, B. Caswell, A. S. Popel, and G. E. Karniadakis. Blood flow and cell-free layer in microvessels. *Microcirc.*, 17(8):615–628, 2010.

[57] B. M. Fenton, R. T. Carr, and G. R. Cokelet. Nonuniform red cell distribution in 20 to 100 micrometers bifurcations. *Microvasc. Res.*, 29(1):103–126, 1985.

[58] S. Fischkoff and J.M. Vanderkooi. Oxygen diffusion in biological and artificial membranes determined by the fluorochrome pyrene. *The Journal Gen Physiol.*, 65(5), 1975.

[59] P. Gaehtgens, H. J. Meiselman, and H. Wayland. Velocity profiles of human blood at normal and reduced hematocrit in glass tubes up to 130 μm diameter. *Microvasc. Res.*, 2(1):13–23, 1970.

[60] B. Gallis, G.L. Corthals, D.R. Goodlett, H. Ueba, F. Kim, S.R. Presnell, D. Figeys, D.G. Harrison, B.C. Berk, and R. Aebersold. Identification of flow-dependent endothelial nitric-oxide synthase phosphorylation sites by mass spectrometry and regulation of phosphorylation and nitric oxide production by the phosphatidylinositol 3-kinase inhibitor ly294002. *J Biol Chem.*, 274(42), 1999.

[61] N. Gamper and M.S. Shapiro. Target-specific pip2 signalling: how might it work? *J Physiol.*, 582(3), 2007.

[62] K.H. Gertz, J.A. Mangos, G. Braun, and H.D. Pagel. Pressure in the glomerular capillaries of the rat kidney and its relation to arterial blood pressure. *Pflug Archiv.*, 288(4), 1966.

[63] Y. Go, H. Park, M.C. Maland, V.M. Darley-Usmar, B. Stoyanov, R. Wetzker, and H. Jo. Phosphatidylinositol 3-kinase γ mediates shear stress-dependent activation of jnk in endothelial cells. *Am J Physiol.*, 275(5):H1898–H1904, 1998.

[64] D.M. Greif, R. Kou, and T. Michel. Site specific dephosphorylation of endothelial nitric oxide synthase by protein phosphatase 2a: evidence for crosstalk between phosphorylation sites. *Biochem.*, 41(52), 2002.

[65] J. Guan. Role of focal adhesion kinase in integrin signaling. *Int J Biochem Cell Biol.*, 29(8), 1997.

[66] S.I. Gundersen, G. Chen, and A.F. Palmer. Mathematical model of no and o¡ sub¿ 2¡/sub¿ transport in an arteriole facilitated by hemoglobin based o¡ sub¿ 2¡/sub¿ carriers. *Biophys Chem.*, 143(1), 2009.

[67] S.T. Gurgel and P. do Nascimento Jr. Maintaining tissue perfusion in high-risk surgical patients: a systematic review of randomized clinical trials. *Anesth Analg.*, 112(6), 2011.

[68] H. K. Hahn, M. Georg, and H.-O. Peitgen. Fractal aspects of three-dimensional vascular constructive optimization. In *Fractals in Biology and Medicine*, pages 55–66. Birkhauser, Basel, 2005.

[69] L. Harder and L. Boshkov. The optimal hematocrit. *Crit Care Clin.*, 26(2), 2010.

[70] G. Helmlinger, B.C. Berk, and R.M. Nerem. Calcium responses of endothelial cell monolayers subjected to pulsatile and steady laminar flow differ. *Am J Physiol.*, 269(2), 1995.

[71] K. Hirata, R. Kuroda, T. Sakodai, M. Katayama, N. Inoue, M. Suematsu, S. Kawashima, and M. Yokoyama. Inhibition of endothelial nitric oxide synthase activity by protein kinase c. *Hypertension*, 25(2):180–185, 1995.

[72] R. M. Hochmuth and D. O. Davis. Changes in hematocrit for blood flow in narrow tubes. *Bibl. Anat.*, 10:59–65, 1969.

[73] S. D. House and H. H. Lipowsky. Microvascular hematocrit and red cell flux in rat cremaster muscle. *Am. J. Physiol. Heart Circ. Physiol.*, 252(1):H211–H222, 1987.

[74] A. S. Iberall. Anatomy and steady flow characteristics of the arterial system with an introduction to its pulsatile characteristics. *Math. Biosci.*, 1(3):375–395, 1967.

[75] L.J. Ignarro. Endothelium-derived nitric oxide: actions and properties. *FASEB J.*, 3(1), 1989.

[76] M.S. Jafri, S. Vajda, P. Pasik, and B. Gillo. A membrane model for cytosolic calcium oscillations a study using xenopus oocytes. *Biophys J.*, 63.

[77] R. D. Jaggi, R. Sandoz, and C. S. Effenhauser. Microfluidic depletion of red blood cells from whole blood in high-aspect-ratio microchannels. *Microfluid. Nanofluid.*, 3(1):47–53, 2007.

[78] R. J. Jendrucko and J. S. Lee. The measurement of hematocrit of blood flowing in glass capillaries by microphotometry. *Microvasc. Res.*, 6(3):316–331, 1973.

[79] H. Jo, K. Sipos, Y. Go, R. Law, J. Rong, and J.M. McDonald. Differential effect of shear stress on extracellular signal-regulated kinase and n-terminal jun kinase in endothelial cells gi2-and gβ/γ-dependent signaling pathways. *J Biol Chem.*, 272(2), 1997.

[80] K. John and A.I. Barakat. Modulation of atp/adp concentration at the endothelial surface by shear stress: effect of flow-induced atp release. *Ann Biomed Eng.*, 29(9), 2001.

[81] B.D. Johnson, K.J. Mathe, and J.P. Wallace. Mechanotransduction of shear in the endothelium: basic studies and clinical implications. *Vasc Med.*, 16(5):365–377, 2011.

[82] P.C. Johnson. Autoregulation of blood flow. *Circ Res.*, 59(5), 1986.

[83] J.W. Putney Jr., L.M. Broad, F.J. Braun, J.P. Lievremont, and G. Bird. Mechanisms of capacitative calcium entry. *J Cell Sci.*, 114(12), 2001.

[84] H. Ju, R. Zou, V.J. Venema, and R.C. Venema. Direct interaction of endothelial nitric-oxide synthase and caveolin-1 inhibits synthase activity. *J Biol Chem.*, 272(30):18522–18525, 1997.

[85] L.A. Juncos, J. Garvin, O.A. Carretero, and S. Ito. Flow modulates myogenic responses in isolated microperfused rabbit afferent arterioles via endothelium-derived nitric oxide. *J. Clin. Invest.*, 95(6), 1995.

[86] G. S. Kassab and J. A. Navia. Biomechanical considerations in the design of graft: the homeostasis hypothesis. *Annu. Rev. Biomed. Eng.*, 8:499–535, 2006.

[87] D. Katritsis, L. Kaiktsis, A. Chaniotis, J. Pantos, E. P. Efstathopoulos, and V. Marmarelis. Wall shear stress: theoretical considerations and methods of measurement. *Prog. Cardiovasc. Dis.*, 49(5):307–329, 2007.

[88] A. Katsumi, T. Naoe, T. Matsushita, K. Kaibuchi, and M. A. Schwartz. Integrin activation and matrix binding mediate cellular responses to mechanical stretch. *J Biol Chem.*, 280(17), 2005.

[89] H. Kaur, R. Carriveau, and B. Mutus. A simple parallel plate flow chamber to study effects of shear stress on endothelial cells. *Am Jl Biomed Sci.*, 4(1), 2012.

[90] S. Kim, R. L. Kong, A. S. Popel, M. Intaglietta, and P. C. Johnson. Temporal and spatial variations of cell-free layer width in arterioles. *Am. J. Physiol. Heart Circ. Physiol.*, 293:H1526–1535, 2007.

[91] N. Kleinstreuer, T. David, M.J. Plank, and Z. Endre. Dynamic myogenic autoregulation in the rat kidney: a whole-organ model. *Am J Physiol.*, 294(6), 2008.

[92] B. Klitzman and P. C. Johnson. Capillary network geometry and red cell distribution in hamster cremaster muscle. *Am. J. Physiol. Heart Circ. Physiol.*, 242(2):H211–H219, 1982.

[93] M. Kobari, F. Gotoh, Y. Fukuuchi, K. Tanaka, N. Suzuki, and D. Uematsu. Blood flow velocity in the pial arteries of cats, with particular reference to the vessel diameter. *J. Cereb. Blood Flow Metab.*, 4(1):110–114, 1984.

[94] A. G. Koutsiaris. A velocity profile equation for blood flow in small arterioles and venules of small mammals in vivo and an evaluation based on literature data. *Clin. Hemorheol. Micro.*, 43(321-334), 2009.

[95] D. N. Ku. Blood flow in arteries. *Ann. Rev. Fluid Mech.*, 29:399–434, 1997.

[96] M.J. Kuchan and J.A. Frangos. Role of calcium and calmodulin in flow-induced nitric oxide production in endothelial cells. *Am J Physiol.*, 266(3):C628–C636, 1994.

[97] M.J. Kuchan, H. Jo, and J.A. Frangos. Role of g proteins in shear stress-mediated nitric oxide production by endothelial cells. *Am J Physiol.*, 267(3), 1994.

[98] W.M. Kuebler, U. Uhlig, T. Goldmann, G. Schael, A. Kerem, K. Exner, C. Martin, E. Vollmer, and S. Uhlig. Stretch activates nitric oxide production in pulmonary vascular endothelial cells in situ. *Am J Resp Crit Care Med.*, 168(11), 2003.

[99] H. Kwan, Y. Huang, and X. Yao. Store operated calcium entry in vascular endothelial cells is inhibited by cgmp via a protein kinase g-dependent mechanism. *J Biol Chem.*, 275(10), 2000.

[100] M. LaBarbera. Principles of design of fluid transport systems in zoology. *Science*, 249(4972):992–1000, 1990.

[101] E.Y. Lai, M.L. Onozato, G. Solis, S. Aslam, W.J. Welch, and C.S. Wilcox. Myogenic responses of mouse isolated perfused renal afferent arterioles effects of salt intake and reduced renal mass. *Hypertension*, 55(4), 2010.

[102] K.A. Lamkin-Kennard, D.G. Buerk, and D. Jaron. Interactions between no and o¡ sub¿ 2¡/sub¿ in the microcirculation: a mathematical analysis. *Microvasc Res.*, 68(1), 2004.

[103] J.R. Lancaster. Simulation of the diffusion and reaction of endogenously produced nitric oxide. *PNAS*, 91(17), 1994.

[104] G. Lemon and M.R. Bennett W.G. Gibson and. Metabotropic receptor activation, desensitization and sequestration i modelling calcium and inositol 1,4,5 trisphosphate dynamics following receptor activation. *J Theor Biol.*, 223.

[105] S. Li, M. Kiml, Y. Hu, S. Jalali, D.D. Schlaepfer, T. Hunter, S. Chien, and J.Y.J. Shyy. Fluid shear stress activation of focal adhesion kinase. *J Biol Chem.*, 272(48), 1997.

[106] H. H. Lipowsky, S. Kovalcheck, and B. W. Zweifach. The distribution of blood rheological parameters in the microvasculature of cat mesentery. *Circ. Res.*, 43:738–749, 1978.

[107] H. H. Lipowsky, S. Kovalcheck, and B. W. Zweifach. The distribution of blood rheological parameters in the microvasculature of cat mesentery. *Circ. Res.*, 43(5):738–749, 1978.

[108] H. H. Lipowsky and B. W. Zweifach. Network analysis of microcirculation of cat mesentery. *Microvasc. Res.*, 7(1):73–83, 1974.

[109] D. S. Long, M. L. Smith, A. R. Pries, K. Ley, and E. R. Damiano. Microviscometry reveals reduced blood viscosity and altered shear rate and shear stress profiles in microvessels after hemodilution. *Proc. Natl. Acad. Sci. USA*, 101:10060–10065, 2004.

[110] R. Loutzenhiser, A. Bidani, and L. Chilton. Renal myogenic response kinetic attributes and physiological role. *Circ Res.*, 90(12), 2002.

[111] G.D.O. Lowe, A.J. Lee, A. Rumley, J.F. Price, and G.F.R. Fowkes. Blood viscosity and risk of cardiovascular events: the edinburgh artery study. *Brit J Haemat.*, 96(1), 1997.

[112] K. Luby-Phelps. Cytoarchitecture and physical properties of cytoplasm: volume, viscosity, diffusion, intracellular surface area. *Int Rev Cytol.*, 192, 1999.

[113] T. Malinski, Z. Taha, S. Grunfeld, S. Patton, M. Kapturczak, and P. Tomboulian. Diffusion of nitric oxide in the aorta wall monitored¡ i¿ in situ¡/i¿ by porphyrinic microsensors. *Biochem Biophys Res Comm.*, 193(3), 1993.

[114] A. Marcinkowska-Gapinska, J. Gapinski, W. Elikowski, F. Jaroszyk, and L. Kubisz. Comparison of three rheological models of shear flow behavior studied on blood samples from post-infarction patients. *Med. Bio. Eng. Comput.*, 45:837–844, 2007.

[115] B. Martinac. Mechanosensitive ion channels: molecules of mechanotransduction. *J Cell Sci.*, 117(12), 2004.

[116] J. Martini, B. Carpentier, A. Negrete, J.A. Frangos, and M. Intaglietta. Paradoxical hypotension following increased hematocrit and blood viscosity. *Am J Physiol.*, 289(5), 2005.

[117] J. Martini, A.G. Tsai, P.C. Cabrales, P.C. Johnson, and M. Intaglietta. Increased cardiac output and microvascular blood flow during mild hemoconcentration in hamster window model. *Am J Physiol.*, 291(1), 2006.

[118] G. A. Mashour and R. J. Boock. Effects of shear stress on nitric oxide levels of human cerebral endothelial cells cultured in an artificial capillary system. *Brain Res.*, 842(1):233–238, 1999.

[119] B. R. Masters. Fractal analysis of the vascular tree in the human retina. *Annu. Rev. Biomed. Eng.*, 6:427–452, 2004.

[120] M. Matsubara, N. Hayashi, T. Jing, and K. Titani. Regulation of endothelial nitric oxide synthase by protein kinase c. *J Biochem.*, 133(6):773–781, 2003.

[121] H. N. Mayrovitz and J. Roy. Microvascular blood flow: evidence indicating a cubic dependence on arteriolar diameter. *Am. J. Physiol. Heart Circ. Physiol.*, 245(6):H1031–H1038, 1983.

[122] T.N. McAllister and J.A. Frangos. Steady and transient fluid shear stress stimulate no release in osteoblasts through distinct biochemical pathways. *J Bone Miner Res.*, 14(6), 1999.

[123] J.L. McMurry, C.A. Chrestensen, I.M. Scott, E.W. Lee, A.M. Rahn, A.M. Johansen, B.J. Forsberg, K.D. Harris, and J.C. Salerno. Rate, affinity and calcium dependence of nitric oxide synthase isoform binding to the primary physiological regulator calmodulin. *FEBS Journal*, 278(24):4943–4954, 2011.

[124] A.M. Melkumyants, S.A. Balashov, and V.M. Khayutin. Endothelium dependent control of arterial diameter by blood viscosity. *Cardiovasc Res.*, 23(9), 1989.

[125] J.B. Michel, O. Feron, K. Sase, P. Prabhakar, and T. Michel. Caveolin versus calmodulin. counterbalancing allosteric modulators of endothelial nitric oxide synthase. *J Biol Chem.*, 272(41), 1997.

[126] F. Morello, A. Perino, and E. Hirsch. Phosphoinositide 3-kinase signalling in the vascular system. *Cardiovasc Res.*, 82(2):261–271, 2009.

[127] P.F. Mount, B.E. Kemp, and D.A. Power. Regulation of endothelial and myocardial no synthesis by multi-site enos phosphorylation. *J Mol Cell Cardiol.*, 42(2), 2007.

[128] C. D. Murray. The physiological principle of minimum work applied to the angle of branching of arteries. *J. Gen. Physiol.*, 9(6):835–841, 1926.

[129] C. D. Murray. The physiological principle of minimum work: I. The vascular system and the cost of blood volume. *Proc. Natl. Acad. Sci. USA*, 12(3):207–214, 1926.

[130] P. K. Nair, J. D. Hellums, and J. S. Olson. Prediction of oxygen transport rates in blood flowing in large capillaries. *Microvasc. Res.*, 38:269–285, 1989.

[131] T.R. Nurkiewicz and Matthew A M.A. Boegehold. Limitation of arteriolar myogenic activity by local nitric oxide: segment-specific effect of dietary salt. *Am J Physiol.*, 277(5), 1999.

[132] Y. Ogawa, K. Iwasaki, K. Aoki, S. Shibata, J. Kato, and S. Ogawa. Central hypervolemia with hemodilution impairs dynamic cerebral autoregulation. *Anesth Analg.*, 105(5), 2007.

[133] J. D. Oliver. The viscosity of human blood at high hematocrits. Master's thesis, MIT, 1986.

[134] M. S. Olufsen. Structured tree outflow condition for blood flow in larger systemic arteries. *Am. J. Physiol. Heart Circ. Physiol.*, 276(1):H257–H268, 1999.

[135] M. Ozeki, H. Watanabe, J. Luo, T. Nakano, K. Takeuchi, Y. Kureishi, M. Ito, T. Nakano, K. Ohashi, and H. Hayashi. Akt and ca2+ signaling in endothelial cells. *Mol Cell Biochem.*, 259(1-2):169–176, 2004.

[136] H.Y. Park, S.A. Kim, J. Korlach, E. Rhoades, L.W. Kwok, W.R. Zipfel, M.N. Waxham, W.W. Webb, and L. Pollack. Conformational changes of calmodulin upon ca2+ binding studied with a microfluidic mixer. *PNAS*, 105(2):542–547, 2008.

[137] K.W. Park, H.B. Dai, E. Lowenstein, and F.W.Sellke. Steady-state myogenic response of rat coronary microvessels is preserved by isoflurane but not by halothane. *Anesth Analg.*, 82(5), 1996.

[138] S.W. Park, M. Intaglietta, and D.M. Tartakovsky. Impact of endothelium roughness on blood flow. *J theor biol.*, 300, 2012.

[139] D.J. Patel, D.L. Fry, and J.S. Janicki. Longitudinal tethering of arteries in dogs. *Circ Res.*, 19(6), 1966.

[140] A. Persechini and B. Cronk. The relationship between the free concentrations of ca2+ and ca2+-calmodulin in intact cells. *J Bioll Chem.*, 274(11), 1999.

[141] M.J. Plank, D.J.N. Wall, and T. David. The role of endothelial calcium and nitric oxide in the localisation of atherosclerosis. *Math Biosci.*, 207.

[142] M.J. Plank, D.J.N. Wall, and T. David. Atherosclerosis and calcium signalling in endothelial cells. *Prog Biophys Mol Biol.*, 91(3):287–313, 2006.

[143] W.C. Plunkett and H.W. Overbeck. Increased arteriolar wall-to-lumen ratio in a normotensive vascular bed in coarctation hypertension. *Am J Physiol.*, 249(4), 1985.

[144] A.S. Pope and G. Enden. An analytical solution for steady flow of a quemada fluid in a circular tube. *Rheol Acta*, 32(4), 1993.

[145] A. S. Popel and P. C. Johnson. Microcirculation and hemorheology. *Ann. Rev. Fluid Mech.*, 37:43–69, 2005.

[146] T. Porumb. Determination of calcium-binding constants by flow dialysis. *Anal Biochem.*, 220(2):227–237, 1994.

[147] B. Prakash and M. Singh. Optimum kinetic energy dissipation to maintain blood flow in glass capillaries: an analysis based on flow field determination by axial tomographic and image velocimetry techniques. *J Biomech*, 28(6), 1995.

[148] A. R. Pries, A. Fritzsche, K. Ley, and P. Gaehtgens. Redistribution of red blood cell flow in microcirculatory networks by hemodilution. *Circ. Res.*, 70(6):1113–1121, 1992.

[149] A. R. Pries, G. Kanzow, and P. Gaehtgens. Microphotometric determination of hematocrit in small vessels. *Am. J. Physiol. Heart Circ. Physiol.*, 245(1):H167–177, 1983.

[150] A. R. Pries, K. Ley, M. Claassen, and P. Gaehtgens. Red cell distribution at microvascular bifurcations. *Microvasc. Res.*, 38(1):81–101, 1989.

[151] A. R. Pries, D. Neuhaus, and P. Gaehtgens. Blood viscosity in tube flow: dependence on diameter and hematocrit. *Am. J. Physiol. Heart Circ. Physiol.*, 263:H1770–1778, 1992.

[152] A. R. Pries, D. Neuhaus, and P. Gaehtgens. Blood viscosity in tube flow: dependence on diameter and hematocrit. *Am. J. Physiol. Heart Circ. Physiol.*, 263:H1770–1778, 1992.

[153] A. R. Pries, T. W. Secomb, and P. Gaehtgens. Design principles of vascular beds. *Circ. Res.*, 77(5):1017–1023, 1995.

[154] A. R. Pries, T. W. Secomb, P. Gaehtgens, and J. F. Gross. Blood flow in microvascular networks. Experiments and simulation. *Circ. Res.*, 67(4):826–834, 1990.

[155] A. R. Pries, T. W. Secomb, T. Gessner, M. B. Sperandio, J. F. Gross, and P. Gaehtgens. Resistance to blood flow in microvessels in vivo. *Circ. Res.*, 75(5):904–915, 1994.

[156] A.R. Pries, T.W. Secomb, and P. Gaehtgens. Structural autoregulation of terminal vascular beds vascular adaptation and development of hypertension. *Hypertension*, 33(1), 1999.

[157] D. Quemada. Rheology of concentrated dispersed systems: III. General features of the proposed non-Newtonian model: Comparison with experimental data. *Rheol. Acta*, 17:643–653, 1978.

[158] R. Rafikov, F.V. Fonseca, S. Kumar, D. Pardol, C. Darragh, S. Elms, D. Fulton, and S.M. Black. enos activation and no function: structural motifs responsible for the posttranslational control of endothelial nitric oxide synthase activity. *J Endocrin.*, 210(3):271–284, 2011.

[159] W. Reinke, P. Gaehtgens, and P. C. Johnson. Blood viscosity in small tubes: effect of shear rate, aggregation, and sedimentation. *Am. J. Physiol. Heart Circ. Physiol.*, 253:H540–547, 1987.

[160] R. S. Reneman, T. Arts, and A. P. Hoeks. Wall shear stress–an important determinant of endothelial cell function and structure–in the arterial system in vivo. Discrepancies with theory. *J. Vasc. Res.*, 43:251–269, 2006.

[161] R. Revellin, F. Rousset, D. Baud, and J. Bonjour. Extension of Murray's law using a non-Newtonian model of blood flow. *Theor. Biol. Medical Modell.*, 6:7, 2009.

[162] T.A. Riccobene, G.M. Omann, and J.J. Linderman. Modeling activation and desensitization of g-protein coupled receptors provides insight into ligand efficacy. *J Theor Biol.*, 200(2), 1999.

[163] T.Q. Richardson and A.C. Guyton. Effects of polycythemia and anemia on cardiac output and other circulatory factors. *Am J Physiol.*, 197(6), 1959.

[164] V. Richter, M. D. Savery, M. Gassmann, O. Baum, E. R. Damiano, and A. R. Pries. Excessive erythrocytosis compromises the blood-endothelium interface in erythropoietin-overexpressing mice. *J. Physiol.*, 589:5181–5192, 2011.

[165] C. E. Riva, J. E. Grunwald, and S. H. Sinclair. Laser doppler velocimetry study of the effect of pure oxygen breathing on retinal blood flow. *Invest. Ophthalmol. Vis. Sci.*, 24(1):47–51, 1983.

[166] S. Rossitti and J. Lofgren. Vascular dimensions of the cerebral arteries follow the principle of minimum work. *Stroke*, 24(3):371–377, 1993.

[167] P.A. Sarma, R.M. Pidaparti, and R.A. Meiss. Anisotropic properties of tracheal smooth muscle tissue. *J Biomed Mat Res A.*, 65(1), 2003.

[168] G. W. Schmid-Schonbein. Biomechanics of microcirculatory blood perfusion. *Annu. Rev. Biomed. Eng.*, 1(1):73–102, 1999.

[169] R. Schubert and M.J. Mulvany. The myogenic response: established facts and attractive hypotheses. *Clin Sci.*, 96, 1999.

[170] T.W. Secomb. Theoretical models for regulation of blood flow. *Microcirc.*, 15(8), 2008.

[171] A.R. Sedaghat, A. Sherman, and M.J. Quon. A mathematical model of metabolic insulin signaling pathways. *Am J Physiol Endocrinol Metab.*, 283.

[172] M. Sharan and A. S. Popel. A two-phase model for flow of blood in narrow tubes with increased effective viscosity near the wall. *Biorheology*, 38:415–428, 2001.

[173] T. F. Sherman. On connecting large vessels to small. The meaning of Murray's law. *J. Gen. Physiol.*, 78(4):431–453, 1981.

[174] J. M. Sherwood, E. Kaliviotis, J. Dusting, and S. Balabani. Hematocrit, viscosity and velocity distributions of aggregating and non-aggregating blood in a bifurcating microchannel. *Biomech. Model. Mechanobiol.*, 11:1–15, 2012.

[175] J.K. Shoemaker. Hemodilution impairs cerebral autoregulation, demonstrating the complexity of integrative physiology. *Anesth Analg.*, 105(5), 2007.

[176] J.Y.J. Shyy and S. Chien. Role of integrins in endothelial mechanosensing of shear stress. *Circ Res.*, 91(9), 2002.

[177] V. Smiesko and P.C. Johnson. The arterial lumen is controlled by flow-related shear stress. *Physiology*, 8(1), 1993.

[178] K. Sriram, B. Y. Salazar Vázquez, A. G. Tsai, P. Cabrales, M. Intaglietta, and D. M. Tartakovsky. Autoregulation and mechanotransduction control the arteriolar response to small changes in hematocrit. *Am. J. Physiol. Heart Circ. Physiol.*, 303(9):H1096–1106, 2012.

[179] K. Sriram, B. Y. Salazar Vázquez, O. Yalcin, P. C. Johnson, M. Intaglietta, and D. M. Tartakovsky. The effect of small changes in hematocrit on nitric oxide transport in arterioles. *Antioxid. Redox Signal.*, 14(2):175–185, 2011.

[180] K. Sriram, A. G. Tsai, P. Cabrales, F. Meng, S. A. Acharya, D. M. Tartakovsky, and M. Intaglietta. PEG-albumin supra plasma expansion is due to increased vessel wall shear stress induced by blood viscosity shear thinning. *Am. J. Physiol. Heart Circ. Physiol.*, 302(12):H2489–2497, 2012.

[181] K. Sriram, B.Y. Salazar Vazquez, A.G. Tsa, P. Cabrales, M. Intaglietta, and D.M. Tartakovsky. Autoregulation and mechanotransduction control the arteriolar response to small changes in hematocrit. *Am J Physiol Heart Circ Physiol.*, 303(9), 2012.

[182] K. Sriram, B.Y. Salazar Vazquez, O. Yalcin, P.C. Johnson, M. Intaglietta, and D.M. Tartakovsky. The effect of small changes in hematocrit on nitric oxide transport in arterioles. *Antioxid Redox Signal.*, 14(2):175–185, 2011.

[183] H. Stark and S. Schuster. Comparison of various approaches to calculating the optimal hematocrit in vertebrates. *J. Appl. Physiol.*, 113(3):355–367, 2012.

[184] D. W. Stepp, Y. Nishikawa, and W. M. Chilian. Regulation of shear stress in the canine coronary microcirculation. *Circulation*, 100(14):1555–1561, 1999.

[185] U. Storch, M. Mederos y Schnitzler, and T. Gudermann. G protein-mediated stretch reception. *Am J Physiol Heart Circ Physiol.*, 302.

[186] Y. Suzuki, N. Tateishi, M. Soutani, and N. Maeda. Flow behavior of erythrocytes in microvessels and glass capillaries: effects of erythrocyte deformation and erythrocyte aggregation. *Int. J. Microcirc. Clin. Exp.*, 16(4):187–194, 1996.

[187] S. Takahashi and M.E. Mendelsohn. Synergistic activation of endothelial nitric-oxide synthase (enos) by hsp90 and akt calcium-independent enos activation involves formation of an hsp90-akt-cam-bound enos complex. *J Biol Chem.*, 278(33):30821–30827, 2003.

[188] G. J. Tangelder, D. W. Slaaf, and R. S. Reneman. Velocity profiles of blood platelets and red blood cells flowing in arterioles of the rabbit mesentery. *Circ. Res.*, 59:505–514, 1986.

[189] L.A. Taylor and J.H. Gerrard. Pressure-radius relationships for elastic tubes and their application to arteries: Part 1-theoretical relationships. *Med Biol Engg Comp.*, 15(1), 1977.

[190] A.G. Tsai, C. Acero, P.R. Nance, P. Cabrales, J.A. Frangos, D.G. Buerk, and M. Intaglietta. Elevated plasma viscosity in extreme hemodilution increases perivascular nitric oxide concentration and microvascular perfusion. *Am J Physiol.*, 288(4), 2005.

[191] A.G. Tsai, P. Cabrales, B.N. Manjula, S.A. Acharya, R.M. Winslow, and M. Intaglietta. Dissociation of local nitric oxide concentration and vasoconstriction in the presence of cell-free hemoglobin oxygen carriers. *Blood*, 108(10), 2006.

[192] A.G. Tsai, B. Friesenecker, M. McCarthy, H. Sakai, and M. Intaglietta. Plasma viscosity regulates capillary perfusion during extreme hemodilution in hamster skinfold model. *Am J Physiol.*, 275(6), 1998.

[193] N.M. Tsoukias and A.S. Popel. Erythrocyte consumption of nitric oxide in presence and absence of plasma-based hemoglobin. *Am J Physiol.*, 51(6), 2002.

[194] M. Vaughn, M.W. Mark, K.T. Huang, L. Kuo, and J.C. Liao. Erythrocyte consumption of nitric oxide: competition experiment and model analysis. *Nitric Oxide*, 5(1), 2001.

[195] B.Y. Salazar Vazquez, J. Martini, A. Chavez Negrete, P. Cabrales, A.G. Tsai, and M. Intaglietta. Microvascular benefits of increasing plasma viscosity and maintaining blood viscosity: counterintuitive experimental findings. *Biorheol.*, 46(3), 2009.

[196] X.U. Weiming, L.Z. Liu, M. Loizidou, M. Ahmed, and I.G. Charles. The role of nitric oxide in cancer. *Cell Res.*, 12(5), 2002.

[197] S. Weinbaum, J.M. Tarbell, and E.R. Damiano. The structure and function of the endothelial glycocalyx layer. *Annu. Rev. Biomed. Eng.*, 9, 2007.

[198] G. B. West, J. H. Brown, and B. J. Enquist. A general model for the origin of allometric scaling laws in biology. *Science*, 276(5309):122–126, 1997.

[199] D.K. Whirlow and W.T. Rouleau. Periodic flow of a viscous liquid in a thick-walled elastic tube. *Bull Math Biophys.*, 27(3), 1965.

[200] T. F. Wiesner, B. C. Berk, and R. M. Nerem. A mathematical model of cytosolic calcium dynamics in human umbilical vein endothelial cells. *Am. J. Physiol. (Cell Physiol.)*, 270(39), 1996.

[201] T.F. Wiesner, B.C. Berk, and R.M. Nerem. A mathematical model of the cytosolic-free calcium response in endothelial cells to fluid shear stress. *PNAS*, 94(8), 1997.

[202] H. R. Williams, R. S. Trask, P. M. Weaver, and I. P. Bond. Minimum mass vascular networks in multifunctional materials. *J. R. Soc. Interface*, 5(18):55–65, 2008.

[203] O. Yalcin, C. Choi, S. Chatpun, M. Intaglietta, and P.C. Johnson. The dependence of cell-free layer thickness in arterioles on systemic hematocrit level. *FASEB J.*, 23, 2009.

[204] J. Yang, J.W. Clark, R.M. Bryan, and C.S. Robertson. Mathematical modeling of the nitric oxide/cgmp pathway in the vascular smooth muscle cell. *Am J Physiol Heart Circ Physiol.*, 289(2), 2005.

[205] X. Yao, H.Y. Kwan, F.L. Chan, N.W.K. Chan, and Y. Huang. A protein kinase g-sensitive channel mediates flow-induced ca2+ entry into vascular endothelial cells. *FASEB J.*, 14(7), 2000.